Universiteit Gent
Faculteit Ingenieurswetenschappen en Architectuur
Vakgroep Informatietechnologie
Vakgroep Elektronica en Informatiesystemen

Wavelength Tunability of Silicon-On-Insulator Ring Resonators with a Cladding Layer of Liquid Crystals

Golflengteafstembaarheid van ringresonators in silicium-op-isolator met een toplaag van vloeibare kristallen

---

Wout De Cort

Proefschrift tot het bekomen van de graad van
Doctor in de Ingenieurswetenschappen:
Fotonica
Academiejaar 2011-2012

Promotoren:

Prof. Dr. Ir. Kristiaan Neyts
Prof. Dr. Ir. Roel Baets

Examencommissie:

Prof. Dr. Ir. Hendrik Van Landeghem *(voorzitter)*, UGent, Industrieel Beheer
Prof. Dr. Ir. Kristiaan Neyts *(promotor)*, UGent, ELIS
Prof. Dr. Ir. Roel Baets *(promotor)*, UGent, INTEC
Prof. Dr. Ir. Jeroen Beeckman, UGent, ELIS
Prof. Dr. Ir. Wim Bogaerts *(secretaris)*, UGent, INTEC
Prof. Dr. Tomasz Wolinski, Warsaw Univ. of Technology
Prof. Dr. Ir. Zeger Hens, UGent, Anorganische en Fysische Chemie

Universiteit Gent
Faculteit Ingenieurswetenschappen en Architectuur

Vakgroep Informatietechnologie
Vakgroep Elektronica en Informatiesystemen
Sint-Pietersnieuwstraat 41, B-9000 Gent, België

Dit werk kwam tot stand in het kader van een specialisatiebeurs van het agentschap voor Innovatie door Wetenschap en Technologie.

Dankwoord

Gent, februari 2012
Wout De Cort

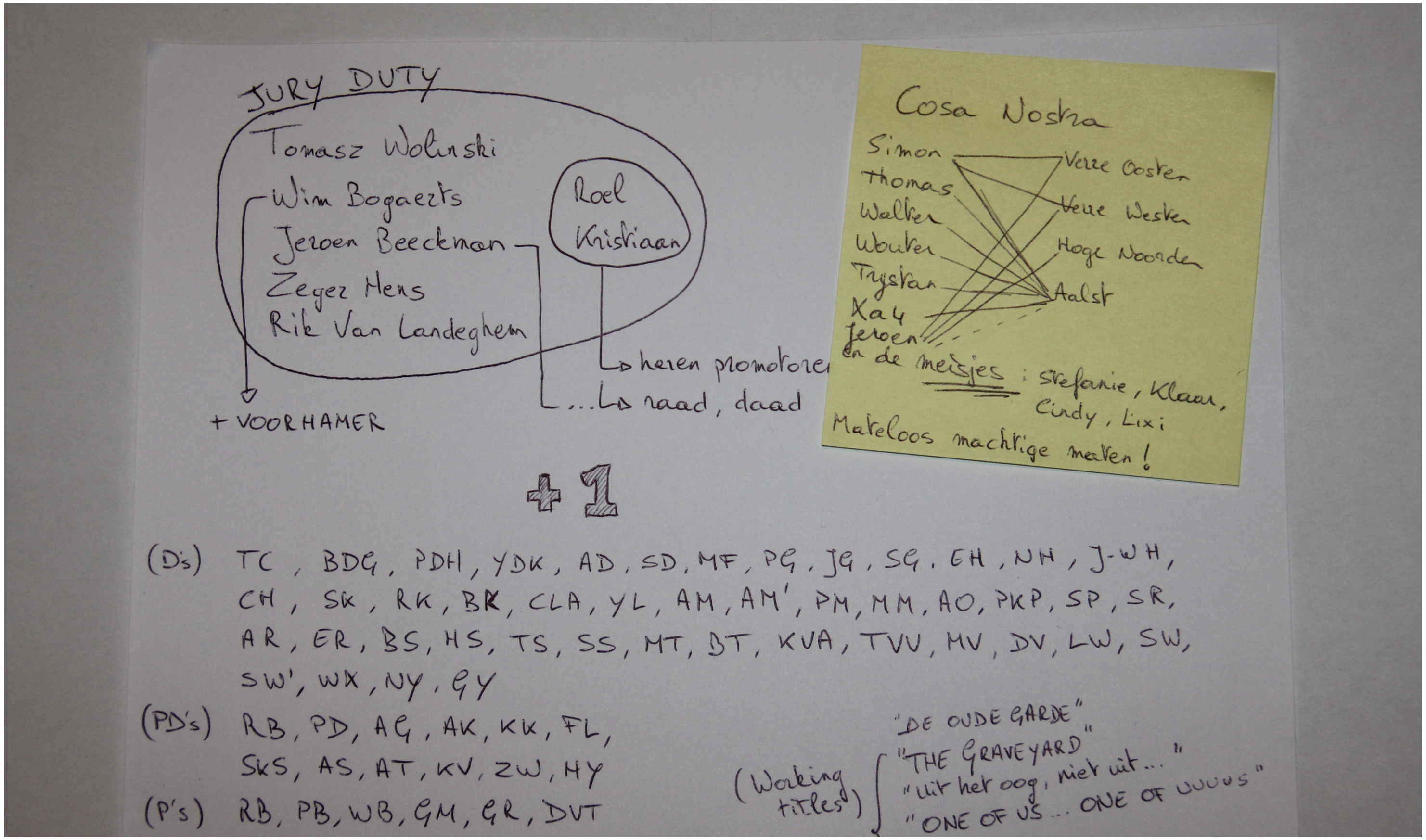

JURY DUTY

Tomasz Wolinski
Wim Bogaerts
Jeroen Beeckman
Zeger Hens
Rik Van Landeghem

Roel
Kristiaan

↳ heren promotoren
...↳ raad, daad

+ VOORHAMER

Cosa Nostra

Simon
Thomas
Walter
Wouter
Trystan
Xa4
Jeroen

Verre Oosten
Verre Westen
Hoge Noorden
Aalst

en de meisjes: Stefanie, Klaar, Cindy, Lixi:
Mateloos machtige maten!

+1

(D's) TC, BDG, PDH, YDK, AD, SD, MF, PG, JG, SG, EH, NH, J-WH, CH, SK, RK, BK, CLA, YL, AM, AM', PM, MM, AO, PKP, SP, SR, AR, ER, BS, HS, TS, SS, MT, DT, KVA, TVV, MV, DV, LW, SW, SW', WX, NY, GY

(PD's) RB, PD, AG, AK, KK, FL, SKS, AS, AT, KV, ZW, HY

(P's) RB, PB, WB, GM, GR, DVT

(Working titles)
"DE OUDE GARDE"
"THE GRAVEYARD"
"Uit het oog, niet uit..."
"ONE OF US... ONE OF UUUUS"

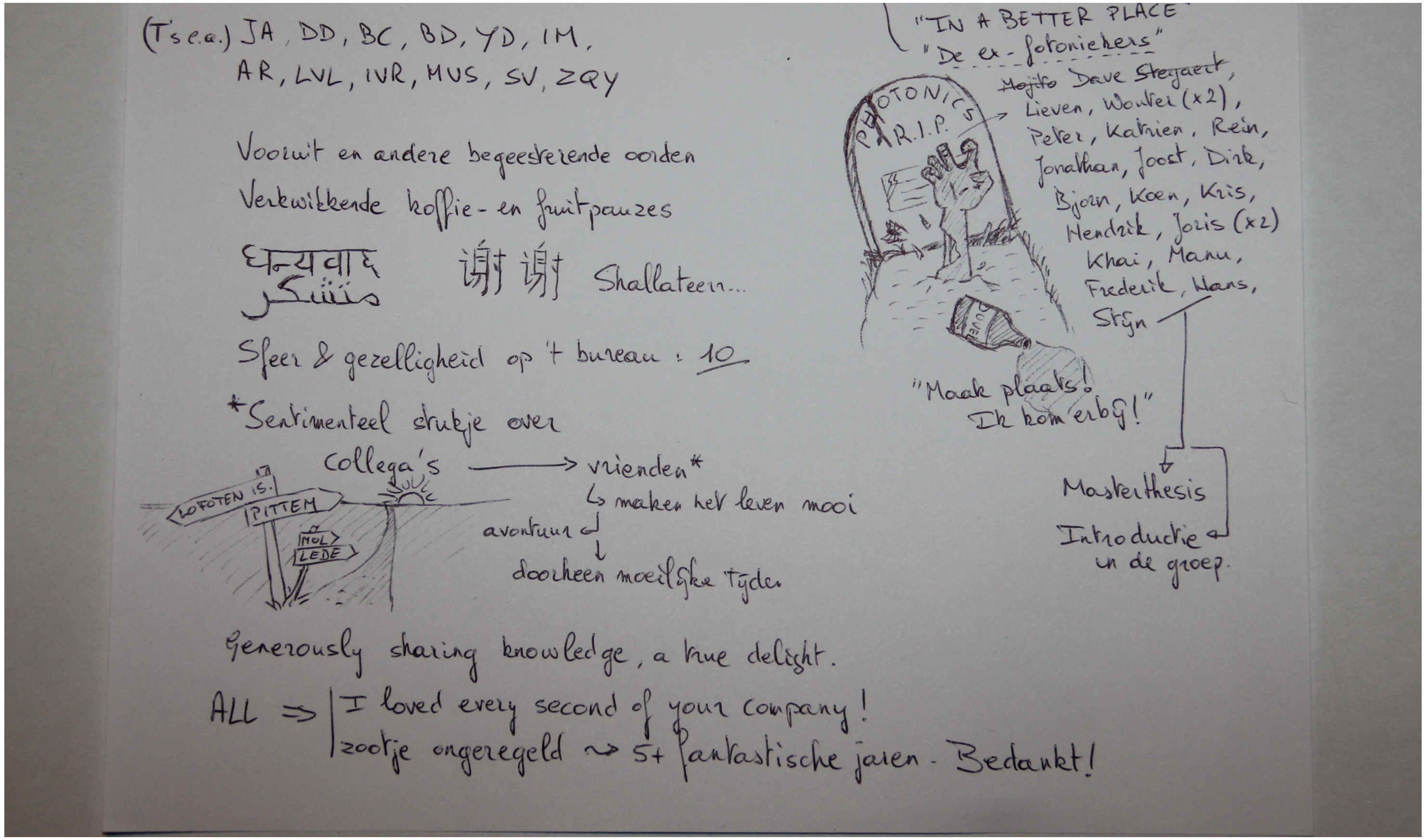

(T's e.a.) JA, DD, BC, BD, YD, IM,
AR, LVL, IVR, MUS, SV, ZQY

Voorwit en andere begeesterende woorden

Verkwikkende koffie- en fruitpauzes

धन्यवाद
متشكر
谢 谢 Shallateen...

Sfeer & gezelligheid op 't bureau : 10

*Sentimenteel stukje over
collega's ⟶ vrienden*
↳ maken het leven mooi
avontuur ↵
↓
doorheen moeilijke tijden

"IN A BETTER PLACE"
"De ex-fotoniekers"
~~Mojito~~ Dave ~~Steyaert~~,
Lieven, Wouter (x2),
Peter, Katrien, Rein,
Jonathan, Joost, Dirk,
Bjorn, Koen, Kris,
Hendrik, Joris (x2)
Khai, Manu,
Frederik, Hans,
Stijn

"Maak plaats!
Ik kom erbij!"

Masterthesis
Introductie
in de groep.

Generously sharing knowledge, a true delight.

ALL ⇒ | I loved every second of your company!
| zootje ongeregeld ⇝ 5+ fantastische jaren. Bedankt!

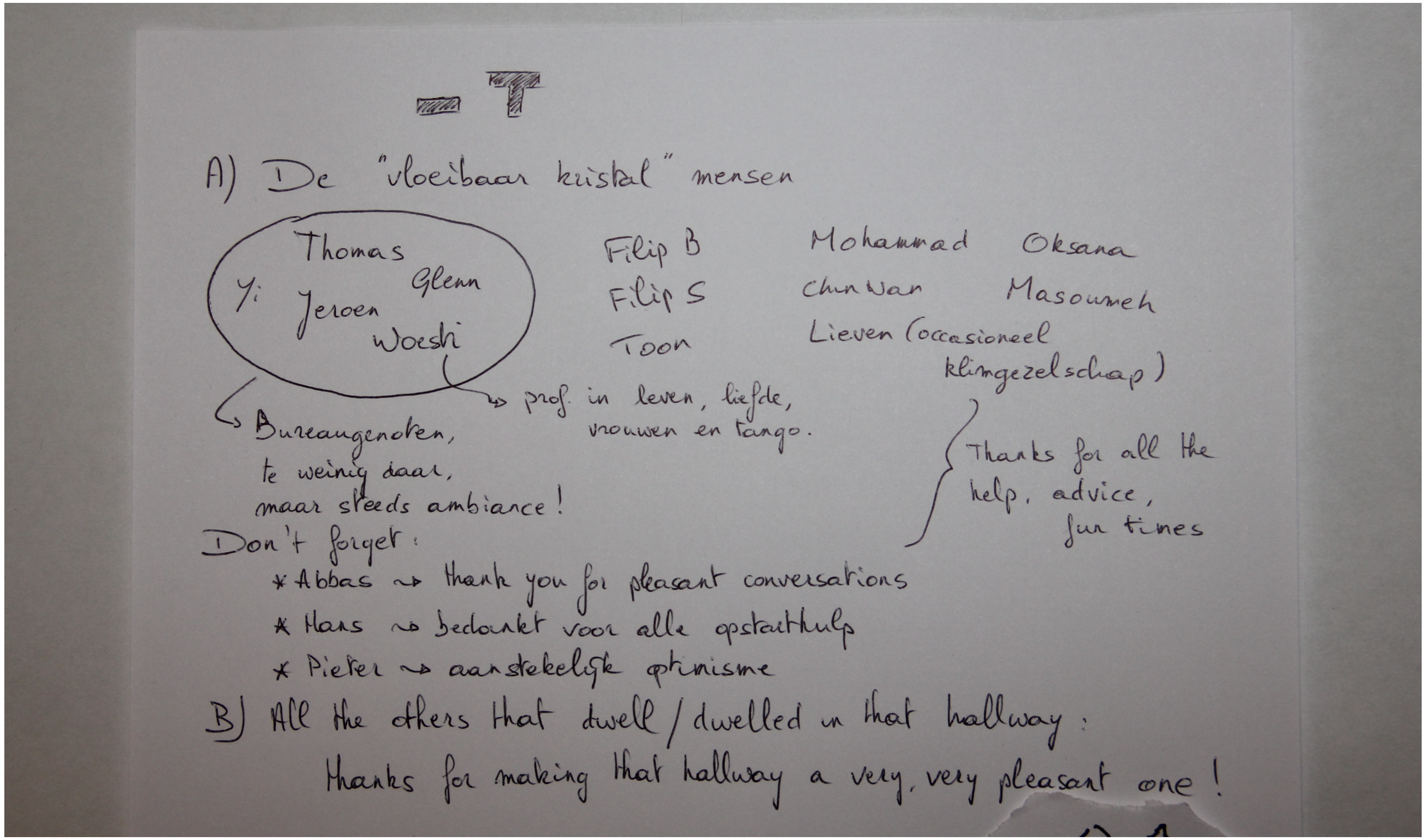

A) De "vloeibaar kristal" mensen

Y: Thomas Glenn Jeroen Woeshi

→ prof. in leven, liefde, vrouwen en tango.

→ Bureaugenoten, te weinig daar, maar steeds ambiance!

Filip B
Filip S
Toon

Mohammad
ChunWan
Lieven (occasioneel klimgezelschap)

Oksana
Masoumeh

Thanks for all the help, advice, fun times

Don't forget:

- * Abbas → thank you for pleasant conversations
- * Hans → bedankt voor alle opstarthulp
- * Pieter → aanstekelijk optimisme

B) All the others that dwell / dwelled in that hallway:

Thanks for making that hallway a very, very pleasant one!

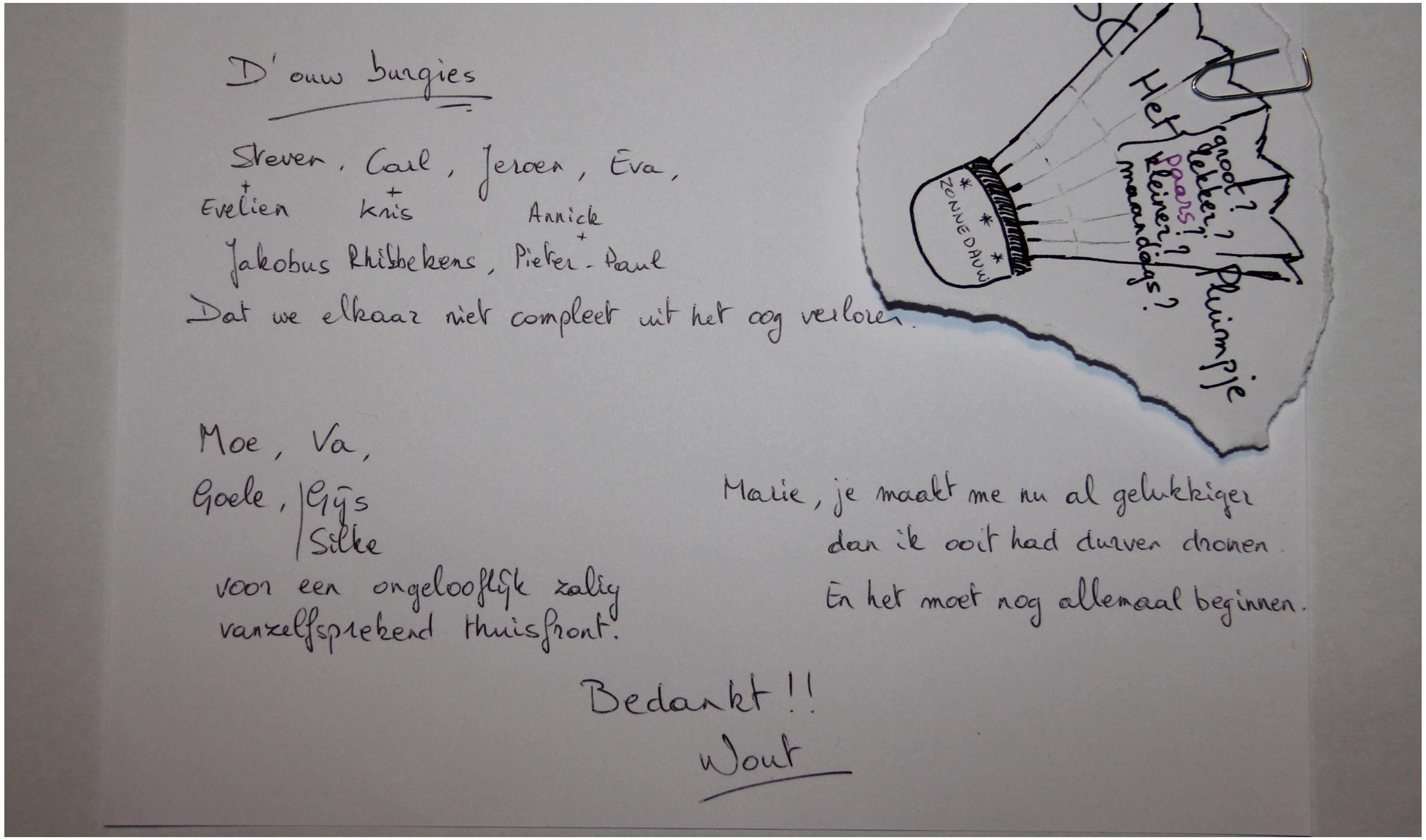

D'ouw burgies

Steven, Carl, Jeroen, Eva,
+ Evelien + Kris Annick +
Jakobus Rhibbekens, Pieter-Paul
Dat we elkaar niet compleet uit het oog verloren.

Moe, Va,
Goele, | Gijs
| Silke
voor een ongelooflijk zalig
vanzelfsprekend thuisfront.

Marie, je maakt me nu al gelukkiger
dan ik ooit had durven dromen.
En het moet nog allemaal beginnen.

Bedankt!!
Wout

Table of Contents

Dankwoord i

Nederlandse samenvatting xvii

English summary xxiii

1 Introduction 1

- 1.1 Liquid crystals 3
  - 1.1.1 Liquid or crystal? 3
  - 1.1.2 Liquid crystal types 3
    - 1.1.2.1 Thermotropic liquid crystals 4
  - 1.1.3 Nematic liquid crystals in detail 5
    - 1.1.3.1 Order parameter 7
    - 1.1.3.2 Dielectric and optical anisotropy 7
    - 1.1.3.3 Elastic properties 10
    - 1.1.3.4 Alignment on a surface 10
    - 1.1.3.5 External electric fields 12
  - 1.1.4 Liquid crystals in this work: 5CB and E7 13
- 1.2 Silicon-on-insulator nanophotonics 13
  - 1.2.1 Waveguiding and more 14
    - 1.2.1.1 High index contrast waveguides 14
    - 1.2.1.2 CMOS compatibility 15
    - 1.2.1.3 Technology platform 15
  - 1.2.2 Integrated optical filter structures 15
    - 1.2.2.1 Ring resonators 16
    - 1.2.2.2 Ring resonator spectral properties 18
- 1.3 Conclusions 19
- References 20

2 Waveguiding and Liquid Crystals 23

- 2.1 Introduction 23
- 2.2 Liquid crystal as the waveguide 23

2.2.1 Waveguides with a LC core 24
2.2.2 Spatial solitons 24
2.3 Liquid crystal as (part of) the cladding 25
2.3.1 Slab waveguides 25
2.3.2 Strip waveguides 26
2.3.3 Liquid crystal-inflitrated photonic crystals and photonic crystal fibers 31
2.4 Conclusions 31
References 32

3 The Liquid Crystal Cell 37
3.1 Introduction 37
3.2 General Implementation 37
3.3 Assembly 39
3.4 Alignment 40
3.4.1 Introduction 40
3.4.2 Polarizing microscopy 41
3.4.3 Alignment on chip 43
3.5 Conclusions 45
References 46

4 Tuning Ring Resonators 47
4.1 Introduction 47
4.2 Practical measurement aspects 47
4.2.1 Setup overview 47
4.2.2 TE and TM grating couplers 49
4.3 TE Ring Resonators 50
4.3.1 Electrical tuning: top-bottom 52
4.3.1.1 Specifications of the device 52
4.3.1.2 Visual inspection 52
4.3.1.3 Tuning the resonance 53
4.3.2 Electrical tuning: in-plane switching 60
4.3.2.1 Specifications of the device 60
4.3.2.2 Visual inspection 60
4.3.2.3 Tuning the resonance 61
4.3.3 Temperature tuning 64
4.3.3.1 Tweaking the setup 64
4.3.3.2 Tuning the resonance 65
4.4 TM Ring Resonators 65
4.4.1 Specifications of the device 67
4.4.2 Tuning the resonance 68

4.5 Dynamic behaviour of electrical tuning 71
4.6 Conclusion 72
References 74

5 Simulating LC-clad waveguides **75**
5.1 Introduction 75
5.2 Simulation tools 75
  5.2.1 Director calculation 76
  5.2.2 Modesolver 78
5.3 General tuning mechanisms 80
  5.3.1 Top-bottom tuning 80
  5.3.2 In-plane switching 81
5.4 Anchoring strength 81
  5.4.1 Top-bottom tuning 82
  5.4.2 In-plane switching 84
5.5 Cell thickness 85
  5.5.1 Top-bottom tuning 85
  5.5.2 In-plane switching: gap between electrodes 85
5.6 Waveguide width 87
5.7 Match between simulations and experiments 89
  5.7.1 Top-bottom tuning 89
  5.7.2 In-plane switching 90
5.8 Conclusions 91
References 93

6 Trimming ring resonators with polymerizable LC **95**
6.1 Introduction 95
  6.1.1 Trimming of SOI ring resonators 95
  6.1.2 Polymerizable LC 96
    6.1.2.1 Photo-initiated polymerization 96
    6.1.2.2 LC polymers 97
    6.1.2.3 Applications 98
6.2 Mixture properties 99
  6.2.1 Materials 99
  6.2.2 Visual inspection 100
  6.2.3 Spectroscopy 101
    6.2.3.1 Thickness of the cell 101
    6.2.3.2 Refractive indices at one wavelength 104
    6.2.3.3 Birefringence 106
6.3 Trimming ring resonators 109
  6.3.1 Cells and setup 109

6.3.2 Measurements 109
6.4 Conclusions 112
References 113

7 Conclusions and Outlook 115
7.1 2006 to 2011 115
7.2 2012 and onwards 116
7.2.1 Wavelength tuning of different components 116
7.2.2 Maximizing the tuning range 117
7.2.3 Quantifying the power consumption 117
7.2.4 Large-scale fabrication and testing 118
7.3 Final conclusion 118

List of Acronyms

0-9

5CB	4-Cyano-4’-pentylbiphenyl

A

AC	Alternating Current
AWG	Array Waveguide Grating

C

CMOS	Complimentary metal-oxide-semiconductor

F

FP	Fabry Pérot
FSR	Free Spectral Range
FTTH	Fiber-To-The-Home
FWHM	Full Width Half Maximum

I

IPS	In-Plane Switching
IR	Infrared
ITO	Indium Tin Oxide

L

LC	Liquid Crystal
LCD	Liquid Crystal Display

M

MZI	Mach-Zehnder interferometer

P

PBG	Photonic Bandgap
PCF	Photonic Crystal Fiber

S

Si	Silicon
SiO2	Silicon dioxide
SOI	Silicon-on-Insulator

T

TBHQ	tert-butylhydroquinone
TE	Transverse electric
TIR	Total Internal Reflection
TM	Transverse magnetic

U

UV	UltraViolet

Nederlandse samenvatting –Summary in Dutch–

De toepassingen van licht zijn de laatste decennia veel ruimer geworden dan enkel verlichting. Net zoals elektriciteit, is licht een drager van informatie geworden en kent het toepassingen die gaan van optische sensoren (voor gassen, stress in materialen, temperatuur, ...) tot telecommunicatie. Licht kan gevangen en getransporteerd worden in golfgeleiders en verwerkt op zogenaamde fotonische geïntegreerde circuits. Vandaag kunnen die golfgeleiders op een dergelijk circuit extreem klein gemaakt worden, tot op een paar nanometer precies. Er wordt druk gewerkt om van fotonica een waardige aanvulling of zelfs concurrent te maken voor de elektronica.

De vermaarde CMOS technologie van de elektronica steunt in ruime mate op het materiaal silicium (Si). Dit is een relatief goedkoop materiaal en de fabricage van componenten uit Si gebeurt met mature technieken. De kennis van Si in de CMOS wereld is dan ook zeer uitgebreid. Si is ook transparant in het golflengtegebied dat voor telecommunicatie gebruikt wordt en het heeft een hoge brekingsindex. Dit heeft de interesse gewekt van onderzoekers actief in de fotonica en op dit moment is Si uitgegroeid tot het belangrijkste materiaal voor fotonische componenten. Silicium dioxide (SiO_2) is het oxide van Si en het heeft een veel lagere brekingsindex dan Si. Door het te combineren met Si zelf, kan een materiaalsysteem met een hoog brekingsindexcontrast gevormd worden, silicium-op-isolator (SOI). Het hoge contrast laat zeer kleine golfgeleiderstructuren toe. Golfgeleiders met bochten, kruisingen, (de-)multiplexers en filters zijn maar een paar voorbeelden van de veelheid aan structuren die reeds gefabriceerd werden. Er zijn echter een aantal toepassingsgebieden waar silicium tekort schiet. Een van die gebieden is het afstemmen in golflengte van fotonische structuren. De mogelijkheden tot golflengteafstembaarheid in silicium zelf zijn eerder beperkt. Vaak word gebruik gemaakt van microscopische warmte-elementen om dit probleem te omzeilen. Deze techniek gaat echter gepaard met een aanzienlijk vermogenverbruik. In dit werk onderzoeken we of vloeibare kristallen op een efficiënte manier gebruikt kunnen worden om SOI componenten af te stemmen in golflengte.

Vloeibare kristallen zijn materialen die een extra fase vertonen tussen de vaste en de vloeibare fase in. De moleculen van een vloeibaar kristal zijn vaak langwerpig en in de vloeibare kristalfase zijn ze geörienteerd volgens een gemeenschappelijke richting, de director. Het materiaal gedraagt zich macroscopisch nog steeds als een vloeistof. Het resultaat van deze gemeenschappelijke oriëntatie is een optische en diëlekrtische anisotropie. Er wordt immers een hoge diëlekrtische constante geassocieerd met de lange as van de molecule en een lage diëlekrtische constante met de korte assen. We zeggen dat het materiaal uniaxiaal is omdat een rotatie rond de lange as in een gelijke situatie resulteert. Wanneer er een extern elektrisch veld wordt aangelegd, oriënteert de director zich volgens de veldlijnen, wat een verandering in de optische eigenschappen van het materiaal teweeg brengt. Dit effect, samen met de grote anisotropie, willen wij gaan gebruiken om de resonantie van optische filters, meer bepaald ring resonators, af te stemmen in golflengte. Gezien de bijzondere eigenschappen van vloeibare kristallen, mikken we op een groot afstembereik en een laag vermogenverbruik.

Werkingsprincipe

Ring resonators zijn zeer efficiënte optische filters. Ze zijn ontworpen om een heel smal golflengtegebied te filteren uit een breed spectrum. Ring resonators bestaan uit een ringvormige golfgeleider die aan een rechte, "de bus", gekoppeld is. Voor golflenges die precies een geheel aantal keer in de ring passen, gaat de ring in resonantie. Dit will zeggen dat het gehele optisch vermogen in de ring te vinden is. Deze resonantiegolflengte hangt af van de effectieve brekingsindex van de mode die in de golfgeleider loopt. Die effectieve brekingsindex is een soort gewogen gemiddelde van de brekingsindices van de kern en de mantel van de golfgeleider. Wanneer de brekingsindex van een van de materialen in de mantel verandert, heeft dit meteen een effect op de effectieve brekingsindex. Wanneer we vloeibaar kristal gebruiken als toplaag, kunnen we met een extern elektrisch veld de resonantiegolflengte van een ring resonator wijzigen.

In onze componenten wordt het vloeibaar kristal gevangen tussen de SOI chip en een glazen plaatje. Die twee zijn aan elkaar vastgelijmd met UV-hardende lijm. In de lijm zitten kleine bolletjes met een specifieke diameter om de afstand tussen de chip en het glazen plaatje te controleren. Capillaire krachten trekken het vloeibaar kristal in de caviteit. Een laag indium tin oxide (ITO) op het glazen plaatje zorgt voor de mogelijkheid om elektrisch te contacteren. Er is ook een alignatielaag op dat plaatje aanwezig die de director een initiële oriëntatie geeft.

Op het oppervlak van de chip aligneert het vloeibaar kristal zich langsheen de golfgeleiders. Dit kunnen we zien met een polarisatiemicroscoop. De director

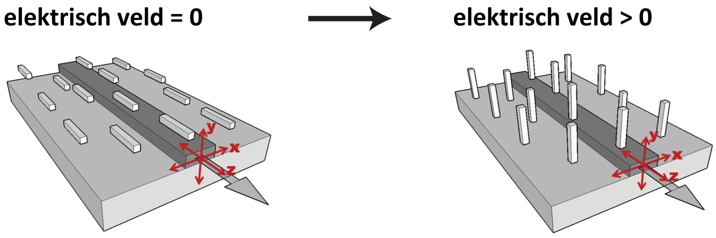

Figuur 1: Heroriëntering van een vloeibaar kristal toplaag op een SOI golfgeleider.

kan de ringvormige golfgeleider volgen en het schema van Figuur 1 is een goede benadering van de realiteit. Deze oriëntatie geeft de mode een initiële effectieve brekingsindex. Wanneer we een elektrisch veld aanleggen tussen de ITO laag en het Si substraat, oriënteert de director zich vertikaal en veranderen de optische eigenschappen in de toplaag. Op dit punt maken we een onderscheid tussen de fundamentele TE en de fundamentele TM mode.

- **TE mode.** De TE mode (Transversaal Elektrisch veld) zit heel sterk opgesloten in de kern van de golfgeleider, maar door de staarten van de mode die zich in de mantel uitstrekken, is er toch interactie met de materialen in mantel mogelijk. De x- en z-componenten van het elektrische veld van de mode zijn alletwee aanzienlijk in grootte en hebben dus beide invloed op de effectieve brekingsindex. Maar hoe verandert die toplaag nu precies? Zonder elektrisch veld, liggen de moleculen langsheen de golfgeleiders. De x-component ziet de korte as van de moleculen en de z-component de lange. Wanneer de moleculen onder invloed van een elektrisch veld verticaal gaan staan, zien zowel de x- als de z-component de korte as. De afnemende bijdrage van de z-component zorgt voor een daling van de effectieve brekingsindex en van de resonantiegolflengte.

- **TM mode.** De TM mode (Transversaal Magnetisch veld) is veel minder gebonden aan de kern van de golfgeleider en we verwachten dat de interactie met de toplaag veel groter zal zijn. Het elektrisch veld van de TM mode is voornamelijk langsheen de y-as gepolariseerd. Wanneer we een extern elektrisch veld aanleggen, oriënteert de director zich volgens de y-as met een stijgende effectieve brekingsindex tot gevolg. Wanneer een ring resonator de TM mode geleidt, zal de resonantiegolflengte stijgen voor een stijgende sterkte van het extern aangelegd elektrisch veld. We verwachten ook dat het afstembereik groter gaat zijn dan voor ringen die de TE mode geleiden vanwege de lagere binding van de mode aan de kern.

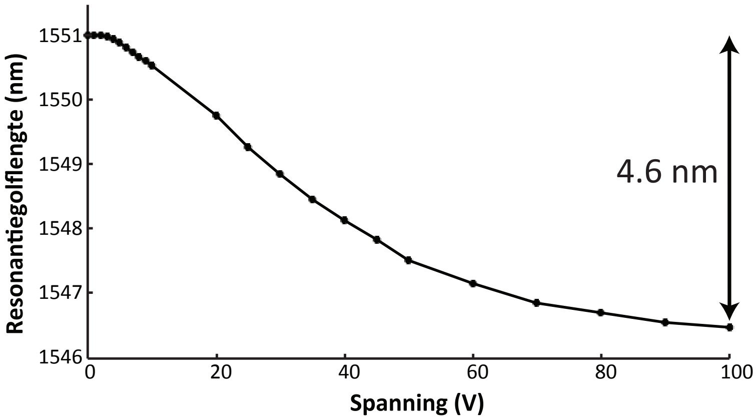

Figuur 2: De resonantie van een TE ring kan afgestemd worden over 4.6 nm naar kortere golflengtes.

Resultaten

We hebben componenten gemaakt die ring resonatoren (voor zowel de TE als de TM mode) met een vloeibaar kristal toplaag bevatten. De busgolfgeleider is uitgerust met roosterkoppelaars om licht eenvoudig in en uit te koppelen met behulp van optische vezels. Als lichtbron gebruiken we een afstembare laser en om het uitgaande vermogen op te meten, gebruiken we een vermogendetector. Wanneer we ook een spanningsbron gebruiken en aankoppelen aan zowel de ITO laag als aan het substraat, kunnen we een elektrisch veld aanleggen over de toplaag. We zijn erin geslaagd de resonanties van TE ringen af te stemmen over 4.6 nm naar kortere golflengtes, zoals in figuur 2. De resonanties van de TM mode kunnen afgestemd worden naar langere golflengtes over een bereik van 31 nm, zoals in figuur 3.

Om deze componenten te kunnen simuleren hebben we een berekening van de director gecombineerd met een modeberekening die volledige anisotropie ondersteunt. Deze combinatie behaalt goede resultaten aangezien de simulaties goed overeenkomen met de meetresultaten. Dit toont dat we de mechanismes in onze componenten zeer goed begrijpen.

We hebben ook gebruik gemaakt van polymeriseerbaar vloeibaar kristal om ring resonators eenmalig af te stemmen in golflengte. Ze zijn dan voor eens en voor altijd gefixeerd op deze golflengte, ook wanneer de spanningsbron afgekoppeld wordt. Dit is handig om fabricagefouten te compenseren. Polymeriseerbare vloeibare kristallen gedragen zich onder normale omstandigheden zoals gewone vloeibare kristallen. Echter, wanneer ze blootgesteld worden aan UV licht, gaan

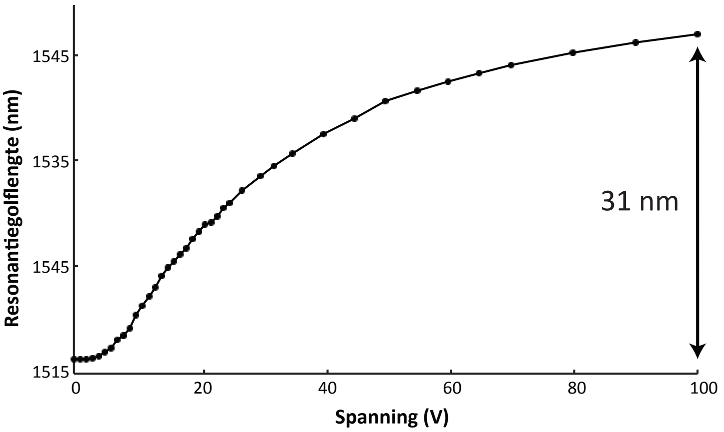

Figuur 3: De resonantie van een TM ring kan afgestemd worden over 31 nm naar langere golflengtes.

de moleculen bindingen met elkaar aan en vormen ze een hecht netwerk. Het materiaal is dan niet langer vloeibaar, maar de orientatie van de moleculen wordt in ruime mate behouden. Deze piste vereist nog meer onderzoek, maar wij hebben alvast aangetoond dat polymeriseerbare vloeibare kristallen gebruikt kunnen worden om resonanties vast te zetten op een vooraf gekozen golflengte.

English summary

During the past decades, the use of light has extended beyond mere illumination. Like electricity, it has become a carrier of information and is used in numerous applications ranging from sensing (gas, biomolecules, stress, temperature, ...) to telecommunication. Light can be transported by waveguides and manipulated on a so-called ’photonic’ integrated circuit (PIC). At present, the waveguide structures on such a circuit can be made extremely small and a lot of effort is being done to make ’photonics’ a true competitor for electronics.

Electronics’ CMOS technology relies largely on silicon, a relatively cheap material that can be processed with well-known techniques. Needless to say that the know-how concerning silicon is extensive. As it is transparent around telecom wavelengths and benefits from a high refractive index, silicon has sparked considerable interest among photonics researchers. And as it turned out, silicon has become one of the major materials in this field. Combined with its oxide, it forms the high index-contrast system silicon-on-insulator (SOI) which can be used to make waveguide structures on a very small scale. Waveguide bends, crossings, (de-)multiplexers en filters are only a few examples of structures that have been fabricated. However, there are some specific areas for which silicon can not provide the desired functionality. Among these is wavelength tuning of optical components. Silicon’s intrinsic tuning capabilities are not great and methods to circumvent this (e.g. by heating) often use a lot of power or remain limited in tuning range. In this work, we investigate the use of liquid crystals to tune SOI components.

Liquid crystals (LC) are materials that exhibit an extra phase between the solid and the liquid phase. Typically, the molecules are elongated and in the liquid crystalline phase, they share a common orientation, the director, while retaining the macroscopic properties of a fluid. Optical and dielectric anisotropy result from the common orientation as different dielectric constants are associated with the long and the short axes of the molecules. The LC is said to be ’uniaxial’. In the presence of an external electric field, the director reorients along the fieldlines, altering the optical properties of the LC. We want to use the electrooptical effect, combined with the huge anisotropy of many LCs to tune the resonance wavelength of optical filters, more in particular ring resonators.

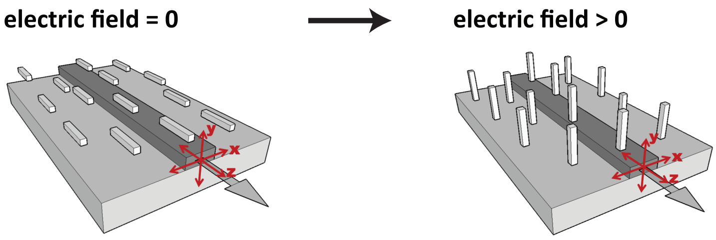

Figure 1: Reorientation of the LC cladding.

Given the extraordinary properties of LC, we aim for a wide tuning range and low power tuning.

Working Mechanism

Ring resonators are efficient optical filters designed to filter out a very small wavelength band from a broad spectrum. They consist of a ring-shaped waveguide coupled to a straight waveguide. For certain wavelengths the ring is in resonance and all the optical power is located inside the ring waveguide. This resonance wavelength depends on the waveguide mode's effective index, which can be seen as a weighted average of the refractive indices of the waveguide and its cladding. If the optical properties of one of the cladding materials change, this will have an effect on the position of the resonance. When we apply LC as a top cladding on the waveguide, we are able to influence the resonance wavelength with an externally applied electric field.

In our devices, LC is caught between the SOI chip and a glass plate. The chip and the glass plate are glued to each other with UV-curable glue mixed with spacers. The LC can be drawn in the gap by capillary forces. On the glass plate, there is a transparent indium tin oxide (ITO) and a spincoated alignment layer present. The ITO is used for contacting while the alignment layer provides an initial preferenial orientation for the director.

When we study an SOI chip with LC top cladding with a polarizing microscope, we see that the LC aligns to the waveguides on the chip. It is able to follow the ring waveguide and in good approximation the LC is oriented parallel to each waveguide (Figure 1). This orientation can be associated with the initial effective index of the mode. When an electric field between the silicon substrate and the ITO layer is applied, the director will reorient vertically, changing the optical properties of the cladding. Here we make a distinction between the fundamental TE and the fundamental TM mode.

- **TE mode.** The TE mode (Transverse Electric field) is highly confined to the waveguide core. Through its evanescent tails, however, it can still interact with the cladding layers. The x- and z-components of the electric field of the mode are both considerable in magnitude and will both have a large influence on the effective index. Now let's consider the change in the cladding. Without an electric field present, the LC molecules present their short axis to the x-component of the electric field of the mode and their long axis to the z-component. When reoriented by an electric field, they present their short axis to both x- and the z-component. The z-component will contribute to a decreasing effective index. When we translate this to the resonance of a ring resonator, we expect that this resonance will shift towards lower wavelengths.

- **TM mode.** The TM mode (Transverse Magnetic field) is far less confined to the core and interaction with the cladding layers is greatly enhanced. The electric field of the TM mode is mainly polarized along the y-axis. When an electric field is applied, the molecules align themselves along the y-axis and an increasing effective index results. A ring resonator guiding the TM mode will boast resonance wavelengths shifting towards longer wavelengths for increasing strength of the external electric field. We expect the tuning range to be bigger than for the TE mode given the lower confinement of the TM mode.

Results

We have fabricated devices that contain both TE and TM guiding ring resonators clad with a layer of LC. The bus waveguides are equipped with grating couplers to easily couple light in from and out to an optical fiber. As a light source we use a tunable laser and the output power is detected with a power meter. A voltage source is connected to the ITO layer and the Si substrate in order to generate an electric field over the LC cladding. We have found that the resonances of ring resonators guiding the TE mode can be tuned 4.6 nm towards shorter wavelengths (Figure 2). The tuning range of ring resonators guiding the TM mode is 31 nm (Figure 3).

We have combined a director calculation with a fully anisotropic mode solver to simulate SOI waveguides with a LC cladding. The simulation results match the experiments closely, showing that the mechanism is well understood.

We have also worked with polymerizable LC to trim the resonance of ring resonators. Rather than constantly tuning and re-tuning, trimming is a process

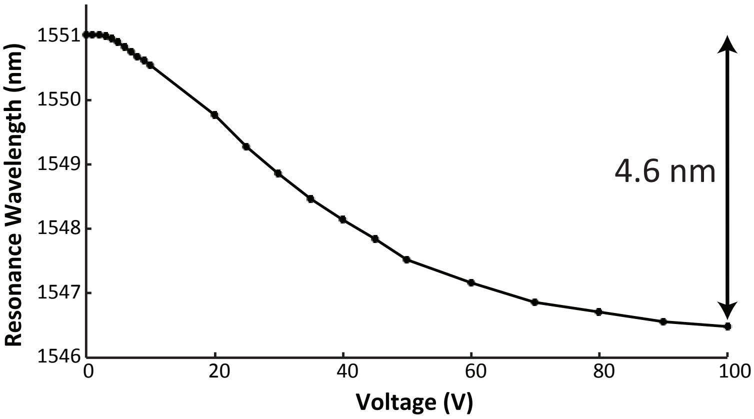

Figure 2: Resonance wavelength of a ring resonator guiding TE light as a function of voltage.

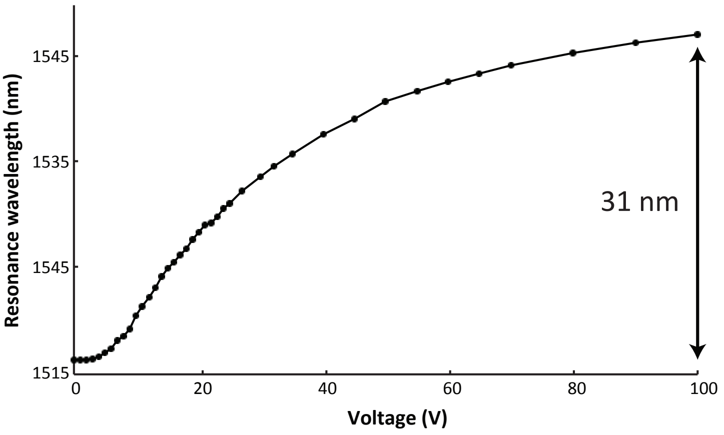

Figure 3: Resonance wavelength of a ring resonator guiding TM light as a function of voltage.

performed only once to fix the resonance to a desired wavelength. This is useful to compensate for the mismatch between the designed parameters of the ring resonators and those after fabrication. Polymerizable LCs behave like regular LCs until they are exposed to UV light. Then, the molecules are linked in a network and the material solidifies, while retaining the molecular ordering. Although more research is needed, we have shown that ring resonators can be trimmed with this method.

1

Introduction

Many PhD dissertations in the field of photonics start with describing the information age, the rapid growth of the internet during the past decade and the urge and push to go ever faster when it comes to telecommunication. And the facts are indeed impressive. The capacity of optical fibers increases on a regular basis, reaching currently up to 112 Tb/s [1]. Stretching all over the world, these fibers hand us the possibility to watch movies, listen to music, take part in video-conferencing,... over the internet, together with billions of other information junkies. In an increasing number of countries, the optical information stream is brought straight into the homes of the FTTH (fiber-to-the-home) subscribers. Long-haul networks, however, are not the only field in which optical communication has taken leaps forward. At the other end of the spectrum, extremely small nanophotonic structures integrated on a chip pave the road for on-chip short-range optical communication.

It is easy to forget that these great new technologies are based on many years of basic, almost fundamental research. Even when a material has been used for years, novel properties and applications can be found. It is here, at this almost-fundamental level that most of the work in this PhD has been carried out. The materials involved, silicon-on-insulator (SOI) and liquid crystals (LCs), are known and have been studied for decades, but the effects of their combination were at the beginning of this work still a bit of a mystery. We set ourselves a goal: to understand the interaction of SOI waveguides and LCs and work towards a real application, being widely tunable photonic devices.

The thesis

Silicon is and has been one of the major materials for photonics. While it has numerous qualities such as the high refractive index and the compatibility with CMOS technology, there are some serious drawbacks. One of these shortcomings is the lack of efficient tunability in the material. Integrated resistive heaters provide a way to circumvent this problem, but they require considerable power. In this work we look for a way to tune silicon photonic components over a wide range with low power. This can lead to widely tunable filters, lasers and other integrated components on silicon.

Liquid crystals have unique optical properties of which the huge anisotropy is one of the most striking. As the optical properties are also electrically tunable, liquid crystals could in theory be very interesting for use in tunable photonic devices. The goal of this work is to integrate LCs as a cladding layer on SOI ring resonators and make their filter characteristics tunable. We aim to exploit the anisotropy maximally and to achieve a tuning range which is wider or at least of the same order of magnitude as competing technologies such as e.g. heating. Furthermore, we want to gain a thorough understanding of the underlying mechanisms so as to be able to predict the behaviour of the tunable ring resonators.

The thesis:
Integrated optical filters in general and ring resonators in particular can be tuned over a wide wavelength range when they are clad with a layer of liquid crystals to which an external electric field is applied.

Overview of this book

In the remaining sections of this introductory chapter, we will introduce the two pillars on which this work is founded: liquid crystals and silicon photonics. A reader less familiar with one or both of these technologies will hopefully gain enough insight to proceed with chapter 2 where we discuss the combination of optical waveguides and liquid crystals. In chapter 3 we describe the fabrication details of our devices, the test "cells". Chapter 4 dives deep into the measurements that we performed. With the knowledge acquired in the first chapters we are able to understand the results intuitively. Nevertheless, in chapter 5 we lay bare all the tuning secrets with numerical simulations. Chapter 6 takes a small detour. Here we will explain how the resonance of ring resonators can be trimmed using polymerizable LC. We explain the working principles and present our experiments. Finally, chapter 7 sums up the conclusions that can be drawn from this work and looks ahead at possibilities for further research.

1.1 Liquid crystals

Liquid crystals are everywhere. We can find them at home, at the office, in the car. We look at them when we watch television, check our e-mail, play "Angry Birds" on our smartphone, make a quick calculation with an old-fashioned calculator or check the time on the car dashboard. Where does this material come from and why is it called like that? In this section we provide the answers and explore various properties of liquid crystals.

1.1.1 Liquid or crystal?

The story starts in 1888, when Frederick Reinitzer heated cholesteryl benzoate. He noticed that at 145.5^{o}C the solid material became a turbid liquid. When heated furter to 178.5^{o}C the liquid became clear. In other words, he saw an intermediate phase of the material in between the solid and the liquid phase. In this phase, the material can flow freely like a liquid as the molecules don't have a fixed position. There is, however, some degree of order in the material. The molecules show a common orientation over a region far larger than a single molecule. This is a property usually only seen in solid, crystalline materials. As it displays properties from both liquids and solid crystals, this class of materials has been named liquid crystals and the additional phase the liquid crystalline phase. What was at first a curiosity to scientists has lead to an enormous research effort and liquid crystals (LC) have gained an important place in modern display technology and photonics applications.

1.1.2 Liquid crystal types

The liquid crystal discovered by Reinitzer is a thermotropic liquid crystal. This means that the factor that determines whether or not the material is in the liquid crystalline phase, is temperature. When the temperature is too high, the thermal motion becomes too strong for the liquid crystalline phase to be sustainable. As the temperature drops, the interaction between the molecules will eventually be strong enough to overcome the thermal motion and the common orientation appears. The other class of LC that we briefly touch upon here is lyotropic LC. Here, molecules are dispersed in a solvent and the liquid crystalline phase appears only if the concentration of molecules is high enough. Lyotropic liquid

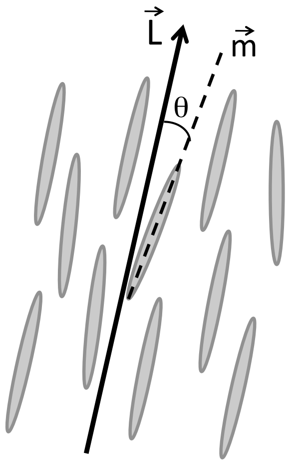

Figure 1.1: In the nematic LC phase, the molecules are oriented along a common director ($\bar{L}$). Their long axis $\bar{m}$ can be at a small angle θ with $\bar{L}$

crystals have found their way mainly in biological applications. In the rest of this work we will focus on thermotropic liquid crystals.

1.1.2.1 Thermotropic liquid crystals

Thermotropic liquid crystals are often composed of elongated, rod-like molecules. At high temperatures they form an ordinary isotropic fluid. The thermal motion is high and the orientation of the molecules random. When the temperature drops, the interaction between the molecules overcomes the thermal motion and a certain order appears although the material still behaves as a liquid. Some liquid crystals exhibit an orientational order. The molecules are randomly positioned with respect to one another but they "point" in the same direction. This is the so-called **nematic** phase and the molecules are oriented along the **director** $\vec{L}$. Some liquid crystals exhibit a phase where there is not only orientational but also a positional order. This is the **smectic** phase. The molecules are lined up in smectic planes. We make a distiction between the smectic A and the smectic C phase (Figure 1.2). In the smectic A phase the normal of the smectic planes coincides with the director. The molecules can freely rotate around the director. This is no longer possible in the smectic C phase where the director makes an angle with the normal of the smectic layers.

Besides these elongated molecules, there are LCs with molecules in other shapes, giving rise to different orderings. Chiral molecules, for example, are elongated molecules without mirror symmetry. They can lead to the formation

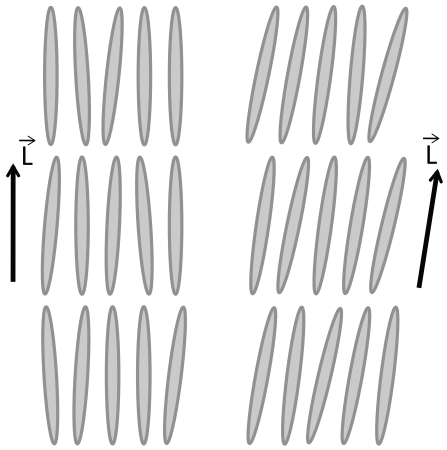

(a) (b)

Figure 1.2: (a) In the smectic A phase, the molecules are organised in smectic planes. The director is along the normal of the planes and the molecules have the freedom to rotate around the director. (b) In the smectic C phase this is no longer possible as the director is at an angle with the normal of the smectic planes.

of helices in the chiral nematic phase. These LCs are also known as cholesteric LCs. Disk-like molecules can form columnar phases (Figure 1.3(a)) while curved molecules may exhibit yet another type of ordering (Figure 1.3(b)).

1.1.3 Nematic liquid crystals in detail

In this work, thermotropic nematic liquid crystals are used. This type of LC is most commonly found in display technology and photonics. The elongated molecules typically consist of two or more aromatic rings connected by a linkage group. Attached to the rings are a side chain and a terminal group. Each part of the molecule influences the behaviour of the LC. The aromatic rings are responsible for the molecular interaction needed for the nematic phase to occur. The linkage group determines the stability of the molecule against e.g. UV illumination. The terminal group determines the dielectric constant of the LC and its anisotropy while the side chain influences the elastic characteristics and the clearing temperature (T_c) at which the nematic phase dissapears into the isotropic phase. In Figure 1.4 you can see a schematic representation of a nematic molecule and the structure of 5CB, a nematic LC widely used in display technologies.

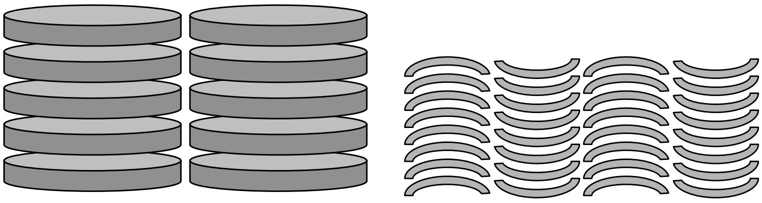

(a) (b)

Figure 1.3: (a) Disk-like molecules can organise themselves in columnar stacks. (b) Banana-shaped LC molecules can lead to positional ordering.

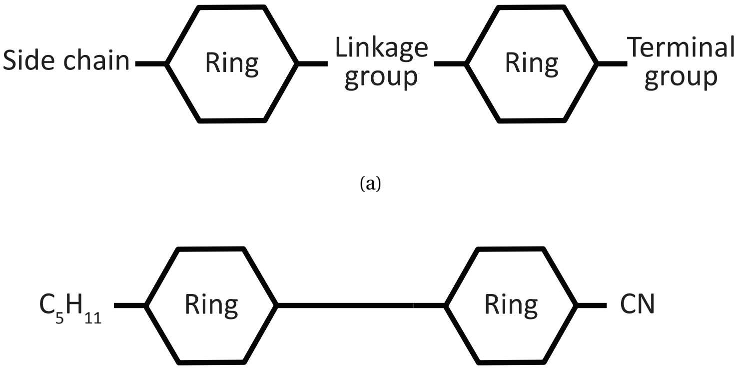

(a)

(b)

Figure 1.4: (a) Schematic view of a typical nematic LC. (b) Schematic view of a 5CB molecule.

The nematic LC phase has a uniaxial symmetry which means that rotating around the director results in an equivalent situation. Herein lie the many possibilities for displays and photonic applications. Light that propagates along the director can behave in a different fashion than light propagating in a plane perpendicular to the director.

1.1.3.1 Order parameter

Above T_c the nematic LC is actually an isotropic liquid. The thermal energy is too large to allow molecular interactions to form a common orientation. There is no director and no nematic behaviour. When the temperature drops, the brownian motion decreases and below T_c the thermal energy is low enough for the orientational order to appear. The molecules align and the director appears. The individual molecules are of course not perfectly still, their orientation fluctuates somewhat around the director. With decreasing temperatures, these fluctuations become less severe. The order parameter S is a means to indicate easily how strong the molecular interactions are with respect to the thermal energy.

$$S = \frac{1}{2}\left\langle 3(\bar{m}\cdot\bar{L})^2 - 1\right\rangle = \frac{1}{2}\left\langle 3cos^2\theta - 1\right\rangle \tag{1.1}$$

θ is the angle between the long axis of the molecule ($\bar{m}$) and the director. We average over a volume to obtain S. In the isotropic phase the molecules are oriented randomly. For a molecule oriented along the director, $\bar{m}\cdot\bar{L}$ is 1 while it is 0 for a molecule oriented along one of the two other main axes. The order parameter S will therefore be 0. Below T_c, S increases with decreasing temperature. When the molecules all are perfectly oriented along the director, S equals 1.

1.1.3.2 Dielectric and optical anisotropy

Nematic liquid crystals are uniaxial materials. As was said above, this means that the molecules can rotate around their long axis without changing the material properties. They have one long axis and two equivalent short axes. Their dielectric permittivity tensor can be written as

$$\bar{\bar{\epsilon}} = \begin{bmatrix} \epsilon_\perp & 0 & 0 \\ 0 & \epsilon_\perp & 0 \\ 0 & 0 & \epsilon_{||} \end{bmatrix}. \tag{1.2}$$

In the xyz coordinate system (Figure 1.5), this becomes [2]

$$\bar{\bar{\epsilon}} = \begin{bmatrix} \epsilon_\perp + \Delta\epsilon sin^2\theta cos^2\phi & \Delta\epsilon sin^2\theta sin\phi cos\phi & \Delta\epsilon sin\theta cos\theta cos\phi \\ \Delta\epsilon sin^2\theta sin\phi cos\phi & \epsilon_\perp + \Delta\epsilon sin^2\theta sin^2\phi & \Delta\epsilon sin\theta cos\theta sin\phi \\ \Delta\epsilon sin\theta cos\theta cos\phi & \Delta\epsilon sin\theta cos\theta sin\phi & \epsilon_\perp + \Delta\epsilon cos^2\theta \end{bmatrix}, \tag{1.3}$$

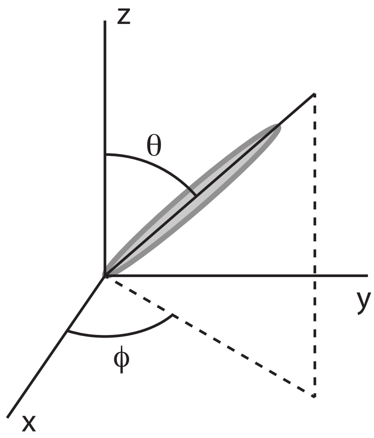

Figure 1.5: Tilt (θ) and twist (ϕ) in the xyz coordinate system.

with $\Delta\epsilon = \epsilon_{||} - \epsilon\perp$. $\Delta\epsilon$ can be positive or negative, depending on the molecule itself.

Light is essentially composed of electric (and magnetic) fields but the optical frequencies are much higher than frequencies applied by external voltage sources. The dielectric constants for optical frequencies are much lower than for frequencies in the kHz range. Therefore we work with the refractive index for optical waves rather than with the dielectric constants. The refractive indices of the LC are

$$n_e = \sqrt{\frac{\epsilon_{||}}{\epsilon_0}} \tag{1.4}$$

$$n_o = \sqrt{\frac{\epsilon_{\perp}}{\epsilon_0}}, \tag{1.5}$$

n_e is called the extraordinary refractive index and is the refractive index for light polarized along the long axis of the molecule. n_o is the ordinary refractive index for light polarized perpendicular to the long axis. $\Delta n = n_e - n_o$ is called the optical anisotropy.

Let us take a look at a plane wave propagating through a nematic LC. To understand what happens, we represent light by an electric field. This field is a superposition of two electric field components oscillating perpendicular to each other and to the propagation direction (z-axis) of the light. In an isotropic medium with refractive index n, these components can be written as:

$$E_x = a_x cos\left[2\pi\nu\left(t - \frac{nz}{c}\right) + \phi_x\right] \tag{1.6}$$

$$E_y = a_y cos\left[2\pi\nu\left(t - \frac{nz}{c}\right) + \phi_y\right] \tag{1.7}$$

v, a and ϕ denote frequency, amplitude and phase. The electric field of the light is then

$$E(z,t) = E_x \bar{x} + E_y \bar{y}. \tag{1.8}$$

Associated with the electric field is a vector in the plane perpendicular to the propagation direction. At each z-position, this wave vector denotes the amplitude and direction of the field. In isotropic media, the endpoint of the vector describes an ellips while the light propagates. This ellips is the polarization of the light. Equations 1.6 and 1.7 describe the ellips,

$$\frac{E_x^2}{a_x^2} + \frac{E_y^2}{a_y^2} - 2cos\phi \frac{E_x^2 E_y^2}{a_x^2 a_y^2} = sin^2\phi, \tag{1.9}$$

with ϕ the phase difference. It is the superposition of two linear polarizations (associated with each of the electric field components) that have an equal oscillation frequency but lag behind each other (phase difference). Depending on the phase difference and the amplitude of the field components, the resulting polarization is elliptical in the general case but can also be circular ($\phi = \pm\pi/2$ and $a_x = a_y$) or linear ($\{a_x$ or $a_y = 0\}$ or $\{\phi = 0$ or $\pi\}$).

In an anisotropic medium, the following equation for the electric flux density holds:

$$D_i = \sum_j \epsilon_{ij} E_j, \tag{1.10}$$

where i, j = 1, 2, 3 indicate the x, y and z components. We can always find a coordinate system for which the off-diagonal elements of the permittivity tensor are 0.

$$\bar{\bar{\epsilon}} = \begin{bmatrix} \epsilon_1 & 0 & 0 \\ 0 & \epsilon_2 & 0 \\ 0 & 0 & \epsilon_3 \end{bmatrix} \tag{1.11}$$

The refractive indices along the axis are

$$n_1 = \sqrt{\frac{\epsilon_1}{\epsilon_0}}, \qquad n_2 = \sqrt{\frac{\epsilon_2}{\epsilon_0}}, \qquad n_3 = \sqrt{\frac{\epsilon_3}{\epsilon_0}}. \tag{1.12}$$

In the rest of the chapter we assume that the main axes of the molecules of the anisotropic medium are along the x, y and z axes. From Maxwell's equations, it follows that for a plane wave travelling in the anisotropic medium

$$\bar{k} \times (\bar{k} \times \bar{E}) + \omega^2 \mu_o \bar{\epsilon} \bar{E} = \bar{0}, \tag{1.13}$$

where ω is the pulsation $2\pi v$. This translates to [3]

$$\begin{bmatrix} n_x^2 k_0^2 - k_y^2 - k_z^2 & k_x k_y & k_x k_z \\ k_y k_x & n_y^2 k_0^2 - k_x^2 - k_z^2 & k_y k_z \\ k_z k_x & k_z k_y & n_z^2 k_0^2 - k_x^2 - k_y^2 \end{bmatrix} \begin{bmatrix} E_x \\ E_y \\ E_z \end{bmatrix} = \begin{bmatrix} 0 \\ 0 \\ 0 \end{bmatrix}, \tag{1.14}$$

where $k_i = \frac{n_i \omega}{c}$ are the components of the wave vector $\bar{k}$ and $k_0 = \frac{\omega}{c}$. The equations have a non-trivial solution when the determinant of the matrix is zero, resulting in the dispersion relation.

Suppose a plane wave travelling along the z axis ($\bar{k} = [0, 0, \frac{\omega n}{c}]$) in a liquid crystal with the director along the x axis. The wave is polarized in the x-y plane, so the polarization can be split up into two linear components along the x and y axis. From equation 1.14 it is found that the dispersion relation reduces to

$$\begin{vmatrix} \frac{n_e^2 \omega^2}{c^2} - \frac{n^2 \omega^2}{c^2} & 0 & 0 \\ 0 & \frac{n_0^2 \omega^2}{c^2} - \frac{n^2 \omega^2}{c^2} & 0 \\ 0 & 0 & \frac{n_o^2 n^2 \omega^2}{c^2} \end{vmatrix} = 0, \tag{1.15}$$

and eigenmodes of the polarization have a refractive index of n_e and n_o. The eigenmodes travel at a different speed through the LC and after a length d, the difference in phase has become

$$\Gamma = k_0(n_e - n_o)d = k_0 \Delta n d, \tag{1.16}$$

where Γ is known as the phase retardation. As the two linear eigenmodes of the polarization travel through the LC at a different speed, the polarization of the light wave changes continuously, except when the light is in one eigenmode only. For example, for a thickness $d = \frac{\pi}{k_0 \Delta n} = \frac{\lambda}{2 \Delta n}$, the phase retardation becomes π. An initial linear polarization results in again a linear polarization mirrored compared to the optical axis, which is the axis representing the direction of the extraordinary refractive index.

1.1.3.3 Elastic properties

Any variation in the director orientation can be seen as a superposition of three basic deformations: splay, twist and bend (Figure 1.6). The sum of the energies, stored in each of the three deformations, is the total elastic energy density in a nematic liquid crystal expressed in the Frank-Oseen expression [4]:

$$f_{elastic} = \frac{K_{11}}{2} \left| \nabla \cdot \bar{L} \right|^2 + \frac{K_{22}}{2} \left| \bar{L} \cdot \nabla \times \bar{L} \right|^2 + \frac{K_{33}}{2} \left| \bar{L} \times (\nabla \times \bar{L}) \right|^2, \tag{1.17}$$

with K_{11}, K_{22} and K_{33} the splay, twist and bend constants. These constants give an indication of how easy the elastic deformations can occur in a nematic LC. In general K_{22} is the lowest of the constants and twist can occur the easiest.

1.1.3.4 Alignment on a surface

When the LC is in contact with a surface, the director will align itself to the surface in a way that is dependent on the structural or chemical properties of

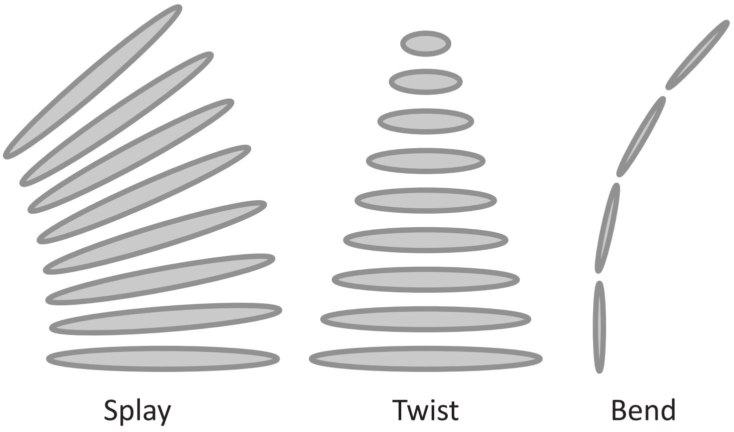

Figure 1.6: The three basic elastic deformations of the director are splay, twist and bend.

the surface. With careful treatment of the surface, it is possible to impose a well-defined alignment of the director. Typically this includes adding a thin alignment layer on the surface. There are several examples found in literature of how this can be done. A polymer layer, for example, rubbed with a piece of cloth can align the director along the rubbing direction and give it a small initial tilt as well (Figure 1.7). Other examples are oblique evaporation of SiO_2 [5–8] or photoalignment [9]. In this last method, a photosensitive layer is applied to the surface. Illuminating this layer with polarized UV light will induce a preferential direction along the polarization of the light. But also on untreated surfaces, the director will align itself in some way to the surface. It can align in a planar fashion to the surface without a preference for an orientation in the plane. This will lead to the forming of several very small domains with different azimuthal orientation. Another possibility is that the director aligns perpendicular to the surface (homeotropic alignment). It is clear that a non-uniform or structured surface can lead to very complicated director alignment patterns. At the surface, the anchoring strength determines to what extent deviations from the preferential direction are allowed. Strong anchoring allows no reorientation, while weak anchoring does, in which case a surface energy appears [4].

$$f_{surface} = \frac{K_s}{2}\left[1-(\bar{L}\cdot\bar{L}_{pref})\right], \tag{1.18}$$

K_s being a constant expressed in J/m^2.

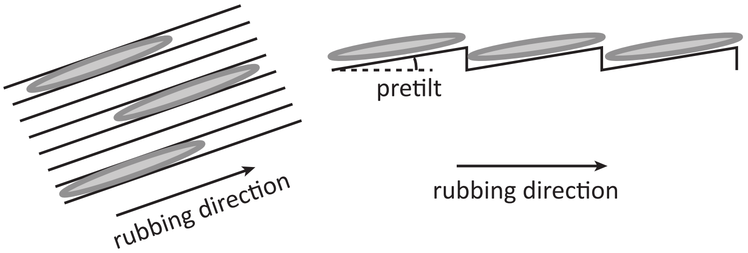

Figure 1.7: Schematic top and side view of a polymer rubbing layer, buffed with a cloth. The molecules align along the rubbing direction and get a pretilt angle.

1.1.3.5 External electric fields

The dielectric anisotropy implies that electric fields oscillating along the long axis of the molecules see a different dielectric constant than electric fields oscillating along one of the short axes. Due to this anisotropy, the dielectric displacement $\bar{D}$ is in general not parallel to the electric field $\bar{E}$.

$$\bar{D} = \epsilon_0 \left[\epsilon_\perp \bar{E} + \Delta\epsilon(\bar{E}\cdot\bar{L})\bar{L}\right], \tag{1.19}$$

with $\Delta\epsilon = \epsilon_{||} - \epsilon_\perp$. Resulting from this, a torque is exerted on the molecules in the presence of an electric field. When a LC slab is positioned between two electrodes with a certain voltage difference, the electric energy density can be written as [10]

$$f_{electric} = -\frac{1}{2}\bar{D}\cdot\bar{E} = -\frac{1}{2}\epsilon_0\left[\epsilon_\perp\bar{E} + \Delta\epsilon(\bar{E}\cdot\bar{L})\bar{L}\right]\cdot\bar{E} \tag{1.20}$$

As the system strives for a minimization of the energy, it can be seen from equation 1.20 that for a positive $\Delta\epsilon$, the director $\bar{L}$ will try to orient itself along $\bar{E}$ (Figure 1.8) while for a negative $\Delta\epsilon$ it does so perpendicular to $\bar{E}$. From equation 1.20 it is clear that the direction of the E-field (+ or -) is not important as the E-field appears squared.

Fréedericksz transition

An electric field introduces a polarization in a polarizable molecule. In nematic LCs with a positive $\Delta\epsilon$, as used in this work, this results in a dipole oriented parallel to the long axis of the molecule. The molecules start reorienting in order to align this dipole parallel to the electric field. This reorientation is called the Fréedericksz transition. When the director is perpendicular to the electric field, a threshold voltage is needed for the Fréedericksz transition to occur. When this is not the case, this threshold strictly speaking disappears.

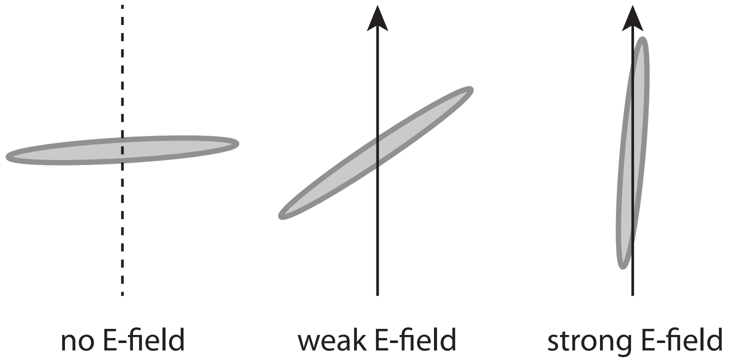

Figure 1.8: An electric field will cause a torque on molecules that are not aligned with the field. Due to this torque the director aligns itself to some degree to the field.

1.1.4 Liquid crystals in this work: 5CB and E7

We work with the well-known commercially available liquid crystals 5CB and E7. Both are regularly used in display technology. In the table below, we list the most relevant parameters: the clearing temperature and the ordinary and extraordinary refractive indices (at room temperature) [11–13].

	5CB	**E7**
T_c	$34^o C$	$59^o C$
n_e	1.7	1.69
n_o	1.52	1.5

Except for the clearing temperature, the two LCs are very similar.

1.2 Silicon-on-insulator nanophotonics

Silicon has been around for many years as the backbone material of CMOS technology. Over the past years, silicon has become one of the (if not *the*) most important materials in integrated photonics as well. Such integrated components include waveguides [14, 15], photodetectors [16] and high-speed modulators [17]. In this section we introduce silicon and silicon-on-insulator (SOI) for photonics and briefly discuss optical filter structures in SOI.

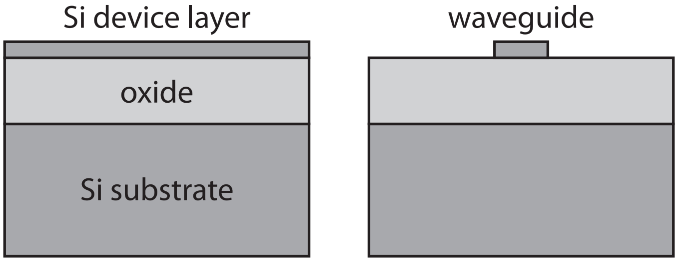

Figure 1.9: Left: a cross section of the SOI stack, right: waveguides are defined in the device layer.

1.2.1 Waveguiding and more

Silicon is a material with an indirect bandgap. It would seem that this makes it unattractive for photonic applications as it is useless as a light emitter. However, it has several advantages that have propelled it to the forefront of photonics research. It is transparent for wavelengths between 1300 nm and 1620 nm, the wavelength band of (long-haul) optical communications. Furthermore, Si has a very high refractive index compared to its oxide SiO_2 (3.45 and 1.45 respectively, at optical frequencies) allowing for very small optical waveguides. The fabrication of SOI photonic structures is also compatible with the well-known techniques of CMOS technology.

1.2.1.1 High index contrast waveguides

In an SOI stack (Figure 1.9), the thin Si layer in which the structures are defined, is separated from the Si substrate by a layer of SiO_2. This buried oxide layer prevents leakage of light from the device layer to the substrate. It usually has a thickness of $2\,\mu$m as this is enough to prevent leakage [18]. Waveguides are etched in the 220 nm thick device layer. Etching all the way through the Si to the SiO_2 provides a very high horizontal index contrast, air - silicon - air. By its nature, the SOI stack has from itself a very high vertical index contrast. A cross section of a waveguide is shown in Figure 1.9. As a result, the mode travelling in the waveguide is highly confined to the core with small exponential tails in the cladding layers. Waveguide bends can be sharp as there are more propagation angles allowed than in systems with a lower index contrast (Figure 1.10). Bend radii of just a few μm are no exception. Another advantage of the high index contrast is that, due to the high confinement, any non-linear or active process in the waveguide is enhanced. These structures can therefore be made smaller than in a lower index contrast waveguide.

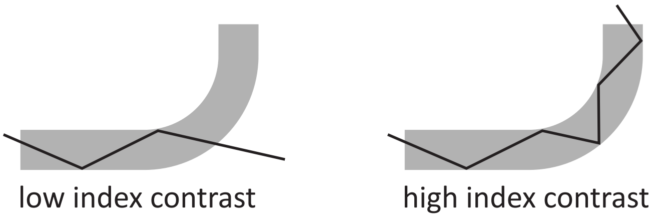

Figure 1.10: In a high index contrast waveguide, bends can be sharper as more propagation angles are allowed.

1.2.1.2 CMOS compatibility

SOI was originally introduced in electronics to improve the performance of transistors. It isolated the transistors from the main Si substrate, reducing the electrical current leakage that degrades the performance. Now it is also one of the driving forces behind photonics and the fabrication processes and know-how built up in CMOS technology are of extraordinary value to silicon photonics. Photonic components in SOI can be produced on wafer-scale in CMOS fabs using deep UV lithography [15]. A photomask containing the patterns to be printed in the silicon, is illuminated and the image is transferred to a photoresist covering the SOI wafer. A dry etching step then etches the image into the silicon. The mass production techniques render the individual components extremely cheap. Examples of research centers using CMOS fabrication processes for silicon photonics are imec in Leuven, Belgium, LETI in Grenoble, France and MIT in Massachusetts, USA.

1.2.1.3 Technology platform

Silicon photonics has to be interpreted in a wider sense than purely SOI wafer-scale produced waveguide structures. It serves as a base layer for a wide range of components and applications. We have already mentioned the photodetectors [16] with germanium grown on or bonded to SOI, but there are many more examples like lasers [19, 20], bio-photonics [21, 22], gas sensors [23, 24] or particle sensors [25].

1.2.2 Integrated optical filter structures

There are many types of optical filters integrated on silicon. Because of the relevance to this thesis, we only discuss filters based on interference and built up out of single mode waveguides. Examples of filters are arrayed waveguide gratings (AWG), Mach-Zehnder interferometers (MZI), ring resonators, Fabry-Perot resonators. A distinction can be made between resonant and non-resonant filters. In the first type, light interferes with itself or in other words, there is a feedback path. These filters boast a high stopband extinction and a narrow passband. Examples are ring or disk resonators and Fabry-Perot resonators. Nonresonant filters combine two or more light paths and there is no feedback present. They generally have a wide passband but a low extinction ratio. A Mach-Zehnder interferometer is an example of this type. Of course exotic combinations of basic filters are possible. In the rest of this work, we focus on ring resonators. They are simple yet very efficient filter structures able to filter out a narrow wavelength band from a broad spectrum.

1.2.2.1 Ring resonators

Optical ring resonators are small filter structures consisting of a waveguide closed in a ring configuration. This ring can be accessed by bus waveguides coupling to and from the ring. These structures are well known and described in literature [26, 27]. The light going around in the ring can interact with itself. When after one round trip the phase of the light has shifted an integer times 2π the light interferes constructively with itself and the cavity is said to be in resonance.

$$k n_{eff} L = q 2\pi, \tag{1.21}$$

with $k = 2\pi/\lambda$, n_{eff} the refractive index of the light mode, L the round trip length and q an integer. From this the resonances follow.

$$\lambda_{res} = \frac{n_{eff} L}{q}, q = 1, 2, 3, ... \tag{1.22}$$

We can distinguish between two comfigurations: the notch filters and the add-drop filters.

Notch filters. Notch filters or all-pass resonators consist of a ring waveguide coupled to one bus waveguide. To analyse the exchange of optical power between the bus and the ring, we consider the situation shown in Figure 1.11. There is lossless coupling from the bus waveguide to the ring and back. The normalized field amplitudes a_1, a_2 and b_1, b_2 are related through the matrix equation [26]:

$$\begin{bmatrix} b_1 \\ b_2 \end{bmatrix} = \begin{bmatrix} t & k \\ -k^* & t^* \end{bmatrix} \begin{bmatrix} a_1 \\ a_2 \end{bmatrix}, \tag{1.23}$$

where t and k are the transmission and coupling coefficient of the electric field amplitudes.

$$|k|^2 + |t|^2 = 1, \tag{1.24}$$

for lossless coupling. The transmission around the ring is

$$a_2 = A e^{-j\phi} b_2, \tag{1.25}$$

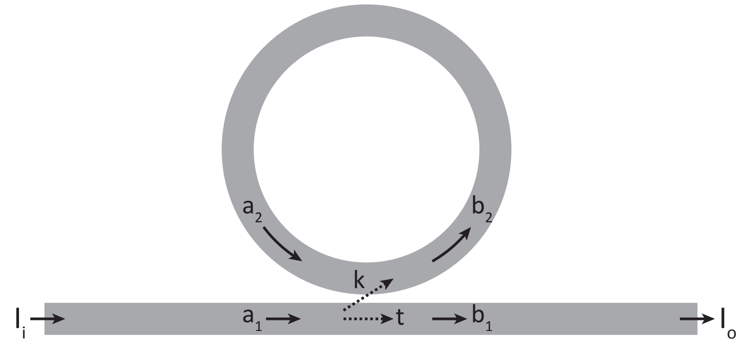

Figure 1.11: Schematic top view of a notch or all-pass ring resonator.

where A is the amplitude transmission after one roundtrip through the ring. It is related to the power attenuation coefficient as:

$$A^2 = e^{-\alpha L}, \tag{1.26}$$

where L is the roundtrip length. Typical losses in our SOI waveguides are of the order of 2 dB/cm. The phase-shift after one round trip is $\phi = \beta L = \frac{2\pi}{\lambda} n_{eff} L$. The transmission can be calculated as:

$$T = \frac{I_o}{I_i} = \frac{A^2 - 2A|t|cos\phi + |t|^2}{1 - 2A|t|cos\phi + (A|t|)^2} \tag{1.27}$$

When the power losses in the ring equal the power coupling to the bus waveguide (1 - A^2 = k^2, or t = A), the transmission drops to zero at a resonance ($\phi = q2\pi$, q and integer). This is called *critical coupling*.

Add-drop filters. The ring is now coupled to two waveguides and the light can be coupled to the drop port as well (Figure 1.12). The matrix equations now become [27]:

$$\begin{bmatrix} b_1 \\ b_2 \end{bmatrix} = \begin{bmatrix} t_1 & k_1 \\ -k_1^* & t_1^* \end{bmatrix} \begin{bmatrix} a_1 \\ a_2 \end{bmatrix} \tag{1.28}$$

$$\begin{bmatrix} b_3 \\ b_4 \end{bmatrix} = \begin{bmatrix} t_2 & k_2 \\ -k_2^* & t_2^* \end{bmatrix} \begin{bmatrix} a_3 \\ a_4 \end{bmatrix}. \tag{1.29}$$

The transmissions follow

$$T_{pass} = \frac{I_{pass}}{I_i} = \frac{|t_2|^2 A^2 - 2A|t_1||t_2|cos\phi + |t_1|^2}{1 - 2A|t_1||t_2|cos\phi + (A|t_1||t_2|)^2} \tag{1.30}$$

$$T_{drop} = \frac{I_{drop}}{I_i} = \frac{(1-|t_1|^2)(1-|t_2|^2)A}{1 - 2A|t_1||t_2|cos\phi + (A|t_1||t_2|)^2} \tag{1.31}$$

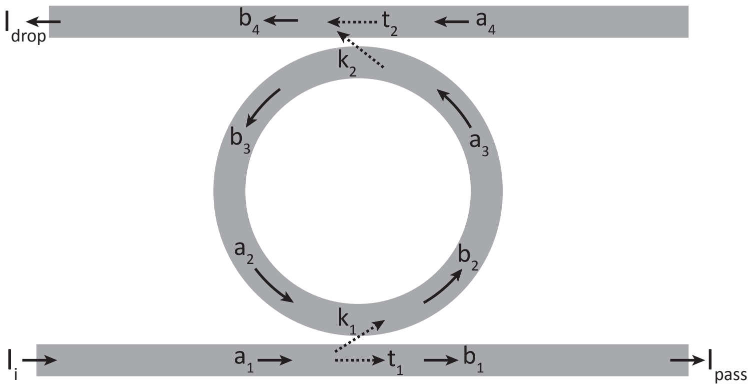

Figure 1.12: Schematic top view of a add-drop ring resonator.

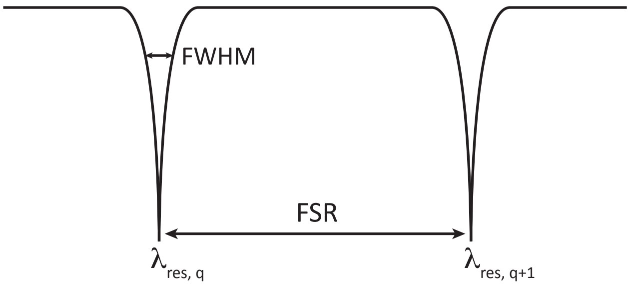

Figure 1.13: Typical pass transmission of a ring resonator. The free spectral range (FSR) is the distance between two resonances. The full bandwidth at half maximum (FWHM) is the 3dB bandwidth of the filter.

Critical coupling now occurs when $A \approx 1$ and $|k_1| = |k_2|$. When the resonator is lossy ($A < 1$), $A|t_2| = |t_1|$ has to hold for critical coupling.

1.2.2.2 Ring resonator spectral properties

Free spectral range. The FSR (Figure 1.13) or the distance between two resonances is given by

$$\Delta\lambda_{FSR} = \frac{\lambda^2}{n_g L}, \tag{1.32}$$

with n_g the group index, defined as

$$n_g = n_{eff} - \lambda \frac{dn_{eff}}{d\lambda} \tag{1.33}$$

FWHM. The full bandwidth at half maximum (Figure 1.13) or the 3 dB bandwidth is given by

$$\Delta\lambda_{FWHM} = \frac{\lambda^2(1-t^2A)}{t\sqrt{A}\pi L n_g} \tag{1.34}$$

Q-factor. The quality factor or Q-factor is defined as the ratio of the resonance wavelength and the FWHM.

$$Q = \frac{t\sqrt{A}\pi L n_g}{\lambda(1-t^2A)} \tag{1.35}$$

It is an important measure of the losses associated with a ring resonator. The higher the Q-factor, the lower the losses. From this formula, it can be seen that a larger ring has a higher Q-factor.

1.3 Conclusions

In this chapter we have discussed the building blocks for this work: liquid crystals and silicon-on-insulator. First we have introduced LC and discussed its various properties related to its anisotropy. Second, the SOI material system was introduced. It is a high index contrast system, ideal for the fabrication of small waveguide structures. We have also devoted part of this chapter to the basics of ring resonators, the wavelength filters that are used throughout this work. In the next chapter we will discuss among others the combination of SOI waveguides and liquid crystals.

References

[1] B. Zhu, T. F. Taunay, M. Fishteyn, X. Liu, S. Chandrasekhar, M. F. Yan, J. M. Fini, E. M. Monberg, and F. V. Dimarcello. *112-Tb/s Space-division multiplexed DWDM transmission with 14-b/s/Hz aggregate spectral efficiency over a 76.8-km seven-core fiber.* Optics Express, 19:16665–16671, 2011.

[2] V. Chigrinov. *Liquid crystal devices: physics and applications.* Artech House, Boston, 1999.

[3] B. E. A. Saleh and M. C. Teich. *Fundamentals of Photonics.* John Wiley & sons, 1991.

[4] Chandrasekhar. *Liquid crystals, 2nd edition.* Cambridge University press, 1992.

[5] J. L. Janning. *Thin-film surface orientation for liquid-crystals.* Applied Physics Letters, 21:173, 1972.

[6] L. A. Goodman, J. T. McGinn, C. H. Anderson, and F. Digeronimo. *Topography of obliquely evaporated silicon-oxide films and its effect on liquid-crystal orientation.* Applied Physics Letters, 21:173, 1972.

[7] W. R. Heffner, D. W. Berreman, M. Sammon, and S. Meiboom. *Liquid-crystal alignment on surfactant treated obliquely evaporated surfaces.* Applied Physics Letters, 36:144–146, 1972.

[8] E. Oton, S. Lopez-Andrez, C. Carrasco-Vela, B. Cerrolaza, N. Bennis, and J. M. Oton. *Dynamics and Electrooptics of Vertically Aligned Nematics With Induced Pretilt on SiO(x).* Journal of Display Technology, 6:263–268, 2010.

[9] V. G. Chigrinov, V. M. Kozenkov, and H. S. Kwok. *Photoalignment of liquid crystalline materials.* Wiley SID series in display technologies, 2008.

[10] I. C. Khoo. *Liquid-Crystals: Physical Properties and Nonlinear Optical Phenomena.* Wiley Hoboken, 1994.

[11] Z. Li, S. Wu, S. Brugioni, R. Meucci, and S. Faetti. *Infrared refractive indices of liquid crystals.* Journal of Applied Physics, 97:073501, 2005.

[12] Z. Li, C. Wen, S. Gauza, R. Lu, and S. Wu. *Refractive Indices of Liquid Crystals for Display Applications.* Journal of Display Technology, 1:51–61, 2005.

[13] J. Li, S. Gauza, and S. T. Wu. *High temperature-gradient refractive index liquid crystals.* Optics Express, 12:2002–2010, 2004.

[14] P. Dumon, W. Bogaerts, V. Wiaux, J. Wouters, S. Beckx, J. Van Campenhout, D. Taillaert, B. Luyssaert, P. Bienstman, D. Van Thourhout, and R. Baets. *Low-loss SOI photonic wires and ring resonators fabricated with deep UV lithography.* Photonics Technology Letters, 16:1328–1330, 2004.

[15] S. K. Selvaraja, P. Jaenen, W. Bogaerts, D. Van Thourhout, P. Dumon, and R. Baets. *Fabrication of Photonic Wire and Crystal Circuits in Silicon-on-Insulator Using 193-nm Optical Lithography.* Journal of Lightwave Technology, 27:4076–4083, 2009.

[16] L. Chen and M. Lipson. *Ultra-low capacitance and high speed germanium photodetectors on silicon.* Optics Express, 17(10):7901–7906, 2009.

[17] A. Liu, L. Liao, D. Rubin, H. Nguyen, B. Ciftcioglu, Y. Chetrit, N. Izhaky, and M. Paniccia. *High-speed optical modulation based on carrier depletion in a silicon waveguide.* Optics Express, 15:660–668, 2007.

[18] P. Dumon. *Ultra-Compact Integrated Optical Filters in Silicon-On-Isolator by Means of Wafer-Scale Technology.* PhD. Thesis, 2007.

[19] G. Roelkens, D. Van Thourhout, R. Baets, R. Notzel, and M. Smit. *Laser emission and photodetection in an InP/InGaAsP layer integrated on and coupled to a Silicon-on-Insulator waveguide circuit.* Optics Express, 14:8154–8159, 2006.

[20] A. W. Fang, H. Park, O. Cohen, R. Jones, M. J. Paniccia, and J. E. Bowers. *Electrically pumped hybrid AlGaInAs-silicon evanescent laser.* Optics Express, 14:9203–9210, 2006.

[21] E. Chow, A. Grot, L. W. Mirkarimi, M. Sigalas, and G. Girolami. *Ultracompact biochemical sensor built with two-dimensional photonic crystal microcavity.* Optics Letters, 29:1093–1095, 2004.

[22] K. De Vos, I. Bartolozzi, E. Schacht, P. Bienstman, and R. Baets. *Silicon-on-Insulator microring resonator for sensitive and label-free biosensing.* Optics Express, 15:7610–7615, 2007.

[23] J. T. Robinson, L. Chen, and M. Lipson. *On-chip gas detection in silicon optical microcavities.* Optics Express, 16:4296–4301, 2008.

[24] N. A. Yebo, P. Lommens, Z. Hens, and R. Baets. *An integrated optic ethanol vapor sensor based on a silicon-on-insulator microring resonator coated with a porous ZnO film.* Optics Express, 18:11859–11866, 2010.

[25] B. Schmidt, V. Almeida, C. Manolatou, S. Preble, and M. Lipson. *Nanocavity in a silicon waveguide for ultrasensitive nanoparticle detection.* Applied Physics Letters, 85:4854–4856, 2004.

[26] A. Yariv. *Universal relations for coupling of optical power between microresonators and dielectric waveguides.* Electronics Letters, 36:321–322, 2000.

[27] J. K. S. Poon, J. Scheuer, S. Mookherjea, G. T. Paloczi, Y. Y. Huang, and A. Yariv. *Matrix analysis of microring coupled-resonator optical waveguides.* Optics Express, 12:90–103, 2004.

2

Waveguiding and Liquid Crystals

2.1 Introduction

In this chapter we will discuss waveguides which involve liquid crystals in some way. The basic principles and material properties introduced in chapter 1 will prove to be useful for the understanding of the waveguide concepts introduced here. The chapter is divided into two main sections. The first explores waveguides where the bulk of the waveguide mode travels in liquid crystalline materials. This part is based mostly on literature. The second part discusses waveguides where part of the cladding consists of liquid crystals. In this section, the foundations for the rest of this thesis are laid. After having read this section, we should have a clear idea of the changeable properties of LC clad waveguides and what has (not) been studied in the past.

2.2 Liquid crystal as the waveguide

Liquid crystals are hugely anisotropic and for this reason a number of waveguides composed of LC have been proposed. The switchable optical properties make them particularly attractive. We make a distinction between waveguides where the light is confined in a pre-defined structure and waveguides formed by the light itself (solitons).

2.2.1 Waveguides with a LC core

Liquid crystals as waveguides in the optical communication framework have been under study for decades [1–3]. For a long time, the consensus seemed to be that liquid crystals would not play a major role in integrated optics but that they are worth investigating for special applications [4]. Scattering losses were estimated too high to yield useful waveguides. These measurements were mostly done in the visible range of the spectrum, more specifically at 633 nm. Later it was shown that scatter losses decrease at longer wavelengths in the near infrared [5]. The last years, literature about LC for (switchable) waveguiding keeps appearing regularly. We have seen e.g. etched V-grooves in Si, overgrown by SiO_2, filled with LC [6, 7] and hollow waveguides with a SiO_2 cladding, infiltrated with LC [8]. Another clever example is the use of LC droplets as electrically tunable micro resonators [9].

Not only waveguides on a chip can be equipped with a liquid crystal core. In literature, quite a few publications discussing optical fibers with an LC core can be found [10–12]. The interaction of the light with the LC is very strong in these devices and they are attractive for a.o. polarization effects, light modulation and sensing.

2.2.2 Spatial solitons

Another area of waveguiding with liquid crystals is that of solitons. Solitons in LC are based on the nonlinearities of the material. In LC one can find many non-linearities that do not exist in other materials. In literature, nice overviews can be found. Examples are director reorientation by laser light, thermal nonlinearities, density nonlinearities, order parameter fluctuations,... [13–15]. Consider a normal optical beam of finite size. After propagation, it will have spread out due to diffraction which acts as a concave lens. The diffraction can be countered when the material in the center of the beam has a higher refractive index. This higher refractive index can be induced by nonlinear effects and acts as a convex lens to narrow the beam. In the occasion that the two effects are exactly in balance, the phase front of the wave will remain the same during propagation. A soliton is created! It creates its own waveguide in a material and travels unchanged. Often, a distinction is made between (1+1)D and (2+1)D solitons. The first number represents the directions a beam can diffract in while the second is associated with the propagation direction. A (1+1)D soliton is a soliton generated in a waveguide geometry. It can diffract in only one direction, the other is limited by the waveguide structure. A (2+1)D soliton travels in the bulk of the LC. In bulk nematic LC, these solitons are sometimes called nematicons.

Thermally induced solitons are based on heating of the material.The ordinary refractive index of the LC increases with themperature and by absorbing the light, the LC heats locally. Thus, a region of higher refractive index is created. Often absorbing dyes are used to allow solitons with low powers [16, 17]. Light itself can also induce a transition to the isotropic phase and travels inside this isotropic channel [18].

When strong enough, the electric field of a beam of light can reorient the LC director. This principle is similar to the reorientation caused by an external electric field (see chapter 1). When it is focused in a liquid crystal, however, the reorientation of the director induces a locally increased refractive index which spreads out due to the elastic forces between the molecules. The light remains confined to this region of high refractive index [19–22].

2.3 Liquid crystal as (part of) the cladding

For many applications in a.o. sensing and optical communications light is confined in well-defined waveguides. Silicon-on-insulator as introduced in chapter 1 is an example of a material system suited for waveguiding. It can be useful to use liquid crystals as a part of the cladding as their optical properties are easily influenced by temperature or an electric field (or another effect). In the rest of this section we discuss slab waveguides with a cladding of LC, single mode strip waveguides with a cladding of LC and briefly photonic crystals and photonic crystal fibers infiltrated with LC.

2.3.1 Slab waveguides

A slab waveguide is simply a layer stack that is capable of confining the light by having a higher refractive index than the surrounding material. Depending on the thickness of the layer with the highest refractive index, the slab guides one or more modes (TE or TM). The modes have an effective refractive index that depends on the refractive indices of the layers and their thickness. When the layers lay in the xz-plane, the light is confined in the y-direction. We assume light propagation along the z-axis. In the xz-plane there is no confinement and the modes will spread out while propagating.

When LC is applied as the top layer of the slab waveguide (Figure 2.1), the modes' properties are influenced as they have exponential tails extending into the cladding. How big this influence is, depends on the index contrast between the cladding and the core. If this contrast is high, the light will be strongly confined in the core and interaction with the cladding will be small. However, if the indices of the LC and the core are similar, then the mode extends far into the LC and the interaction will be considerable. There are already some components available based on slab waveguides with a top layer of LC. Electrical reorientation of the cladding layer can induce a large difference in the optical path of the TE

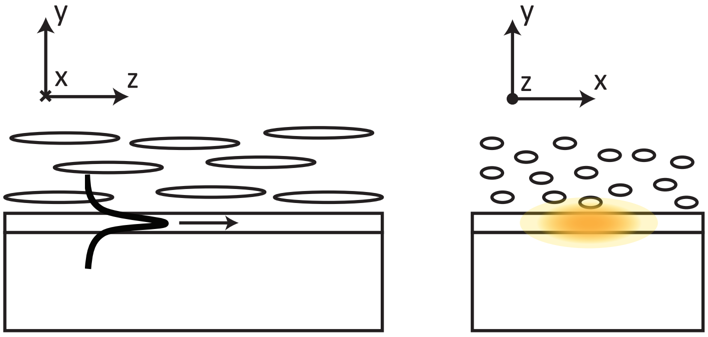

Figure 2.1: Schematic view of a slab waveguide clad with a layer of LC. Note that the light in the slab will diffract while propagating.

and the TM mode. This can be used in broadband Fourier spectroscopy for IR detection of molecules [23]. When the applied voltage varies along the x-axis, the phase becomes a function of the x-coordinate and functions like beam steering and (de-)focusing of the beam can be implemented [24]. Another application is switchable coupling between two slab waveguides. The coupling length is dependent on the distance between the two slabs and the refractive index of the materials between the slabs. When there is LC between the two slabs, the coupling length can be influenced by an electric field. This can be used to switch the light from one waveguide to another or leave it in the first waveguide [25, 26].

2.3.2 Strip waveguides

In slab waveguides, the light is confined in one direction (along the y-axis) only. Etching the core waveguiding layer allows us to confine the light in the xz-plane as well. Let's consider for the rest of this part waveguides formed by strips of a high index contrast running along the z-axis. The light is now confined both in the x- and y-direction and can propagate in the z-direction. When the refractive index contrast is high, as is the case in SOI, the waveguides have dimensions of the order of a few hundred nm. A downside of the use of this high index contrast is that the waveguide modes are more strongly confined than would be the case in a system with a low index contrast. When the alignment of the director to the material is planar, it has been shown that the director aligns itself to the ribs of intersecting surfaces [27]. The orientation of the director in the cladding layer can be influenced with an externally applied electric field. This will have an effect on the effective index of the modes traveling in the waveguide. In Figure 2.3 and

Figure 2.4, the director is oriented along the x, y or z-axis.

Let's first consider the TE ground mode of a SOI waveguide. Due to the strong index contrast and the small dimensions of the waveguide, it follows from Maxwell's equations that, apart from the transversal x-component, the mode has also a large longitudinal z-component, located at the sidewalls of the waveguide (see Figure 2.2, where we have plotted the electric field components of the TE and TM mode in a SOI waveguide). Both the x and the z-component have considerable exponential tails extending into the cladding and they both have an influence on the effective index of the mode. The tails of the x-component extend from the top of the waveguide, while the tails of the z-component sit at the sidewalls. The x-component is the largest and when the director is oriented along the x-axis, n_{eff} is largest. When the director is along the y-axis, both the x and the z-component experience a low dielectric constant and the effective index will be small. For alignment in the z-direction, n_{eff} takes on an intermediate value.

The fundamental TM mode is polarized mainly along the y-axis. This implies a high effective index for a director orientation along the y-axis. n_{eff} takes a lower value for any other orientation of the LC director. However, as there is again a z-component to the TM mode, the n_{eff} is lowest for an orientation of the director along the x-axis. In Figure 2.3 and Figure 2.4 we show the values of n_{eff} of the fundamental TE and TM mode respectively. We have calculated the theoretical resonance wavelength of a ring resonator guiding these modes. We assumed a resonance at 1550 nm for rings with the director aligned along the waveguides. The differences in resonance wavelength, or the tuning range, are a lot bigger for the TM than for the TE mode. This is directly related to the confinement of the light to the core of the waveguide. The TE mode is strongly confined to the core, 65% of the optical power is located in the core material, the remaining 35% can be found in the cladding layers. The TM mode is far less confined as only 37% of the optical power sits inside the core region. 63% of the optical power is found in the cladding layers. This is why ring resonators guiding the TM mode are expected to have a larger tuning range than their TE counterparts. This way of tuning n_{eff} has inspired many groups to investigate tunable waveguide devices based on strip waveguides with a LC cladding. Tunable Fabry-Perot resonators (a.o.) have been demonstrated [28]. The resonances of a SOI waveguide between two facets in the silicon were tuned over 0.3 nm with an applied voltage of 10 V. There has also been a considerable effort towards tunable ring resonators with LC cladding, the topic of this dissertation. It is clear that the LC cladding offers possibilities for a very wide tuning range, especially for ring resonators guiding TM polarized light. In 2003 already, a tunable TE ring resonator with LC cladding was shown [29]. The tuning range, however, remained limited to 0.22 nm. A method using a photo-alignment layer on the ring resonators was patented by

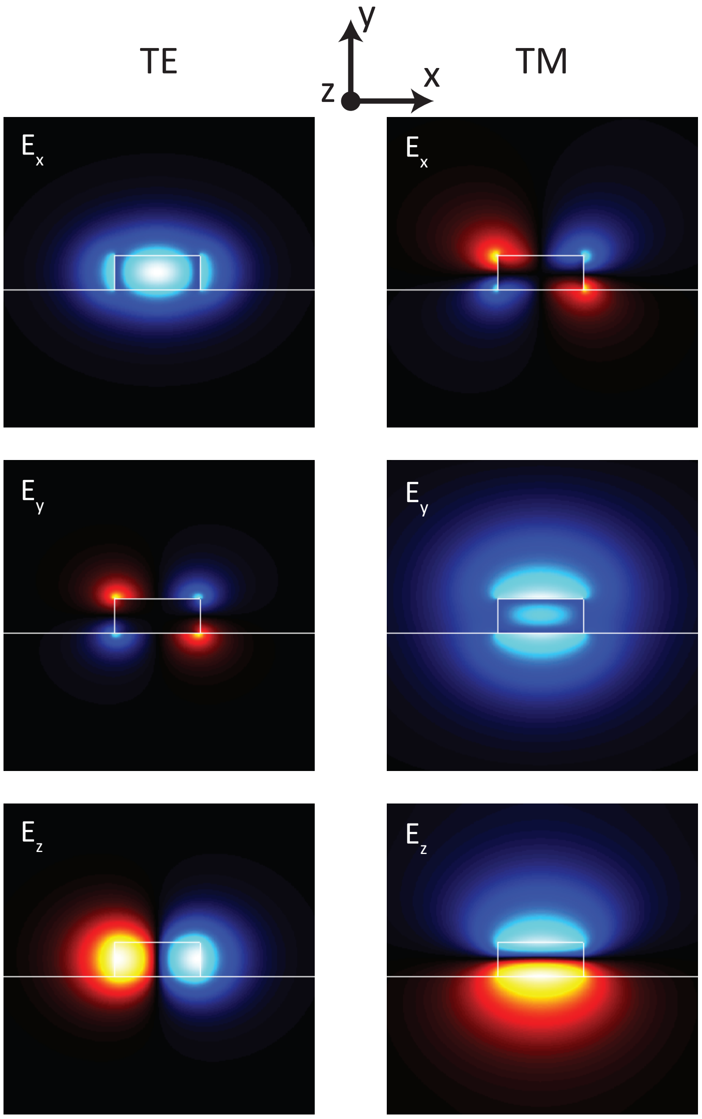

Figure 2.2: X, y and z components of the electric field of the TE mode (left) and the TM mode (right).

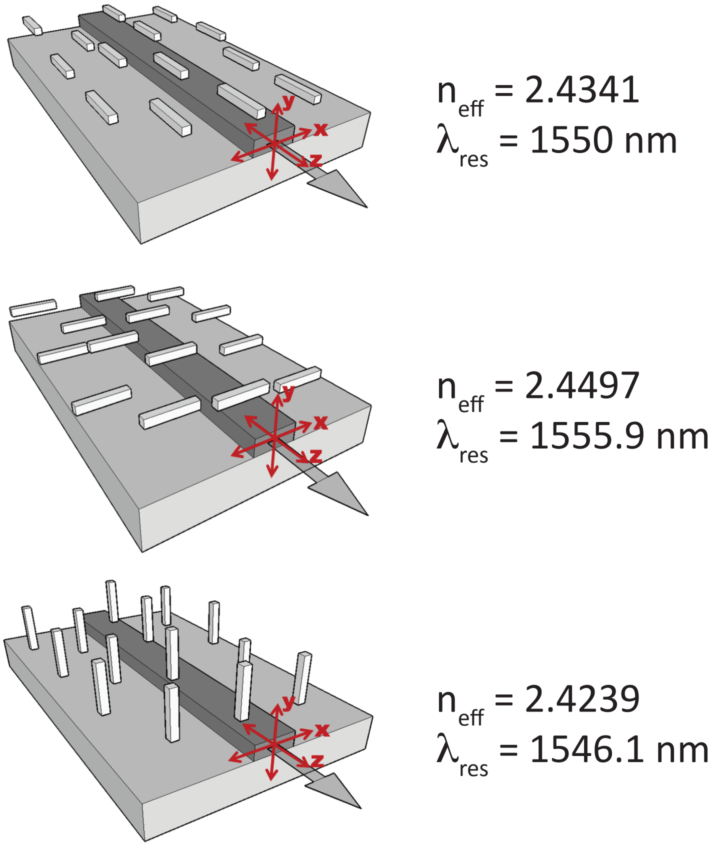

Figure 2.3: The effective index of the TE mode in a waveguide with LC top cladding changes, depending on the orientation of the LC molecules. The resonance wavelengths of a ring resonator guiding TE light are also indicated, assuming a resonance at 1550 nm when the director lies along the z-axis.

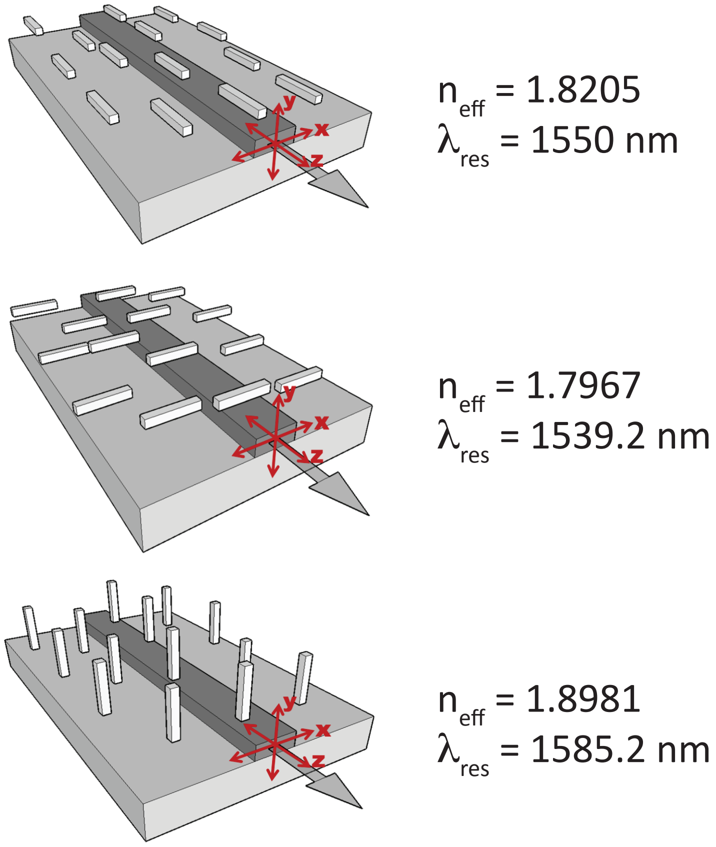

Figure 2.4: The effective index of the TM mode in a waveguide with LC top cladding changes, depending on the orientation of the LC molecules. The resonance wavelengths of a ring resonator guiding TM light are also indicated, assuming a resonance at 1550 nm when the director lies along the z-axis.

Chigrinov et al [30]. This is more or less the situation before the results presented in this dissertation were achieved.

2.3.3 Liquid crystal-inflitrated photonic crystals and photonic crystal fibers

A combination of LCs and silicon photonics that deserves a place here is photonic crystals infiltrated by LCs. The holes of the photonic crystal offer easy access for liquid crystals to the core of the waveguide. This way, the waveguides can benefit of the extreme material properties of LC. Thermal tuning of silicon photonic crystals was shown early this century [31]. Later, other tunable PCs have been demonstrated, such as electrically tunable PC lasers [32].

Photonic crystal fibers (PCF) are a special and relatively recent class of optical fibers [33]. They are microstructures and the light is confined either through a photonic bandgap (PBG) effect or by total internal reflection. The material they are made from is mostly SiO_2, with a series of holes around the core. The light in the PCF is highly sensitive to materials present inside the holes. Very different and unique applications of PCFs have been shown, e.g. non-linear fibers with high dispersion control [34], supercontinuum generation [35], hollow-core fibers [36] and many more. PCFs can be infiltrated by LCs in order to increase the functionality. Among others thermooptic fiber switches [37] and continuously tunable birefringence have been shown some time ago. New applications in this rapidly evolving field are to be expected [38].

2.4 Conclusions

In this chapter we have given a short overview of Liquid Crystals used in a combination with photonic waveguides. We have discussed waveguides where the core material is LC and waveguides where only a part of the cladding contains LC. All these combinations make use of the exceptional material properties of LC to add functionality to photonic waveguides. In this chapter, we have also explained the basic principle of tuning the effective refractive index of modes in SOI waveguides with a LC cladding. This intuitively simple idea will form the base of the coming chapters.

References

[1] T. G. Giallorenzi, J. A. Weiss, and J. P. Sheridan. *Light scattering from smectic liquid-crystal waveguides.* Journal of Applied Physics, 47:1820–1826, 1976.

[2] D. J Channin. *Optical waveguide modulation using nematic liquid crystal.* Applied Physics Letters, 22:365–366, 1973.

[3] C. Hu and J. R. Whinnery. *Losses of a nematic Liquid-crystal optical waveguide.* Journal of the Optical Society of America, 64:1424–1432, 1974.

[4] J. R. Whinnery, C. Hu, and Y. S. Kwon. *Liquid-crystal waveguides for Integrated Optics.* IEEE Journal of Quantum Electronics, 13:262–267, 1977.

[5] M. Kawachi, N. Shibita, and T. Edahiro. *Possibility of use of liquid crystals as optical waveguide material for 1.3μm and 1.55μm bands.* Japanese Journal of Applied Physics, 21:162–164, 1982.

[6] A. d'Alessandro, B. Bellini, D. Donisi, R. Beccherelli, and R. Asquini. *Nematic liquid crystal optical channel waveguides on silicon.* IEEE Journal of Quantum Electronics, 42:1084–1090, 2006.

[7] D. Donisi, B. Bellini, R. Beccherelli, R. Asquini, G. Gilardi, M. Trotta, and A. d'Alessandro. *A Switchable Liquid-Crystal Optical Channel Waveguide on Silicon.* IEEE Journal of Quantum Electronics, 46:762–768, 2010.

[8] D. P. Cai, S. C. Nien, H. K. Chiu, C. C. Chen, and C. C. Lee. *Electrically tunable liquid crystal waveguide attenuators.* Optics Express, 19:11890–11896, 2011.

[9] M. Humar, M. Ravnik, S. Pajk, and I. Musevic. *Electrically tunable liquid crystal optical microresonators.* Nature Photonics, 3:595–600, 2009.

[10] T.R. Wolinski, A. Szymanska, T. Nasilowski, M.A. Karpierz, A. Kujawski, and R. Dabrowski. *Propagation effects in liquid crystal-core optical fiber waveguides.* Molecular Crystals and Liquid Crystals, 321:113–124, 1998.

[11] T.R. Wolinski, A. Szymanska, E. Nasilowski, Nowinowski, and R. Dabrowski. *Polarization Properties of Liquid Crystal-Core Optical Fiber Waveguides.* Molecular Crystals and Liquid Crystals, 352:361–370, 2000.

[12] T.R. Wolinski and A. Szymanska. *Polarimetric optical fibers with elliptical liquid crystal core.* Measurement Science and Technology, 12:948–951, 2001.

[13] I. C. Khoo. *Liquid-Crystals: Physical Properties and Nonlinear Optical Phenomena.* Wiley Hoboken, 1994.

[14] I. C. Khoo. *Nonlinear optics of liquid crystalline materials.* Physics Reports, 471:221–267, 2009.

[15] F. Simoni. *Nonlinear Optical Properties of liquid-crystals and Polymer Dispersed Liquid-Crystals.* World Sci., 1997.

[16] F. Derrien, J. Henninot, M. Warenghem, and G. Abbate. *A Thermal (2D+1) Spatial Optical Soliton in a Dye Doped Liquid Crystal.* Journal of Optics A: Pure and Applied Optics, 2:332–337, 2000.

[17] J. Henninot, M. Debailleul, and M. Warenghem. *Tunable non-locality of Thermal Non-linearity in Dye Doped Nematic Liquid Crystals.* Molecular Crystals and Liquid Crystals, 375:631–640, 2002.

[18] J. Henninot, M. Debailleul, R. Asquini, A. d'Alessandro, and M. Warenghem. *Self-waveguiding in an Isotropic Channel Induced in Dye Doped Nematic Liquid Crystal and a Bent Self-Waveguide.* Journal of Optics A: Pure and Applied Optics, 6:315–323, 2004.

[19] M. A. Karpierz, M. Sierakowski, M. Swillo, and T. Wolinski. *Self-focusing in liquid-crystalline waveguides.* Molecular Crystals and Liquid Crystals, 320:157–163, 1998.

[20] M. Peccianti, A. De Rossi, G. Assanto, A. De Luca, C. Umeton, and I. C. Khoo. *Electrically assisted self-confinement and waveguiding in planar nematic liquid-crystal cells.* Applied Physics Letters, 77:7–9, 2000.

[21] J. Beeckman, K. Neyts, X. Hutsebaut, C. Cambournac, and M. Haelterman. *Simulations and experiments on self-focusing conditions in nematic liquid-crystal planar cells.* Optics Express, 12:1011–1018, 2004.

[22] J. Beeckman, K. Neyts, X. Hutsebaut, and M. Haelterman. *Observation of out-coupling of a nematicon.* Opto-Electronics Review, 14:263–267, 2006.

[23] T. H. Chao, T. T. Lu, S. R. Davis, S. D. Rommel, G. Farca, B. Luey, A. Martin, and M. H. Anderson. *Compact liquid-crystal waveguide based fourier transform spectrometer for in-situ and remote gas and chemical sensing.* Proceedings of the SPIE, page 69770p, 2008.

[24] S. R. Davis, G. Farca, S. D. Rommel, A. W. Martin, and M. H. and Anderson. *Analog, non-mechanical beam-steerer with 80 degree field of regard.* Proceedings of the SPIE, page 69710G, 2008.

[25] M. A. Clark, N. A. Handshy. *Surface-stabilized ferroelectric liquid-crystal electro-optic waveguide switch.* Applied Physics Letters, 57:1852–1854, 1990.

[26] G. N. Ntogari, D. Tsipouridou, and E. Kriezis. *A numerical study of optical switches and modulators based on ferroelectric liquid-crystals.* Journal of Optics A: Pure and Applied Optics, 7:82–87, 2005.

[27] H. Desmet, K. Neyts, and R. Baets. *Modeling nematic liquid crystals in the neigborhood of edges.* Journal of Applied Physics, 98:123517, 2005.

[28] H. Desmet, W. Bogaerts, A. Adamski, J. Beeckman, K. Neyts, and R. Baets. *Silicon-on-insulator optical waveguides with liquid-crystal cladding for switching and tuning.* in Proceedings of the European Conference on Optical Communication, 3:430Ű431, 2003.

[29] B. Maune, R. Lawson, C. Gunn, A. Scherer, and L. Dalton. *Electrically tunable ring resonators incorporating nematic liquid crystals as cladding layers.* Applied Physics Letters, 83:4689–4691, 2003.

[30] V. G. Chigrinov, L. Zhou, A. A. Muravsky, and A. W. Poon. *Electrically tunable microresonators using photoaligned liquid-crystals.* On US Patent 7, 783,144 B2, 2010.

[31] S. W. Leonard, J. P. Mondia, H. M. van Driel, O. Toader, S. John, K. Busch, A. Birner, U. Gosele, and V. Lehmann. *Tunable two-dimensional photonic crystals using liquid-crystal infiltration.* Physical Review B, 61:R2389–R2392, 2000.

[32] B. Maune, M. Loncar, J. Witzens, M. Hochberg, T. Baehr-Jones, D. Psaltis, A. Scherer, and Y. M. Qiu. *Liquid-crystal electric tuning of a photonic crystal laser.* Applied Physics Letters, 85:360–362, 2004.

[33] J. C. Knight, J. Broeng, T. A. Birks, and P. St. J. Russell. *Photonic bandgap guidance in optical fibers.* Science, 283:1476–1478, 1998.

[34] J. C. Knight, J. Arriaga, T. A. Birks, A. Ortigosa-Blanch, W. J. Wadsworth, and P. S. Russell. *Optical devices based on liquid crystal photonic bandgap fibres.* Photonics Technology Letters, 12:807–809, 2000.

[35] J. M. Dudley, G. Genty, and S. Coen. *Supercontinuum generation in photonic crystal fiber.* Reviews of Modern Physics, 78:1135–1184, 2006.

[36] R. F. Cregan, B. J. Mangan, J. C. Knight, T. A. Birks, P. S. Russell, P. J. Roberts, and D. C. Allan. *Single-mode photonic band gap guidance of light in air.* Science, 831:1537–1539, 1999.

[37] T. T. Larsen, A. Bjarklev, D. S. Hermann, and J. Broeng. *Optical devices based on liquid crystal photonic bandgap fibres.* Optics Express, 11:2589–2596, 2003.

[38] T. R. Wolinski, S. Ertman, D. Budaszewski, M. Chychlowski, A. Czapla, R. Dabrowski, A. W. Domanski, P. Mergo, E. Nowinowski-Kruszelnicki, K. A. Rutkowska, M. Sierakowski, and M. Tefelska. *Liquid Crystal Photonic Crystal Fibers and their applications.* in Proceedings of Conference on Emerging Liquid Crystal Technologies VI, 7955:795502, 2011.

3
The Liquid Crystal Cell

3.1 Introduction

The fabrication process of the test cells and the study of the alignment of the liquid crystal throughout the cell are discussed in this chapter. The cell offers the basic functionality of applying an electric field over a liquid crystal layer which is deposited on a silicon-on-insulator chip. This is briefly described in section 3.2. We assemble the cell manually in a clean room environment. This process is explained in section 3.3 together with an overview of the materials used. The alignment of the liquid crystal plays an important role in the final performance of the cell. The experiments concerning the alignment involve work with a polarizing microscope. An introduction to liquid crystal alignment is given in section 3.4 together with an overview of the experiments we performed to determine the alignment in the cells.

3.2 General Implementation

The goal is to incorporate a top cladding layer of LC on top of a SOI chip. We choose a straightforward implementation based on techniques of display technology. The LC layer is sandwiched between the SOI chip and a glass plate. The chip and the glass plate are glued together with glue mixed with spacers. The

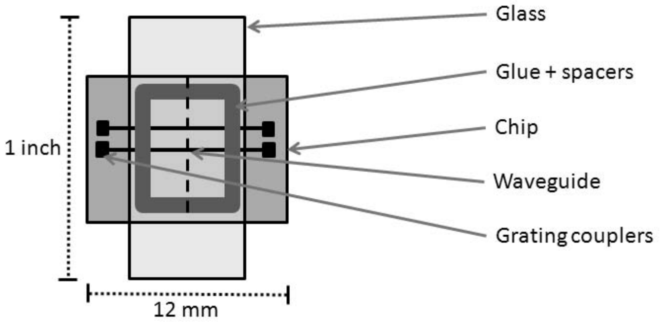

(a)

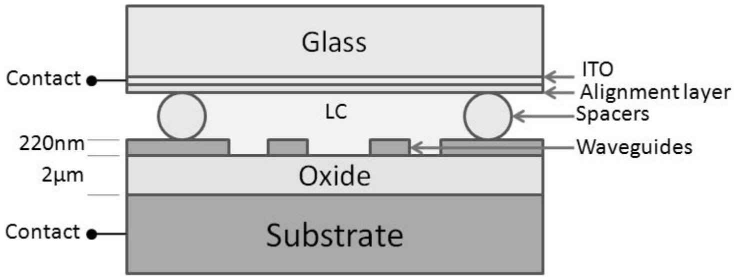

(b)

Figure 3.1: Schematic view of a device consisting of a SOI substrate with LC cladding, sealed off by a glass plate with ITO electrode and alignment layer.(a) top view, (b) side view, cross section is taken along the dashed line in Figure 3.1(a).

spacers will ensure a fixed thickness of the LC layer. The cell needs electrodes if we want to apply an electric field over the LC. These are provided by a transparent conducting layer of indium tin oxide (ITO) present on the glass plate and by the silicon substrate itself. The transparency of the ITO makes it possible to study the properties of the LC layer once the cell is fabricated. Finally, an alignment layer on the glass plate provides a fixed orientation of the liquid crystal director on this surface. A schematic side view of the cell is shown by Figure 3.1(b). The different process steps are described in order of execution in section 3.3. All these steps are done manually and require some practical skills. After an appropriate learning period a yield of over 90 % can easily be achieved.

3.3 Assembly

The assembly of a typical liquid crystal cell as seen in Figure 3.1 is quite straightforward. The processing steps in order of execution are as follows:

1. **Cleaning of the glass plates.** The glass plates are obtained from Delta Technologies [1]. They measure 1 inch by 1 inch and are 1.1 mm thick. On one side they are coated with a thin ITO layer (approx. 100 nm). The cells will be only a few micrometer thin so thorough cleaning of the glass plates is necessary. They are submerged in an ultrasonic bath filled with a soap solution, acetone and isopropanol consecutively for 15 min. each.

2. **Coating with an alignment layer.** To avoid the formation of domains in the LC, it is important to align the liquid crystal properly on the surfaces it touches. The alignment on glass plate can easily be achieved by spincoating an appropriate layer. After spincoating, the layer is cured in an oven. In this work we have used nylon and a polymide. They align LC in a planar fashion and there seems to be no difference in alignment using one or the other material.

3. **Rubbing the alignment layer.** When the alignment layer is rubbed with a cloth, small grooves are formed running in the rubbing direction. The LC which comes into contact with the layer will align itself along these grooves. The cloth is wound around a rotating drum. The glass plates are brought into contact with the revolving cloth. The harder the contact, the stronger the alignment of the LC will be [2].

4. **Cutting the glass plate.** Coupling light in and out of the waveguides on the SOI chip is done by grating couplers [3]. These diffract vertically incoming light into the waveguides. This coupling is explained further in chapter 4. In order to shine light in a controlled fashion on the couplers, they should not be covered by the glass plate. As the grating couplers are spaced only 12 mm apart, the plates are cut to appropriate size using a scriber with a diamond tip.

5. **Glueing the glass plate to the chip.** Norland Optical Adhesive UV curable glue [4] is mixed with spherical spacers. The spacers have a known diameter (typically 6 to 10 μm) and serve to keep the glass plate at a fixed distance when it is glued to the chip. The glue is deposited on the glass plate with help of a dispensing machine controlled by a plotter, after which the cell is assembled manually.

6. **Soldering metallic wires for contacting.** Metallic wires are soldered to the glass plate (in contact with the ITO layer) and to the Si substrate.

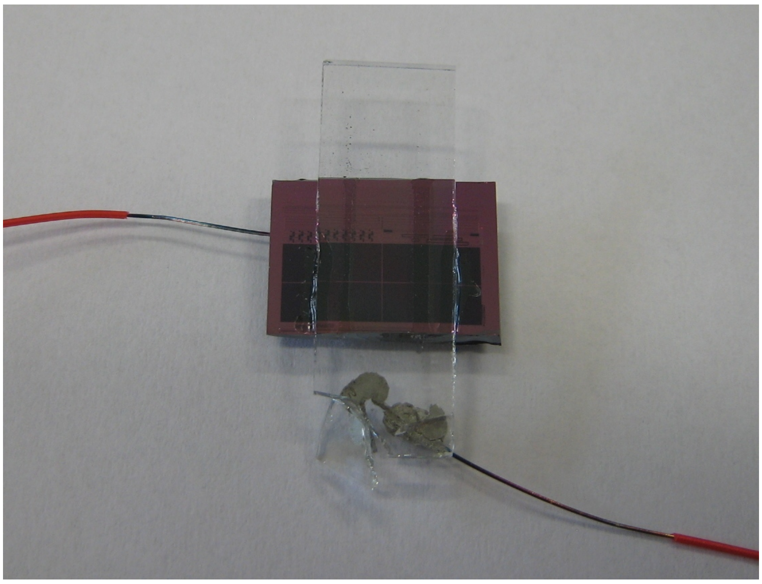

Figure 3.2: Photograph of a completed cell.

7. **Filling the cell.** The cell and the LC are heated above the clearing temperature of the LC. The LC will be in its isotropic phase where it is less viscous. A drop of LC is deposited near the gap between the chip and the glass plate and is sucked inside by capillary forces. The cell is then gradually cooled down to minimize the formation of domains. Finally the cell is sealed with glue.

A photograph of a completed cell can be seen in Figure 3.2

3.4 Alignment

3.4.1 Introduction

Rubbing the alignment layer on the glass plate provides a fixed orientation of the LC director [2]. When a liquid crystal is caught between two such coated glass plates (this is the case in many display applications), the director in the cell will have a uniform orientation. In this work, however, one of the boundaries is an SOI chip. Due to the waveguide structures, this chip has a certain surface geometry which will influence the alignment of the LC on this surface. Furthermore, applying an alignment layer on the chip surface would weaken the influence of the liquid crystal on the waveguide mode due to both its thickness and the anchoring forces that will inhibit the reorientation of the surface director.

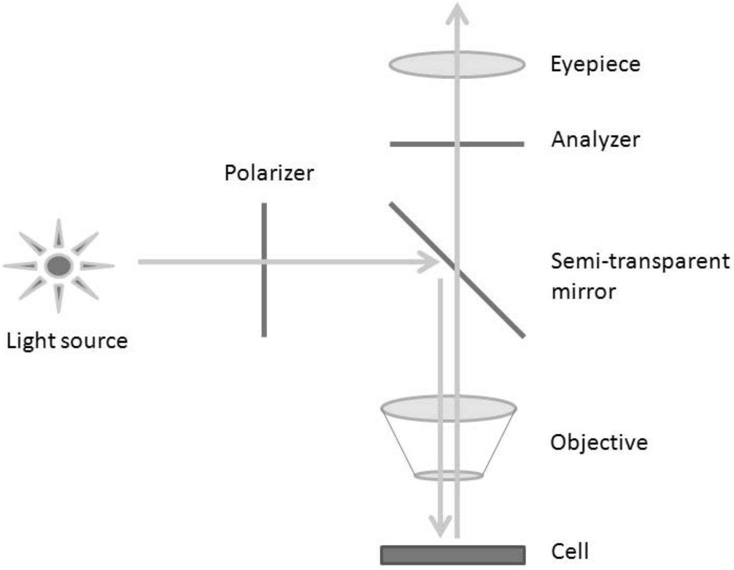

Figure 3.3: General outline of a polarizing microscope in reflection.

A very large degree of freedom of the director on the chip's surface is desirable as it will allow maximal reorientation. This is in practice hard to achieve as the anchoring strength will always have a finite value [5]. On any surface, the molecules will experience some anchoring forces even when no alignment layer is present. On the rubbed surface of the glass plate the anchoring is very strong and the orientation is determined by the direction of the rubbing. On the chip surface it is less clear what exactly happens. The director will orient itself in such a manner as to minimize the energy stored in the LC layer [6–9]. Experiments with a polarizing microscope help to gain insight into this.

3.4.2 Polarizing microscopy

In this work we inspected the liquid crystal cells with a polarizing microscope Nikon Eclipse E400 POL. This type of microscope is equipped with two polarizers which can be rotated. One polarizer is rotated 90^o with respect to the other (crossed polarizers). The general layout of the microscope is shown in Figure 3.3. This setup is also often used in the study of liquid crystal displays. Light from the source passes through the polarizer resulting in linearly polarized light. A semi-transparent mirror deflects the light towards the cell under study. The light reflects off the cell and hits the second polarizer, also called the analyzer.

The alignment of the LC on the glass plate (determined by the alignment

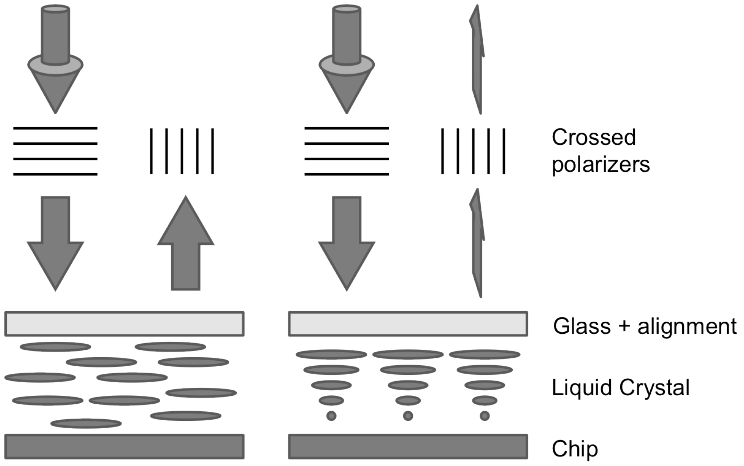

Figure 3.4: Principle of observing a cell with a polarizing microscope.

layer) is chosen to be parallel to the orientation of the polarizer. In a uniform LC layer the polarization of the light remains unchanged upon transmission. All light will be blocked at the analyzer (Figure 3.4 left side). When there is a twist present in the LC layer, the polarization of the light will undergo a change. For some wavelengths, the polarization is rotated 90^o and all the light will be transmitted through the analyzer. If the molecules have a twist over 90^o through the layer, and the light that reflects off the surface experiences a total twist of 180^o, the transmission T can be calculated as

$$T = \frac{sin^2\pi\sqrt{1+\left(\frac{\Delta nd}{\lambda}\right)^2}}{1+\left(\frac{\Delta nd}{\lambda}\right)^2}, \tag{3.1}$$

with Δn the optical anisotropy (n_e-n_o), $d/2$ the thickness of the cell (bear in mind that the light reflects off the chip's surface so the total distance travelled by the light is d) and λ the wavelength of the light. When we observe a 2.5 μm thick cell filled with a LC that has a Δn of 0.2 through crossed polarizers, we get a transmission as in Figure 3.5. The peak of transmission lies around 580 nm and the cell will appear yellow-ish. When the twist is slow (d » λ), the polarization turns gently, following the twist of the director. This is called the Mauguin limit and the transmission from equation 3.1 equals zero in that case. For our cells, there is still transmission of the light indicating that the cells are not thick enough for the Mauguin limit to appear. The yellow-ish color that appears, is due to the spectrum of the microscope light.

When the LC layer is uniform (no twist) but the alignment is not parallel with

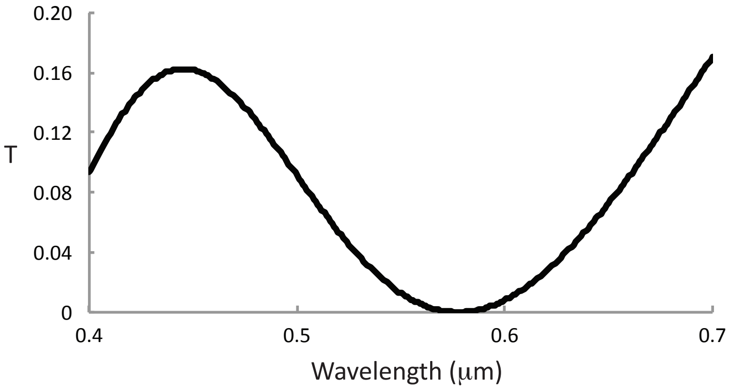

Figure 3.5: Transmission of a twisted cell (as seen in the right side of Figure 3.4) with a thickness of 5 μm (2 x 2.5 μm) and a Δn of 0.2.

the polarizer's orientation, there is also transmission of light. The linear polarization hitting the liquid crystal splits up into two linear components, one along the long axis (n_e) of the molecules and one along the short axis (n_o). Both travel at a different speed and as a result the total polarization changes continuously. When the angle between the rubbing direction and the orientation of the polarizer is ϕ, the transmission can be calculated as

$$T = sin^2\left(2\phi\right) sin^2\left(-\pi\frac{\Delta n d}{\lambda}\right), \tag{3.2}$$

with again Δn the optical anisotropy (n_e-n_o), $d/2$ the thickness of the cell and λ the wavelength of the light. It is clear that the transmission is zero when the rubbing direction is parallel with or perpendicular to the orientation of the polarizer (ϕ = n$\frac{\pi}{2}$, n = 0,1,2,...). A 2.5 μm thick cell with a uniform layer of LC that has a Δn of 0.2 yields a transmission as in Figure 3.6 when the angle between the polarizer and the rubbing direction is $\frac{\pi}{4}$.

3.4.3 Alignment on chip

The observations described in the previous paragraph are quite straightforward. They require, however, a well defined alignment of the LC on the surface of the chip. In this work the situation is much more complicated as the surface is not completely flat due to the etched structures in the silicon. Moreover, we can not use an alignment layer as it will decrease the interaction of the waveguide mode with the LC. So, apart from a thorough cleaning, we leave the surface of the chip as it is and study the behaviour of the LC cladding.

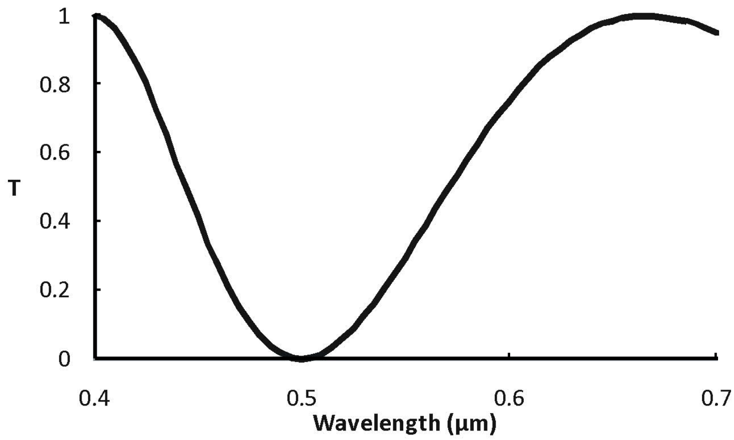

Figure 3.6: Transmission of a uniform cell (as seen in the left side of Figure 3.4) with a thickness of 5μm (2 x 2.5μm) and a Δn of 0.2. The polarizer makes an angle of $\frac{\pi}{4}$ with the rubbing direction

A simple test structure on the chip is used. It consist of a waveguide flanked by several hundreds of Si rectangles. A glass plate covered with a polymide is attached to the chip and the cell is filled with 5CB. The rubbed polymide provides an alignment of the LC parallel to the direction of the waveguide. The image acquired with a polarizing microscope with crossed polarizers remains mostly dark (Figure 3.7). The polarizer is aligned parallel to the preferential direction defined by the alignment layer. The dark regions indicate that the LC retains the same orientation from glass plate to chip surface. Therefore no change in polarization is induced by the LC and transmission is close to zero (eq. 3.2). The bright parallel lines correspond to the gratings next to the waveguide. Here, the LC will twist to align itself parallel to the sidewalls of the Si blocks. A twist from the glass plate to the chip surface is the result and light will be transmitted according to eq. 3.1. The waveguide lies in between these gratings and appears dark in the image. From this, we can draw conclusions regarding the director orientation throughout the cell:

- The molecules remain parallel to the glass plate and chip surface (in the plane).
- The orientation is everywhere determined by the alignment layer on the glass plate except on the surface of the chip, where it aligns parallel to the vertical sidewalls of the structures. A twist throughout the layer is the result.

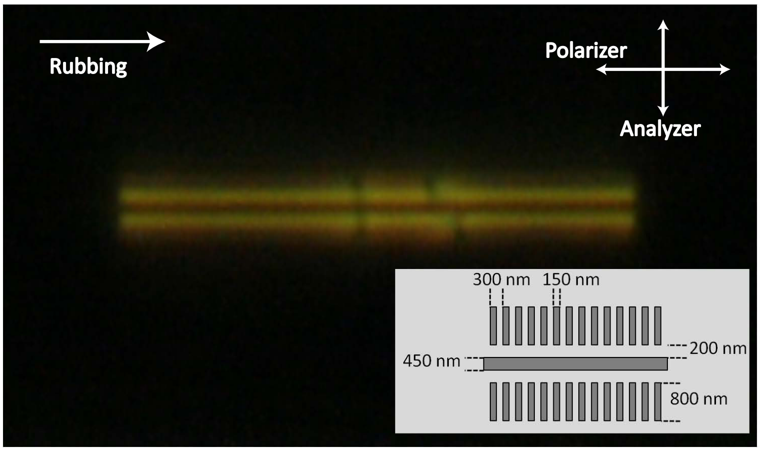

Figure 3.7: Polarizing microscope image of a waveguide and grating covered with LC. The inset shows the structure outline.

- The director is able to follow the silicon structures down to nanometer scale.

In this test structure the director twists over 90^o to align with the sidewalls of the Si blocks in the grating. This twist can be left-handed or right-handed, both are energetically equivalent. The dark interruptions of the bright lines in Figure 3.7 are disclinations. These are separation lines between regions with a different twist handedness. There is no well-defined director near these lines and they always tend to appear dark in polarizing microscope images.

3.5 Conclusions

In this work the liquid crystal cells are fabricated by glueing a glass plate to a SOI chip. There is a transparent conductor (ITO) on the glass for contacting and an alignment layer. Spacers keep the cell at a well-defined thickness. The director is in the plane of the surface throughout the cell and retains the orientation determined by the rubbed alignment layer. On the patterned chip surface the director is able to follow the local structures. This is observed with a polarizing microscope on specially designed test structures consisting of a waveguide flanked by a grating.

References

[1] Delta Technologies. *datasheet ito coated float glass substrates (cg-90in-0115).* `http://www.delta-technologies.com/Products.asp?C=13`.

[2] D. W. Berreman. *Solid surface shape and alignment of an adjacent nematic liquid-crystal.* Physical Review Letters, 28:1683, 1972.

[3] D. Taillaert, P. Bienstman, and R. Baets. *Compact efficient broadband grating coupler for silicon-on-insulator waveguides.* Optics Letters, 29:2749–2751, 2004.

[4] Norland optical adhesive. *datasheet uv curable glue 68.* `http://www.gentec.be/noa68.pdf`.

[5] C. Desimpel, J. Beeckman, K. Neyts, S. Verstuyft, D. Van Thourhout, K. d'Havé, and P. Rudquist. *Realization of a Four-Electrode Liquid Crystal Device With Full In-Plane Director Rotation.* IEEE Transactions on Electron Devices, 54:1295–1300, 2007.

[6] P. G. de Gennes and J. Prost. *The Physics of Liquid Crystals.* Oxford University Press, 1995.

[7] J. C. Jones, G. Bryan-Brown, E. Wood, A. Graham, Brett P., and J. Hughes. *Novel bistable liquid crystal displays based on grating alignment.* in Proceedings of the Society of Photo-Optical Instrumentation Engineers (SPIE), San José, CA, USA, pages 84–93, 2000.

[8] H. Desmet, K. Neyts, and R. Baets. *Modeling nematic liquid crystals in the neigborhood of edges.* Journal of Applied Physics, 98:123517, 2005.

[9] B. Bellini and R. Beccherelli. *Modelling, design and analysis of liquid crystal waveguides in preferentially etched silicon grooves.* Journal of Physics D: Applied Physics, 42:045111, 2009.

4

Tuning Ring Resonators

4.1 Introduction

In this chapter we discuss the measurements performed on the cells, fabricated as described in chapter 3. The physics and working principles outlined in chapter 2 will prove to be very useful in understanding and predicting the results. The chapter starts with an overview of the measurement equipment and setup. After this, the actual measurements are discussed. The focus is first on TE resonators where we cover two types of electrical tuning and thermal tuning. Then we describe the electrical tuning experiments on TM resonators. The chapter is concluded with a short section on the timescale on which the tuning takes place.

4.2 Practical measurement aspects

4.2.1 Setup overview

The chip under study is fixed on a vacuum chuck (see Figure 4.1). Light from an optical fiber is coupled into the waveguides through grating couplers (these will be explained in section 4.2.2). As a light source we use a tunable laser which ensures high power at a chosen wavelength. As the grating couplers are designed for a specific linear polarization (TE or TM) we make use of polarization paddles to set the correct polarization before the light is coupled to the waveguides. The

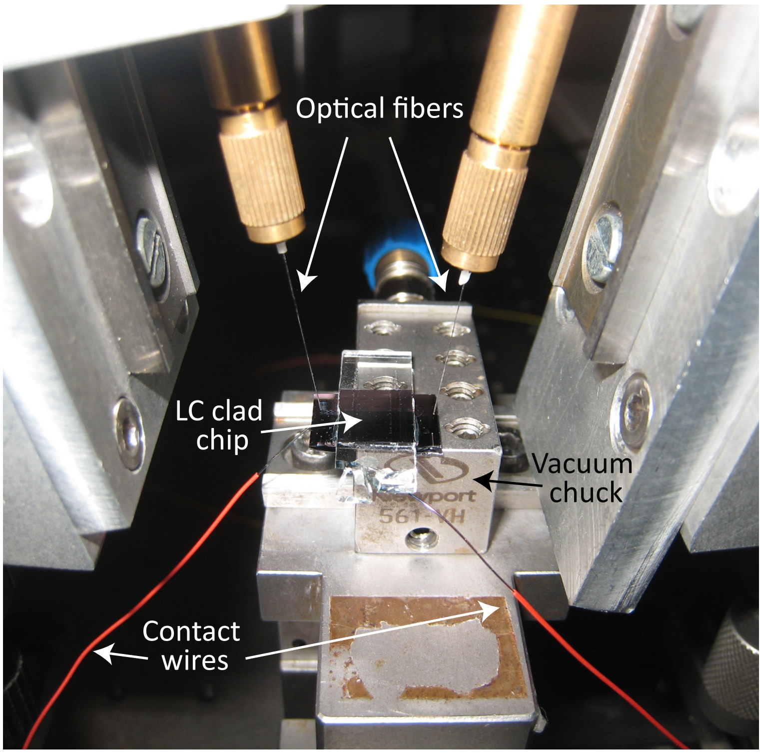

Figure 4.1: Photograph of the measurement setup. The cell is fixed on a vacuum chuck. Light from an optical fiber is coupled in and out of the waveguide through grating couplers. The second optical fiber captures the outcoming light. The metallic wires allow for easy contacting.

light from the output grating coupler is collected with a second optical fiber and fed to a power meter. All optical instruments are connected to a labview computer program to collect data and set the correct parameters. With a standard AC voltage source we apply an electric field with the desired frequency and amplitude. The AC is needed to prevent ion drift in the cell [1]. We generally work with frequencies in the order of 10 kHz. As we have shown before (equation 1.20), the director will not flip up and down due to the E-field as it reacts to the square of the field. The ions present in the LC will not drift towards the electrodes but merely oscillate. They are thus prevented from shielding the electrodes and deteriorating the performance of the device.

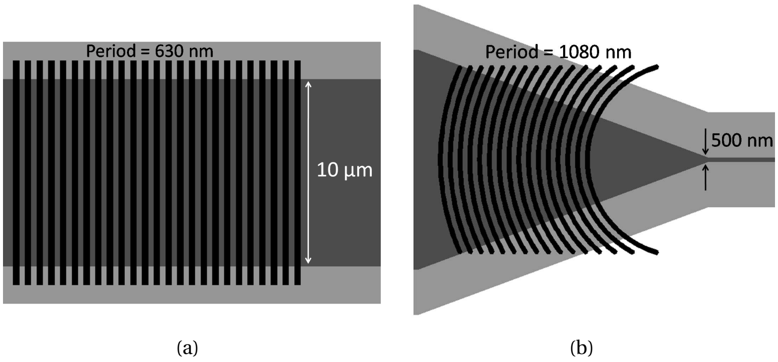

(a) (b)

Figure 4.2: (a) Top view of a TE grating coupler. (b) Top view of a TM grating coupler. The dark grey areas represent the silicon where the light grey areas represent the trenches around the waveguides. The black lines are etched 70 nm deep.

4.2.2 TE and TM grating couplers

To efficiently characterize SOI waveguide devices, we couple light from an optical fiber to the waveguides through grating couplers. This allows for a very easy alignment, which is much less critical than facet coupling. The couplers for TE and TM light have different specifications and we will describe them here separately.

TE grating couplers (see Figure 4.2(a)) are typically 10 μm wide and couple light from the optical fiber to 10 μm wide ridge waveguides [2]. Long adiabatic tapers reduce the waveguide width to around 500 nm. The grating couplers are first order diffraction gratings. They are etched 70 nm deep into the Si waveguide. The grating period is 630 nm with a fill factor of 50%. This results in a coupling efficiency of around 30% at a wavelength of 1550 nm. The spectral window (1 dB bandwidth) of these couplers is around 40 nm. The dimensions of the couplers (10 μm by 10 μm) allow for easy and accurate alignment of the fibers, using piezoelectrically controlled translation stages. The efficiency can be increased by making use of raised grating couplers. Coupling efficiencies of -1.6 dB have been demonstrated [3].

Coupling TM polarized light to a SOI waveguide is somewhat more tricky. A major problem is that it is not possible to use regular tapers for TM polarized light in asymmetrical waveguides. In this section, when a waveguide is named symmetrical, this means that the top cladding is equal to the bottom cladding. In symmetrical waveguides there are two symmetry planes: the horizontal XZ-plane and the vertical YZ-plane (see Figure 4.3(a)). The vertical symmetry (M_V) defines the distinction between quasi-TE and quasi-TM modes. The horizontal

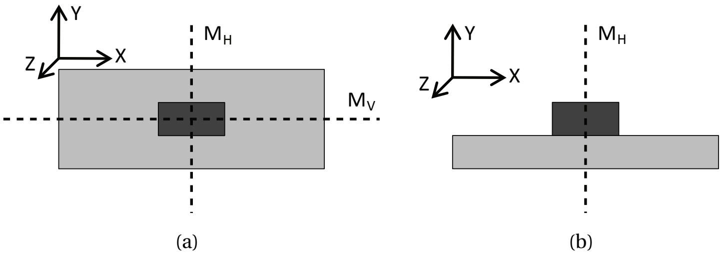

Figure 4.3: (a) Schematic cross section of a symmetric waveguide. (b) Schematic cross section of an asymmetric waveguide.

symmetry (M_H) allows a classification of the modes into even and odd. When the vertical symmetry is broken (see Figure 4.3(b)), one can not make a clear distinction between the different quasi-polarized modes. Physically this means that the electric fields of the quasi-TM and quasi-TE modes are no longer purely even or odd (symmetrical or anti-symmetrical) along the y-direction. This is the case in the waveguides used in this work as one cladding consists of oxide and the other of liquid crystal. The quasi-polarization classification disappears, or in other words the orthogonality between quasi-TE and quasi-TM disappears, and the polarizations can couple to each other in adiabatic tapers [4]. In Figure 4.4 we show the effective refractive index as a function of the waveguide width for both symmetrical and asymmetrical waveguides. For asymmetrical waveguides the conversions (the anti-crossings) from the fundamental quasi-TM mode to the higher order quasi-TE modes are indicated.

As the conventional adiabatic tapers do not transmit the fundamental quasi-TM mode, we use focused grating couplers (see Figure 4.2(b)) for TM polarized light in this work. These gratings couple and focus the light at the same time into the 500 nm narrow waveguides. The gratings have a period of 1080 nm and a fill factor of 55% (45% is etched, with an etch depth of 70 nm). An efficiency of 13% was demonstrated [4] for coupling from a fiber to a photonic wire of 220 nm thick and 500 nm wide. The 1 dB spectral window is about 45 nm.

4.3 TE Ring Resonators

In this section we focus on the tuning of ring resonators guiding TE polarized light. The method discussed in the first and most important part is electrical tuning. We distinguish between top-bottom tuning where the electric field is oriented perpendicular to the chip and in-plane switching, where the electric fieldlines run in the plane of the chip. Finally, we briefly dicuss the thermal tuning of TE resonators with a liquid crystal cladding.

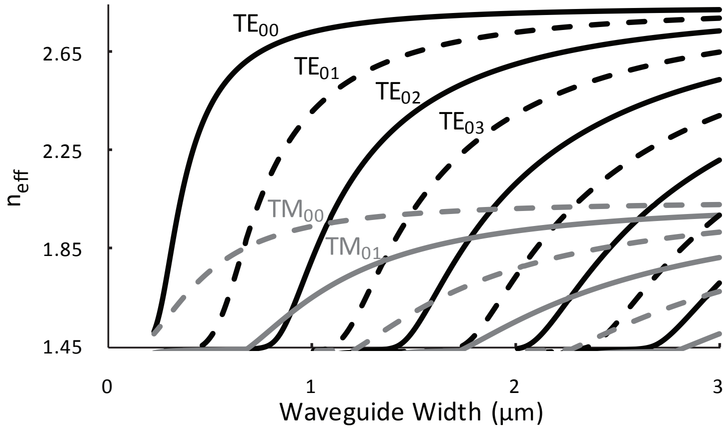

(a)

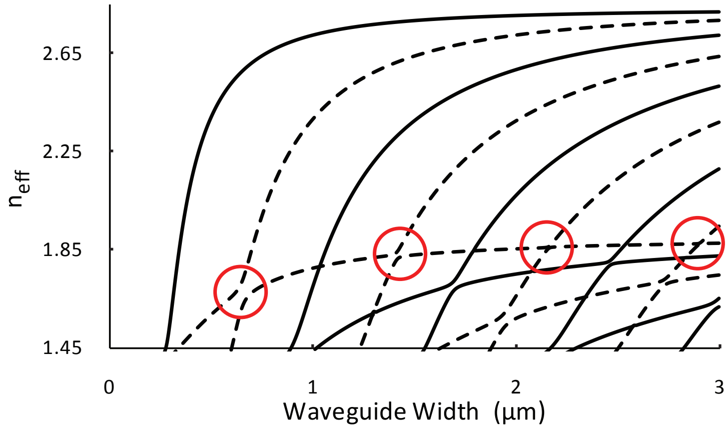

(b)

Figure 4.4: (a) Effective refractive index (n_{eff}) as a function of waveguide width in symmetric waveguides. The Si waveguide is surrounded by SiO_2 (n = 1.45). The TM modes are indicated in grey, the TE modes in black. The odd modes are represented by dashed lines. (b) Effective refractive index (n_{eff}) as a function of waveguide width in asymmetric waveguides. The SOI waveguide has an air cladding. Some anti-crossings are indicated with a red circle. Mode conversion from the lowest order TM mode to higher order TE modes will occur here in adiabatic tapers.

4.3.1 Electrical tuning: top-bottom

Top-bottom tuning is the most straightforward method of tuning as the cell setup is quite simple. A uniform ITO layer on the covering glass plate acts as top electrode while the Si substrate acts as the bottom electrode. These two electrodes are hooked up to a voltage source and the resulting electric fieldlines run perpendicular to the chip and the glass plate. The LC director tries to reorient itself from an orientation along the waveguides to an orientation along the fieldlines, perpendicular to the waveguides. This will cause a change in refractive index of the cladding as seen by the waveguide mode. As the effective refractive index of the mode changes, so will the resonance wavelength of the ring resonators.

4.3.1.1 Specifications of the device

The SOI waveguides used here are 220 nm high and 450 nm wide. The bus waveguides are equipped with TE grating couplers as described in section 4.2. The ring consists of four straight waveguides connected by 90 degree bends. The bend radius is 15 μm and the straight sections are 12 μm long. This adds up to a total length of 142 μm. The coupling section, where the ring waveguide and the bus waveguide can couple to each other, is 250 nm wide and 2 μm long. The LC layer is 6 μm thick and the rubbing direction is parallel to the majority of the waveguides and the coupling section.

4.3.1.2 Visual inspection

Under a polarizing microscope we can clearly see the alignment around the resonators. When the polarizer is oriented parallel to the rubbing direction the image remains dark except where the director twists. This was explained in chapter 3. In the middle of the microscope image shown in Figure 4.5 there is a black region. This is the trench around the resonator where the Si is etched away. The SiO_2 surface is flat and the director remains parallel to the rubbing direction as defined on the top glass plate. As there is no twist of the director in this region, there is no transmission of light. Waveguides that are not parallel to the rubbing direction are bright. The director twists throughout the cell [5] causing transmission of light through the second polarizer. However, there are two possible ways for the director to twist: along a right-handed helix and left-handed one. The ring waveguide is divided in 4 regions because of this. Regions 1 and 3 see the director twist in a right-handed helix, whereas regions 2 and 4 are characterized by a left-handed one. Transitions 4-1 and 2-3 is smooth as there is no sudden jump between the regions of different handedness. Transitions 3-4 and 1-2 are more problematic and a dark border between the bright regions appears. The director orientation is not well defined along this disclination that runs between the chip and the glass plate. From a waveguide mode point of view, the disclination can be seen as a part of the ring where the director (and so the cladding) behaves unpredictably. This may cause equally unpredictable tuning behaviour and the introduction of extra scatter losses. We estimate that this region stretches about 5 μm along the waveguide. On a total length of 142 μm this is still rather small but in smaller ring resonators the disclinations can become problematic.

When a voltage is applied the image becomes totally dark after an initial moderate brightening (Figure 4.6). This somewhat brighter image at 5 V is likely due to a small planar reorientation of the director in the bulk of the LC at voltages too low to force the director fully vertical. At 10 V the image is almost completely dark indicating a vertical director orientation in the bulk. Higher voltages will reorient the director mostly at the surfaces where the anchoring forces holding the director are stronger than in the bulk. When the polarizers make an angle with the rubbing direction the image (Figure 4.7) is bright as the birefringent LC causes transmission of light through the second polarizer. For increasing voltages the image darkens again until the director is fully vertical (Figure 4.7). As a conclusion we can say that the director is everywhere parallel to the rubbing direction as defined on the glass plate except where there are structures on the surface. There, the director follows the local structures. When a voltage is applied between the ITO and the Si substrate, the resulting electric field reorients the director to a vertical orientation.

4.3.1.3 Tuning the resonance

After the cell is filled with LC, it is fixed on a metal vacuum chuck (see Figure 4.1). We couple TE light in the optical waveguides with a tunable laser and capture the outcoming light with a detector. A voltage source is connected to the bottom of the substrate and to the ITO electrode (at the top of the LC cladding). We apply an AC voltage (10 kHz) to the cell and increase the amplitude in steps. The output spectra for different voltages can be seen in Figure 4.8. For low voltage levels the resonance remains at the same wavelength. The electric field is too weak to compensate for the elastic forces holding the LC in place. The reorientation of the director due to the electric field will first take place in the bulk of the cell and at higher voltages the effect will spread towards the surfaces. Our measurements show that at a voltage level of 3V the resonance wavelength starts to move, indicating that the LC director near the surface starts to reorient itself along the electric field lines (Freedericksz transition). The resonance wavelength shifts towards shorter wavelengths. The steepest part of the tuning curve (Figure 4.9) lies between 20 V and 40 V with a tuning of about 0.09 nm/V. For higher voltages the tuning slows down until no further tuning can be achieved by increasing the voltage. This means that the director throughout the cell is fully oriented along

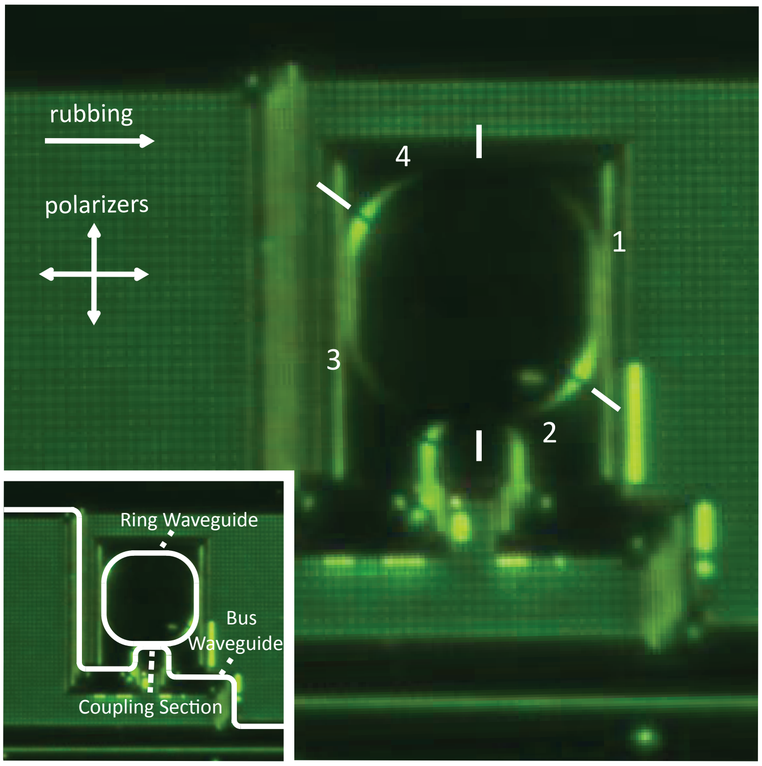

Figure 4.5: Polarization microscope image of a ring resonator with a cladding of LC. The inset shows a schematic view of the waveguides over the microscope image. The first polarizer is oriented parallel to the rubbing direction on the glass plate rendering all parts of the image where there is no director twist dark. The waveguides perpendicular to the rubbing direction appear bright indicating that the director follows local structures on the surface. The numbers indicate regions of different director handedness (right and left-handed). The small white stripes mark the boundaries of the regions. Between region 3 and 4 and between 1 and 2 dark interuptions mark disclinations in the LC layer.

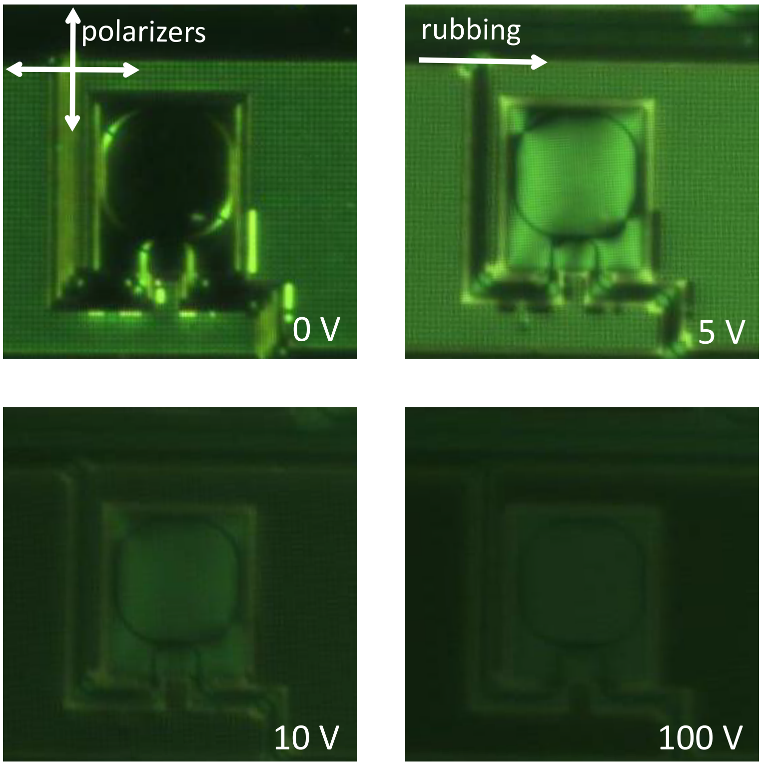

Figure 4.6: Polarization microscope images of the ring resonator for increasing voltages. The rubbing direction is parallel to the first polarizer. The bright parts of the image gradually darken as the electric field reorients the director vertically.

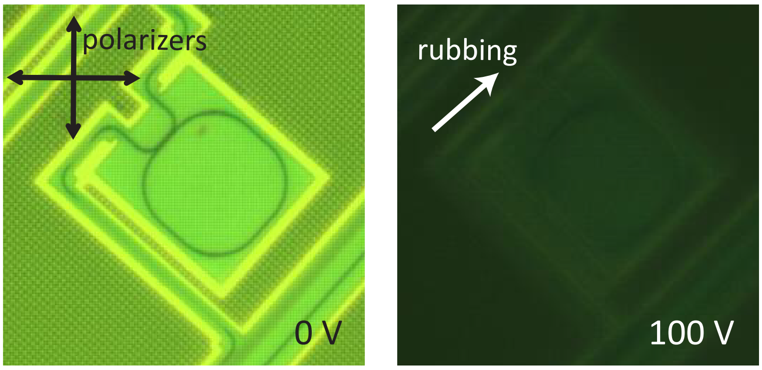

Figure 4.7: Polarization microscope images of the ring resonator for increasing voltages. The rubbing direction is at an angle with the first polarizer. The bright image gradually darkens as the electric field reorients the director vertically.

the vertical fieldlines. The maximal tuning range is reached at around 100 V. By then the resonance wavelength has shifted 4.5 nm. This corresponds with a Δn_{eff} of 0.01. In Figure 4.9, the threshold for the tuning can clearly be seen, as can the saturation effect at higher voltage levels.

Tuning mechanism. As discussed in chapter 2 the different electric field components of the waveguide mode interact with the LC cladding. Initially, the director is oriented along the waveguide (z-axis). When a high voltage is applied, the director is aligned along the y-axis. The z-component of the electric field experiences a decrease in dielectric constant in the cladding. The y-component experiences an increase. As the z-component is by far the biggest of the two, the effective index of the waveguide mode will decrease with increasing voltage.

Q-factor. From Figure 4.8 we can see that the width of the resonance peak changes throughout the tuning process. We fit the peaks to a Lorentzian function to calculate the FWHM and Q-factor. The Q-factor as a function of voltage is depicted in Figure 4.10. For voltages lower than 10 V the FWHM of the peak remains stable at 0.041 nm. This translates to a Q-factor of 37830. When the voltage level increases further, we see that the peaks become wider and the Q-factor decreases. At 30 V the Q-factor is about 16000. This remains more or less stable up to 70 V. At 80 V and 90 V the Q-factor is at its lowest level, around 8000. It rises again at 100 V, when the reorientation of the director is complete. As the Q-factor is a measure for the losses in the ring waveguide, these losses somehow increase during the tuning. We believe that the fluctuation of the Q-factor may be due to the appearance and disappearance of domains on the surface of the

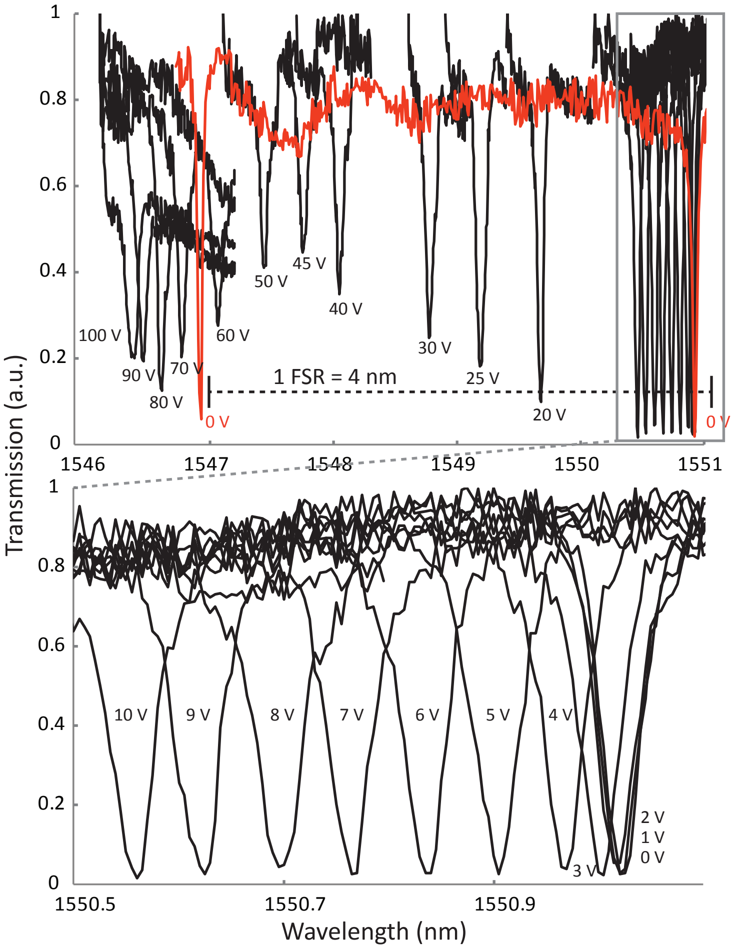

Figure 4.8: Transmission of a ring notch filter with LC cladding for increasing voltages. The red curve at 0V shows two peaks, indicating the free spectral range of the ring resonator. The voltage is shown at every peak.

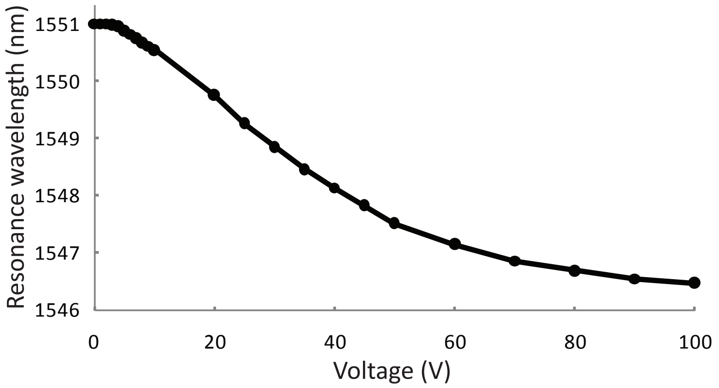

Figure 4.9: Resonance wavelength of the ring resonator (transmission is seen in Figure 4.8) as a function of voltage. Note the threshold voltage around 3 V and the saturation at high voltages.

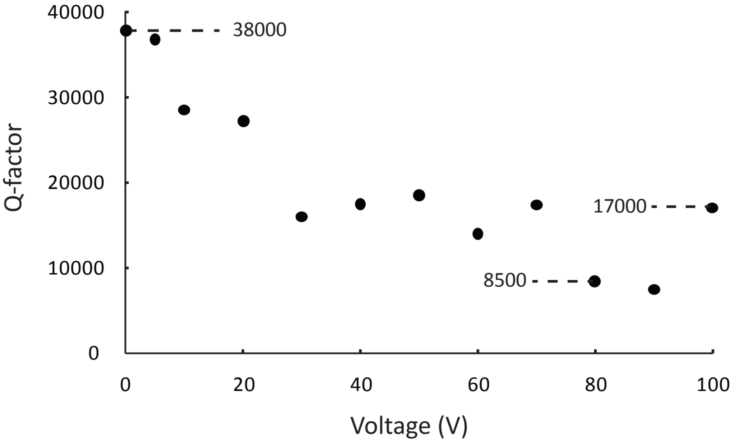

Figure 4.10: Q-factor of the TE ring resonator as a function of voltage.

chip. The vertical reorientation of one domain may be a bit stronger or a bit weaker than is the case in a neighbouring domain. Even if this difference is very small, it introduces extra scattering losses in the ring and thus a drop in the Q-factor of the resonator. This drop follows from equation 1.35. Likely, also the coupling between the ring and the bus waveguide changes a little in the tuning process, which, again through equation 1.35, has an effect on the Q-factor. It is not trivial, however, to give an estimate of the magnitude of this effect.

Free Spectral Range. The tuning range achieved here is 4.5 nm. As this is more than one FSR, we are able to address all wavelengths with this specific device. However, as modesty is the best policy, we note that the FSR depends on the length of the ring resonator. For smaller resonators the FSR increases but the tuning range does not. At some point we will not be able to cover an entire FSR with this tuning mechanism.

Voltage drop. As the Si substrate acts as bottom contact in the LC cell, there is a considerable voltage drop across the oxide layer. We can easily calculate this, assuming the LC cell can be approximated as two parallel plate capacitors in series. One is filled with SiO_2 and the other with LC. The permittivity of SiO_2 in the kHz range is 3.9 [6] where the LC's permittivity values are 5.1 and 19.8 (E7). We calculate the voltage drop in a cell with 2 μm SiO_2 and a 6 μm thick E7 cladding.

$$V = V_{ox} + V_{LC} = \int_0^{2\mu m} \frac{E_0}{\epsilon_{ox}} dx + \int_{2\mu m}^{8\mu m} \frac{E_0}{\epsilon_{LC}} dx \tag{4.1}$$

$$\Rightarrow E_0 = \frac{V \epsilon_{ox} \epsilon_{LC}}{2(\epsilon_{LC} + 3\epsilon_{ox})\mu m}, \tag{4.2}$$

with E_0 the electric field in vacuum, V_{ox} and V_{LC} the voltage across the oxide and the LC and ϵ_{ox} and ϵ_{LC} the permittivities of the oxide and the LC. From equation 4.1 the voltages across the oxide and the LC can be determined:

	V = 1 V	**V = 100 V**
ϵ_{LC}	5.1	19.8
V_{ox}	0.3 V	63 V
V_{LC}	0.7 V	37 V

Note that at high voltage levels we have to take the extraordinary dielectric constant into account. This calculation shows that the entire tuning curve presented above can be achieved with 37 V instead of 100 V provided the bottom electrode can be integrated on top of the chip.

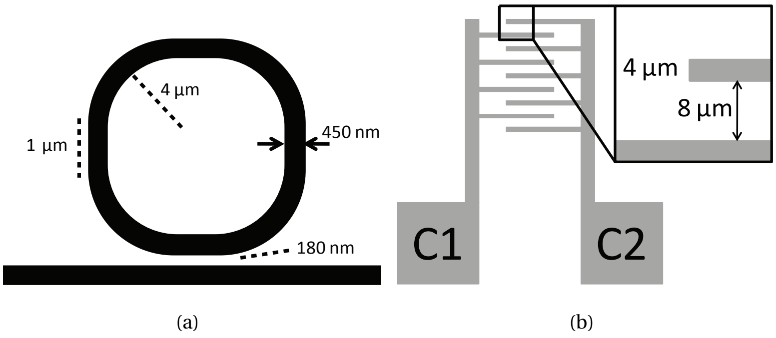

(a) (b)

Figure 4.11: (a) Schematic view of a ring resonator as used in the IPS experiments. (b) Schematic view of the finger electrodes.

4.3.2 Electrical tuning: in-plane switching

A somewhat less straightforward method of tuning TE ring resonators with a LC cladding is in-plane switching (IPS). Instead of reorienting de director to a vertical orientation it can be turned in the plane of the chip. In the ITO layer on the glass cover, interdigitated electrodes are etched. They provide a horizontally oriented E-field twisting the director. The refractive index in the cladding will undergo a change that influences the resonance wavelength of the resonators.

4.3.2.1 Specifications of the device

The rings used for this experiment are very small (Figure 4.11(a)). They have a bend radius of 4 μm with 4 straight sections of 1 μm. The waveguide is 220 nm high and 450 nm wide. The gap between the bus and the ring waveguide is 180 nm. The electrodes are etched in a fingerpattern in the ITO. The fingers are 4 μm wide and are spaced 8 μm apart (Figure 4.11(b)). Through contact pad C1 and C2 an electric field can be applied between the finger electrodes. The cell is about 2 μm thick. The rubbing direction is parallel to the bus waveguide.

4.3.2.2 Visual inspection

The polarization microscope offers a first indication of the workings of an IPS cell. From what we learned in previous sections of this thesis we can more or less predict what will happen. When no voltage is applied and the polarizer is parallel or perpendicular to the rubbing direction most of the image is black except around waveguides that do not run parallel to the rubbing. Here the image is bright as the director twists throughout the cell to align to the sidewalls of the waveguides. As can be seen in Figure 4.12 this is a correct assumption. Note

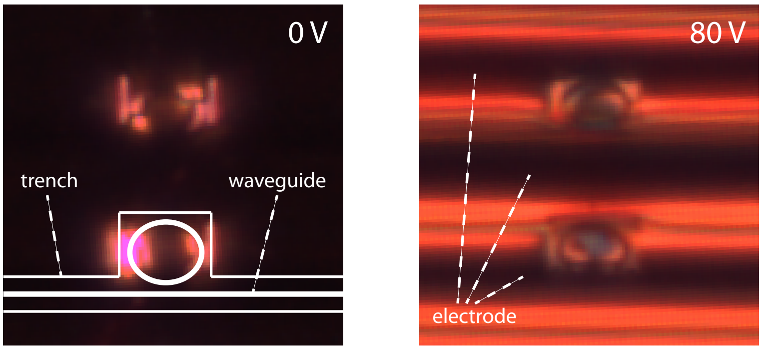

Figure 4.12: Polarization microscope image of ring resonators in an IPS electrode configuration. When a voltage is applied the image brightens as the director turns in the plane.

that we can again see the dark disclinations separating regions of uniform twist. The rings are much smaller than in the previous experiments and we expect a bigger influence of these disclinations on the tuning behaviour as they now take up a considerable part of the ring waveguide. When the voltage between the electrodes increases the cell becomes bright due to a twisting director. Between the dark electrodes there are two bright regions separated by a thin dark stripe. This can be interpreted as a twist of the director reaching 90 degrees in between two electrodes. It is therefore also clear that the director is far from uniform throughout the cell, which causes problems regarding alignment of the electrodes to the rings. Moreover, the region directly below the electrodes remains dark, indicating that the director there is unaffected by the electric field or shows a pure tilt. The latter is more likely as the substrate is a conductor and may act as a third electrode at 0V. At 0V, the disclinations (also discussed in section 4.3.1) are visible. As opposed to the top-bottom tuning experiments, the disclinations take up a large part of the very small rings. This can be seen in the left part of Figure 4.12. As the exact director orientation in these regions is not well known we expect that this can pose considerable problems for the tuning range.

4.3.2.3 Tuning the resonance

The cells are filled with E7 and fixed on the vacuum chuck of the setup. Light from a tunable laser is coupled into the waveguides and the optical output is measured with a power meter. We apply 10 kHz voltage to the electrodes and increase the amplitude in steps. At low voltage levels the resonance wavelength remains at its initial position indicating that the field is too weak to reorient the director. When the threshold voltage is reached the resonance starts to shift. This threshold is directly related to the distance between the electrodes. After an

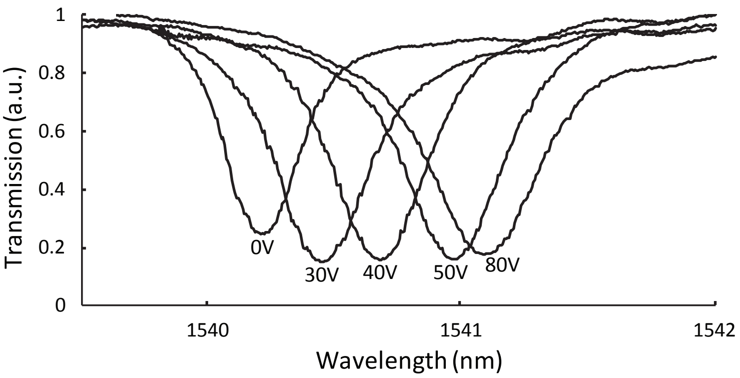

Figure 4.13: Transmission of a notch filter with LC cladding for different voltages in an in-plane switching cell.

initial small drop, the resonance wavelenght increases with increasing voltage. Between 20 V and 50 V the resonance shifts about 0.025 nm/V (see Figure 4.13). For higher voltages the shift saturates as the director reaches its maximal twist angle. At 80 V the resonance has shifted about 0.9 nm (Figure 4.14) compared to the situation without voltage. The tuning range is considerably lower than the 4.5 nm achieved in the top-bottom electrode configuration. This might be partly due to the larger relative size of the disclinations discussed above. A larger part of the ring waveguide will behave unpredictably and this could have a negative influence on the tuning range. A second cause of the reduced tuning range is the fact that the ring waveguide sees a continuously changing effective index. The ring sections parallel to the electrode fingers see the director twist 90 degrees from its initial alignment to the waveguides. The regions perpendicular to the electrode fingers will see no effect at all. This means that only a part of the ring will contribute to the resonance tuning.

Tuning mechanism. Initially the director is oriented along the z-axis. Under the polarization microscope it has become clear that between two electrode fingers the director twists to reach 90 degrees in the middle. The fieldlines running from one electrode to the other describe an arc and will cause the director in regions close to the edges of the electrodes not only to twist but also to tilt. As the director orientation is not uniform it is somewhat harder to predict what exactly will happen to the resonance. When a waveguide is nicely in between two electrodes the director in its cladding will purely twist in the plane. This causes an increase in ϵ_x and a decrease in ϵ_z. The transversal component of the electric field of the mode interacts the most with the cladding

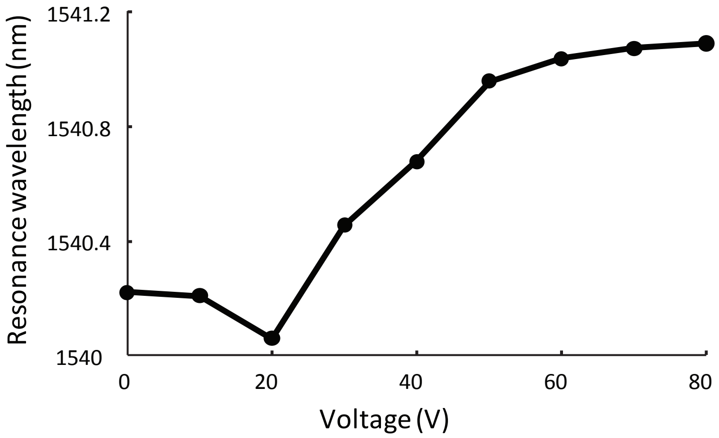

Figure 4.14: Trace of the resonance wavelength as a function of applied voltage.

so a net increase of the effective refractive index is to be expected. When the waveguide is closer to an electrode, the situation becomes more complicated. The effects of the tilt and twist of the director work against each other and it is hard to say what the resulting change in effective refractive index will be. Directly below the electrode the director most likely tilts causing a decrease in effective refractive index. This effect may explain the initial dip in the resonance wavelength.

Electrode distance. In this work the cells are made manually, without making use of machinery to align the electrodes to the rings. The director orientation is not uniform throughout the cell. It is divided into a sequence of identical regions. Pure twist is found in the middle between two electrodes. Therefore, the positioning of the rings between two electrode fingers is critical to have optimal tuning behaviour. With our rudimentary method of making the cells, we rely on a bit of luck to find a ring in a reasonably good position. Even when the alignment is not perfect, we can expect that at least a part of the ring will see the in-plane director reorientation. When the distance d between the electrode increases, it becomes more and more likely that a ring benefits from an optimally aligned cladding. However the voltage needed to tune a cell will increase as well as the electric field scales inversely with d^2. In the measurement presented above we can not guarantee that the ring experiences a pure twist of the director in the cladding. It is possible that with careful alignment a wider tuning range can be achieved.

Q-factor. The Q-factor of the LC clad rings without voltage applied is about

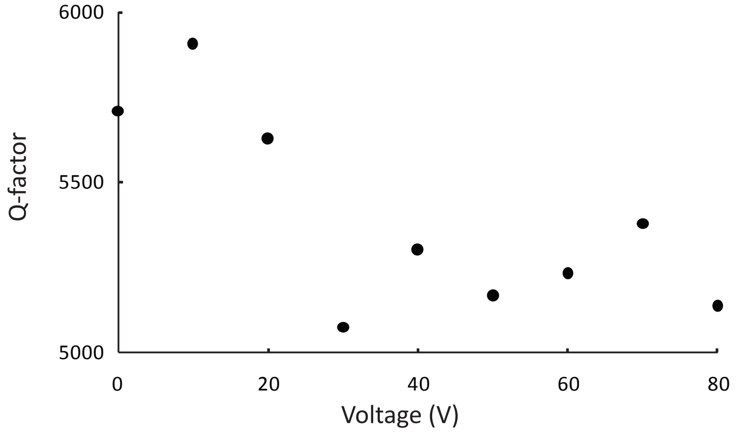

Figure 4.15: Q-factor of the ring resonator as a function of applied voltage.

5700 (Figure 4.15). When the resonance starts shifting, the Q-factor drops to 5250. This remains more or less constant for increasing voltages. Again we think that the formation of some LC domains on the surface during tuning may cause extra scattering losses. Note that the Q-factor in general is quite low in these experiments. This is caused partly by the short length of the ring waveguide. Equation 1.35 shows that shorter lengths mean lower Q-factors.

4.3.3 Temperature tuning

Silicon has a large thermooptic coefficient ($1.8*10^{-4}$ $/^{o}$C) and tuning SOI ring resonators with heaters is therefore a widely researched domain [7, 8]. In the absence of the LC cladding, our ring resonators (with waveguides of 500 nm wide and 220 nm high) exhibit a shift of 0.8 nm of the resonance wavelength per 10 ^{o}C temperature rise. When the rings are clad with LC, the thermooptic properties of the LC will translate into an altered temperature tuning behaviour.

4.3.3.1 Tweaking the setup

The optical part of the setup is identical to that of the electrical measurements. Light from a tunable laser is coupled via optical fibers into and out of the waveguides by means of grating couplers. The output is fed to a power meter. A Peltier element is integrated under the vacuum chuck which holds the chip. The temperature at which we measure the output can now be accurately controlled.

4.3.3.2 Tuning the resonance

The output of ring resonators in an empty cell is measured in steps for increasing temperatures. The resonance wavelength shifts about 0.8 nm per 10 ^{o}C towards longer wavelengths as is to be expected from a SOI resonator. The cell is then filled with 5CB. This LC is very similar to E7 but it has a much lower clearing temperature (around 35 ^{o}C), which makes it more suited for the study of temperature response. Again the temperature is increased in steps. Initially, the resonance shifts in a linear fashion towards longer wavelengths. The slope is somewhat less steep than in an empty cell (0.073 nm/^{o}C as opposed to 0.079 nm/^{o}C). Around 45 ^{o}C there is a sudden drop seen in the resonance wavelength. It shifts 0.8 nm towards the blue side of the spectrum. As the temperature increases further, the resonance wavelength shifts again towards longer wavelengths at a rate of 0.053 nm/^{o}C. It is clear that the thermooptic constant of the LC is negative, as opposed to that of silicon. With careful waveguide design, control of the confinement and selection of an appropriate LC, the photonic structures may be made temperature insensitive as well as tunable. This has been done with polymers [9] and the same principles can be used here. We believe this can be a very interesting topic for further research.

Tuning mechanism Both the longitudinal (z-) component and the transversal (x-) component of the electric field of the light interact with the LC cladding. We leave the y-component out of consideration as it is by far the smallest of the three. In chapter 1 we have discussed the evolution of LC as a function of temperature. In figure 4.17 the values of the refractive indices of 5CB can be seen. For increasing temperatures, the x-component contributes positively to the effective refractive index of the mode as the refractive index along the x-axis increases in the cladding from n_o to n_{iso}. The z-axis contributes negatively as the refractive index along the z-axis decreases from n_e to n_{iso}. As n_e - n_{iso} > n_o - n_{iso} the net effect on n_{eff} will be negative. The effect is strongest around the clearing temperature as the refractive index of the LC changes rapidly. The clearing temperature seen from our experiments is between 43 ^{o}C and 45 ^{o}C. That this is higher than the actual clearing temperature of 5CB (around 34 ^{o}C) is due to the fact that our setup controls the temperature at the bottom of the SOI chip and not at the LC layer as this is sealed off from the environment.

4.4 TM Ring Resonators

TM ring resonators (together with most other resonant structures guiding TM polarized light) are intrinsically more suited for tuning with cladding layers than their TE counterparts. The TM mode traveling in the waveguides is far

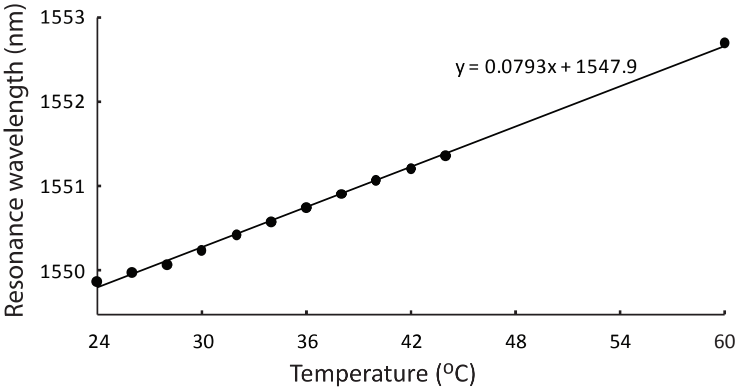

(a)

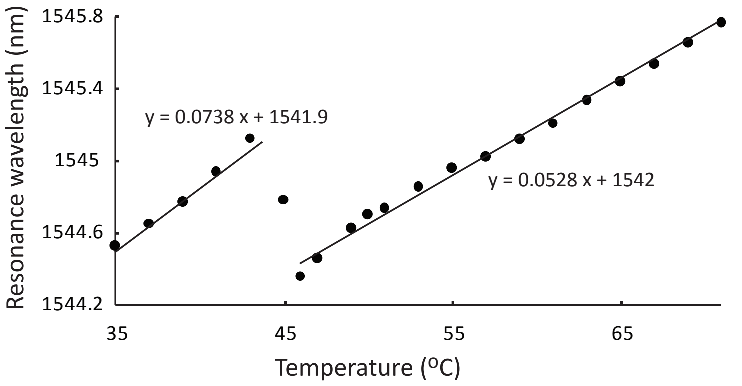

(b)

Figure 4.16: (a) Trace of the resonance wavelength of a ring resonator without LC cladding for increasing temperature. (b) Trace of the resonance wavelength of a ring resonator with 5CB cladding for increasing temperature. The horizontal axes show the temperature at the bottom of the substrate. The actual temperature of the LC is lower.

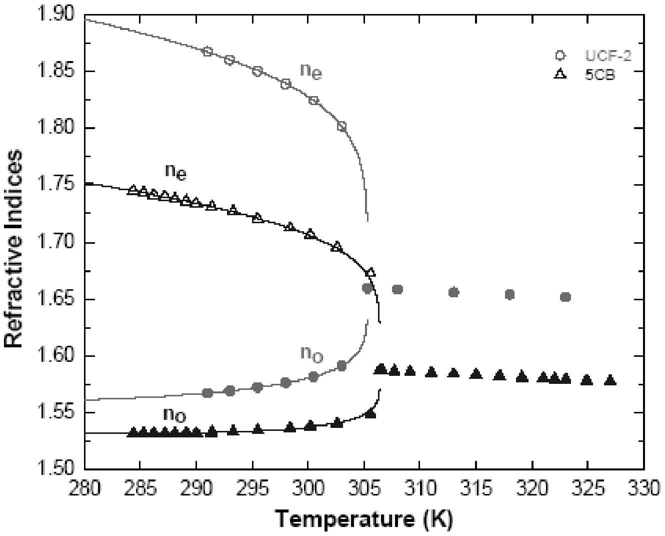

Figure 4.17: Temperature-dependent refractive indices of UCF-2 (a nematic liquid crystal mixture) and 5CB at λ=589 nm. Figure reproduced from [10]

less confined than the TE mode and has therefore much more overlap with the cladding material. The downside of using TM structures is that the lower effective index of the mode does not allow for structures as small or bends as sharp as in TE structures. In this section we go over our tuning experiments using TM ring resonators. The structures used here are very similar to those used in section 4.3.1 and the devices are constructed in the same top-bottom tuning configuration. Therefore we will only briefly describe the ring resonators and immediately show and explain the experimental results.

4.4.1 Specifications of the device

The SOI waveguides used in this section are 220 nm high and 450 nm wide. The bus waveguides are equipped with TM grating couplers as described in section 4.2. The ring waveguide consists of 4 straight waveguides connected by 90 degree bends. The bend radius is 20 μm and the straight sections are 10 μm long. This adds up to a total length of 166 μm. The coupling section, where the ring waveguide and the bus waveguide can couple to each other, is 550 nm wide and 4.5 μm long. The LC layer is 6 μm thick and the rubbing direction is parallel to the majority of the waveguides and the coupling section.

4.4.2 Tuning the resonance

Before measuring, the cell is filled with E7. It is then fixed on the vacuum chuck and substrate and ITO are connected to the voltage source. Light from a tunable laser is coupled into and out of the waveguides through TM grating couplers. The output is measured with a power meter connected to a pc. We apply a 10 kHz AC signal to the LC layer and increase the amplitude in steps. For very low voltage levels the resonance wavelength does not shift. Above 3 V we see a shift of the resonance towards longer wavelengths (Figure 4.18). At 100 V the wavelength range covered is 31 nm which covers several FSRs and nearly the entire C-band of optical communications. This wavelength range corresponds with a Δn_{eff} of 0.07. As in the TE experiments we see again a treshold voltage needed to start the tuning and a saturation effect at higher voltages, where the director is fully tilted. We start tracking a resonance 3 orders towards shorter wavelengths when we reach the boundaries of the transmission window of the TM grating couplers. At the steepest part of the tuning curve, the tuning reaches about 1 nm/V (Figure 4.19).

Tuning mechanism. The TM ground mode is much less confined to the waveguide core than the TE mode. This allows for better interaction with the cladding layers and explains the wider tuning range. The interaction is also fundamentally different as the normal (y-)component of the electric field of the mode is now the main player involved in the tuning. The director is initially oriented parallel to the waveguide and in the plane of the substrate. The y-component will experience a low value of the dielectric constant (ϵ_o) resulting in a low n_{eff} of the mode. As the director reorients vertically the Y-component experiences a dielectric constant that evolves more and more towards ϵ_e. The n_{eff} together with the resonance wavelength of the ring resonator will increase.

Q-factor. As can be seen from Figure 4.18 the Q-factor of the ring increases for intermediate voltage levels and decreases again at high voltages. We fit the peaks to a Lorentzian function and extract the Q-factor. They are plotted in Figure 4.20. The Q-factor drops from a value of 11500 to a value of 4000 during the tuning and rises again to around 10000 at high voltages. We believe that domains can be formed on the chip surface (as discussed before) when the director reorients introducing extra losses. A complete reorientation reduces the number of domains again and the Q-factor rises.

Free spectral range. The tuning range greatly exceeds the FSR. We can therefore address all wavelengths in the C-band of optical communications. Even if the rings would be made smaller (the FSR will then increase), it will remain possible to address any wavelength in the C-band.

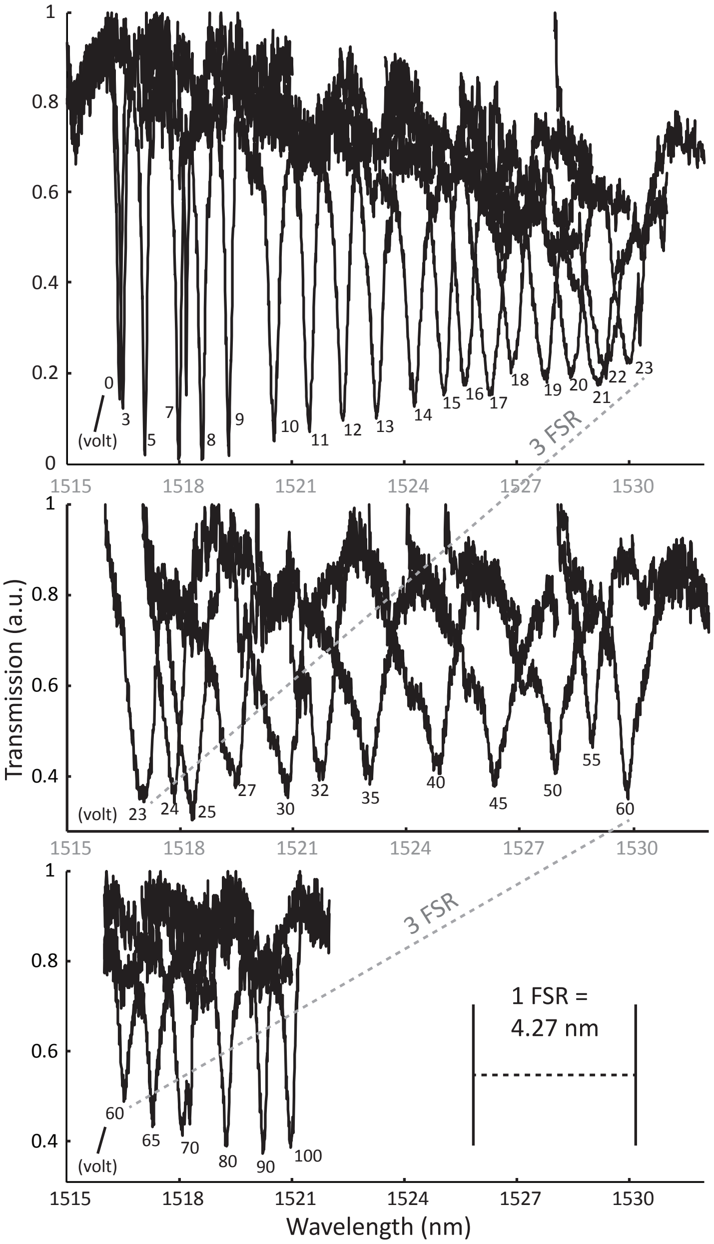

Figure 4.18: Transmission of a ring notch filter with LC cladding for increasing voltages. The rings guide the TM mode.

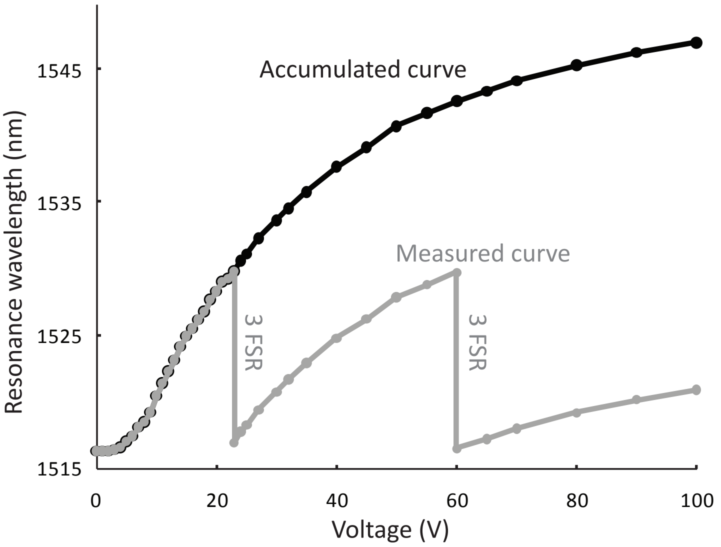

Figure 4.19: Resonance wavelength of a ring resonator guiding TM light, as a function of voltage. The curve in gray represents the measured data points. At certain voltages, we jump back 3 FSRs. The curve in black shows the accumulated curve.

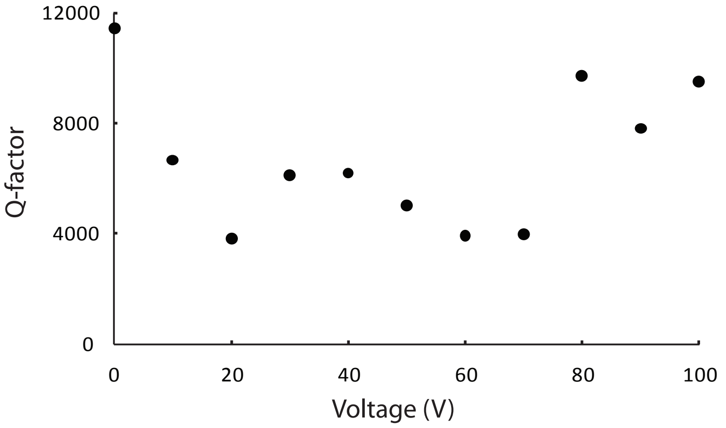

Figure 4.20: Evolution of the Q-factor of TM ring resonators with LC cladding for increasing voltage levels.

Voltage drop. The considerations we made while discussing the top-bottom tuning method of TE ring resonators, are valid here as well. There is a considerable voltage drop across the insulating oxide layer separating the contacted substrate from the LC cladding layer. The voltages used here can therefore be a lot lower, provided an electrode is designed and implemented directly below the cladding layers.

4.5 Dynamic behaviour of electrical tuning

Up to now we have not discussed the timescales on which the tuning takes place. To measure the tuning speed we supply an AC voltage of 10 V at 100 kHz for 500 ms. Then we cut off the voltage for 250 ms and repeat the process. The ring under study guides TE light and has a bend radius of 6 μm. We connect the substrate and the ITO layer to the voltage source. In Figure 4.21 the transmission of the ring resonator with and without voltage is shown. The asymmetry seen in the dips is due to thermal nonlinear effects. As we approach the resonance wavelength with the tunable laser from the shorter wavelength side, we start to couple light into the ring. Power builds up, heating the structure. This causes an increase of the effective index, which then shifts the resonance wavelength slightly towards longer wavelengths. This effect stretches out the left slope of the resonance dip. When the wavelength of the tunable laser gets longer than the resonance wavelength, the structure cools down, shifting the resonance wavelength back to the blue. This results in a very sudden and steep slope on the right side of the resonance. Both the Si and the LC can contribute to this effect, but as their thermooptic effects are different in sign (in our case), they work against each other, as was shown in Figure 4.16. We adjust the tunable laser to emit light at the resonance wavelength of the ring without voltage applied. The transmitted power as a function of time is shown in Figure 4.22. As expected, the transmission is high when a voltage is applied and low otherwise. We estimate the rise and falltime to be about 50 ms. The estimations, however, are made difficult by the seemingly gradual increase of losses when voltage is applied. At the moment, we do not have a clear explanation for these losses. This should be investigated further. However, from this experiment, we can conclude that our devices can be tuned in about 50 ms. This can be shortened when we go to other, faster switching liquid crystals. The thickness of the cell has an influence on the switching speed as well. Generally, thinner cells will switch faster, but we need to be a bit careful with that statement. First, for thin cells, the combined anchoring forces from the top and bottom substrate will hold the molecules firmly in place. Second, one should be careful not to make the cell too thin. When the ITO gets too close to the waveguide, the light can get absorbed. This is

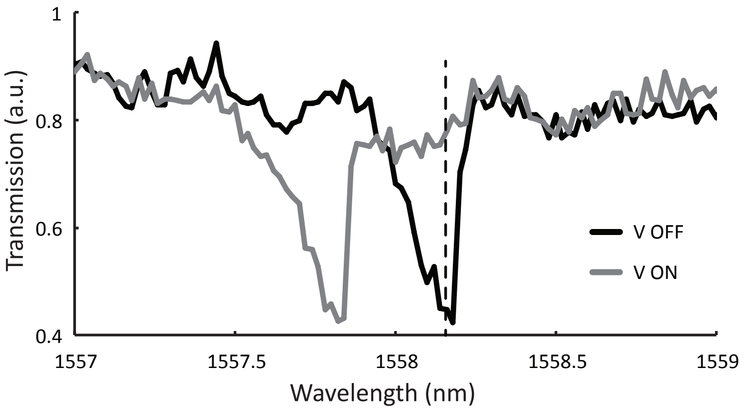

Figure 4.21: Transmission of the ring resonator as a function of wavelength. The peak shifts when a voltage (10 V) is applied. The dashed line represents the wavelength (1558.16) used in Figure 4.22. At this wavelength the output is high when a voltage is applied and low when no voltage is applied.

especially important for less confined modes like the TM mode. We suggest a minimum of 3 μm thickness.

4.6 Conclusion

In this chapter, we have discussed the experimental tuning of TE and TM ring resonators. TE ring resonators can be tuned 4.5 nm towards shorter wavelengths in a top-bottom electrode configuration and about 1 nm towards longer wavelengths in an in-plane switching cell. The TM mode is less confined to the waveguide core and therefore offers more interaction with the cladding layers. We have demonstrated 31 nm tuning towards longer wavelengths for ring resonators guiding TM polarized light. The different tuning mechanisms are now well understood and explain the results that we achieved.

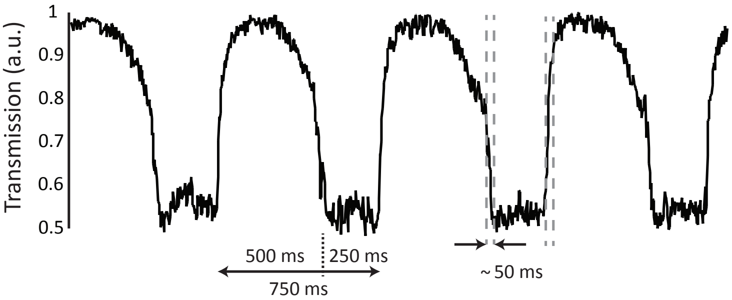

Figure 4.22: Transmission of the ring at 1558.16 nm as a function of time. A voltage (10 V) is applied for 750 ms and cut off for 250 ms. Rise and fall time are estimated to be about 50 ms.

References

[1] A. Di Falco and G. Assanto. *Tunable wavelength-selective add-drop in liquid crystals on a silicon microresonator.* Optics Communications, 279:210–213, 2007.

[2] D. Taillaert, P. Bienstman, and R. Baets. *Compact efficient broadband grating coupler for silicon-on-insulator waveguides.* Optics Letters, 29:2749–2751, 2004.

[3] D. Vermeulen, S. Selvaraja, P. Verheyen, G. Lepage, W. Bogaerts, P. Absil, D. Van Thourhout, and G. Roelkens. *High-efficiency fiber-to-chip grating couplers realized using an advanced CMOS-compatible Silicon-On-Insulator platform.* Optics Express, 18:18278–18283, 2010.

[4] D. Vermeulen, K. Van Acoleyen, S. Ghosh, S. Selvaraja, W. A. D. De Cort, N. A. Yebo, E. Hallynck, K. De Vos, P. P. P. Debackere, P. Dumon, W. Bogaerts, G. Roelkens, D. Van Thourhout, and R. Baets. *Efficient Tapering to the Fundamental Quasi-TM Mode in Asymmetrical Waveguides.* Presented at the European Conference on Integrated Optics 2010 (ECIO), page WeP16, 2010.

[5] H. Desmet, K. Neyts, and R. Baets. *Modeling nematic liquid crystals in the neigborhood of edges.* Journal of Applied Physics, 98:123517, 2005.

[6] P. R. Gray, P. J. Hurst, S. H. Lewis, and R. G. Meyer. *Analysis and Design of Analog Integrated Circuits (Fifth ed.).* Wiley, 2009.

[7] I. Kiyat, A. Aydinli, and N. Dagli. *Low-power thermooptical tuning of soi resonator switch.* Photonics Technology Letters, 18:364–366, 2006.

[8] P. Dong, W. Qian, H. Liang, R. Shafiiha, D. Feng, G. Li, J. Cunningham, A. Krishnamoorthy, and M. Asghari. *Thermally tunable silicon racetrack resonators with ultralow tuning power.* Optics Express, 18:20298–20304, 2010.

[9] J. Teng. *Fabrication of PSQ-L polymer photonic devices.* PhD. Thesis, 2010.

[10] J. Li, S. Gauza, and S. T. Wu. *High temperature-gradient refractive index liquid crystals.* Optics Express, 12:2002–2010, 2004.

5

Simulating LC-clad waveguides

5.1 Introduction

Simulations are very useful to gain insight in the working principles of physical experiments. For our work, this is no different. In this chapter, we give an overview of the simulations performed. In the first section, we briefly discuss the different tools that are used. The next sections each deal with an important parameter. Each of these parameters has a considerable influence on the outcome of the simulations. We focus on anchoring strength, cell thickness and waveguide width.

5.2 Simulation tools

Complete modeling of optical waveguides with a liquid crystal overlay in the presence of an electric field is no trivial matter. When we strive for an accurate model we need to calculate both the orientation of the director in the cladding layer and use this information when modeling the waveguide optically. These two calculation steps have to be combined as a small change in the orientation will induce a change in the optical properties. The modeling of the liquid crystal orientation requires several nonlinear equations to be solved at the same time. In a complex geometry this can be a difficult problem. The optical modeling of the liquid crystal is also quite challenging because of the optical anisotropy and the non-uniformity. The dielectric tensor $\bar{\bar{\epsilon}}$ can have up to six non-zero elements in the most general case. Most solvers make some kind of approximation to handle this, either in the anisotropy or in dimensionality [1–3]. For example, there are numerous solvers proposed in the past allowing only transverse anisotropy [4–8]. Longitudinal (in the propagation direction of the light) anisotropy is not allowed. In this work we have used the combination of a director calculation with a full vectorial mode solver allowing full anisotropy of the dielectric tensor. Next is a description of these different tools we used or developed to tackle the simulation problem as accurate and complete as possible. We explain how we use them to simulate optical waveguides with a cladding layer of LC.

5.2.1 Director calculation

The calculation of the director orientation was developed at University College London by Richard James. It is based on the minimization of the Landau-de Gennes free energy functional [9]. The model is implemented in a finite-element scheme. The order parameter of the liquid crystal can be variable which allows for the calculation of rapid variations of the order parameter, like in disclinations [10]. This tool is able to handle liquid crystal layers in the neighbourhood of small and complex geometries like our optical waveguides. As we work in a finite element scheme, it is necessary to define a mesh. This is a network of elements that divides the calculation space into a number of domains. In this work, the geometry is defined in 2D and the space is discretized in triangular elements. The generation of a mesh is an important step in the calculation of the problem. The number of elements determine the accuracy of the results but of course also the calculation time. Therefore, we make sure that there are enough elements close to the waveguide and less elements where there is less accuracy needed to reduce the calculation time. The mesh is generated using GiD, a commercially available program [11]. In Figure 5.1 we provide an example of a generated mesh used for the calculation of the director. Different parts of the mesh have additional information about the geometry. We can assign anchoring strenghts to regions with *FixLC* labels. For the different dielectrics, we can provide the dielectric constants and the optical refractive indices. For the Si waveguide, conductivity is assumed. Lastly, we can assign a voltage to the electrodes and calculate the resulting director orientation throughout the LC layer. Visualized examples of the results are shown in Figure 5.2 for a top bottom configuration and in Figure 5.3 for in plane switching. It can be clearly seen that the director undergoes a reorientation when there is a voltage applied to the electrodes. The results of the director calculation are directly imported into the mode solver. This ensures an accurate optical analysis of the LC-clad waveguides.

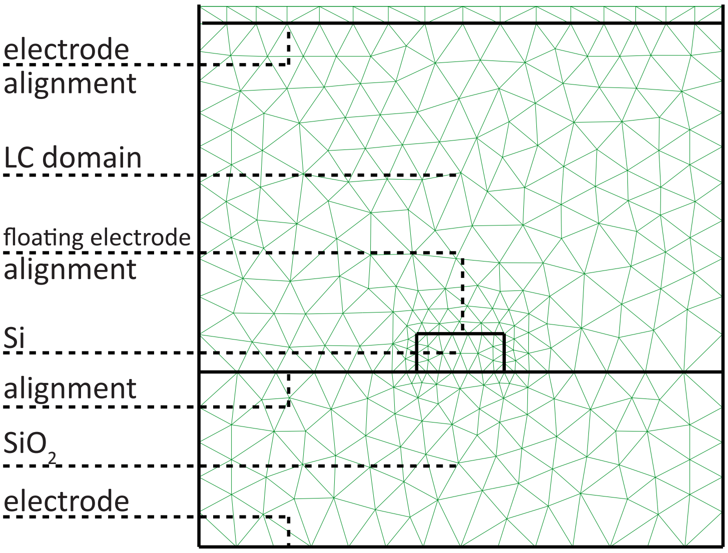

Figure 5.1: Mesh generated with the GiD program. The assigned materials are indicated.

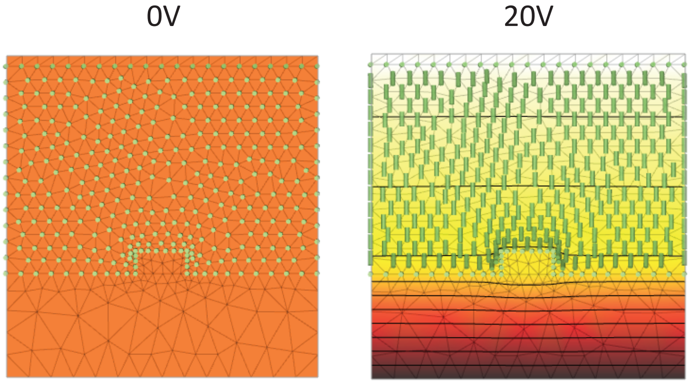

Figure 5.2: Simulated director orientation in a waveguide cladding layer for 0V and 20V. The electrodes are in a top-bottom configuration.

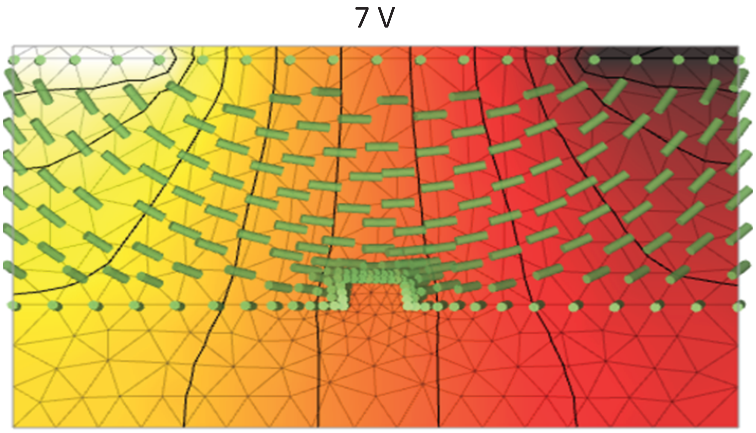

Figure 5.3: Simulated director orientation in a waveguide cladding layer for 7V. The electrodes are in an in-plane switching configuration.

5.2.2 Modesolver

The modesolver used in this work to analyse the waveguides optically was developed in a collaboration with University College London. It is capable of handling fully anisotropic problems [12]. The calculation is based on the solution of the variational form of the curl-curl equation of the electric field, implemented with higher-order edge elements. The Helmholz equation for the electric field is solved

$$\nabla \times \left(\frac{1}{\mu_r} \nabla \times \bar{E} \right) - k_0^2 \bar{\bar{\epsilon}}.\bar{E} = 0 \quad in\ \Omega \tag{5.1}$$

with the boundary condition

$$\bar{n} \times \bar{E} = 0 \quad on\ \delta\Omega \tag{5.2}$$

representing a perfect conductor. This corresponds to a variational problem [13]:

$$\begin{cases} \delta F(\bar{E}) = 0 \\ \bar{n} \times \bar{E} = 0 \quad on\ \delta\Omega \end{cases} \tag{5.3}$$

where

$$F(\bar{E}) = \frac{1}{2} \int \int_{\Omega} \left[\frac{1}{\mu_r} (\nabla \times \bar{E}).(\nabla \times \bar{E})^* - k_0^2 \bar{E}.\bar{\bar{\epsilon}}.\bar{E}^* \right]. \tag{5.4}$$

We look for modes propagating along the z direction

$$\bar{E}(x, y, z) = \bar{E}(x, y) e^{-jk_z z} \tag{5.5}$$

so $F(\bar{E})$ can be rewritten as

$$F(\bar{E}) = \frac{1}{2}\int\int_{\Omega}\left[\frac{1}{\mu_r}(\nabla_t \times \bar{E})\cdot(\nabla_t \times \bar{E})^* - k_0^2\bar{E}\cdot\bar{\bar{\epsilon}}\cdot\bar{E}^* \right. \\ \left. + \frac{1}{\mu_r}(\nabla_t E_z + jk_z\bar{E}_t)\cdot(\nabla_t E_z + jk_z\bar{E}_t)^*\right] d\Omega, \quad (5.6)$$

where ∇_t is the nabla operator containing only $\delta/\delta x$ and $\delta/\delta y$. The field is also split up into the transverse ($\bar{E}_t$) and the longitudinal (E_z) component. When we substitute $\bar{e}_t = k_z\bar{E}_t$ and $e_z = -jE_z$ and multiply by k_0^2, F can be written as

$$F = \frac{1}{2}\int\int_{\Omega}\left[\frac{1}{\mu_r}(\nabla_t \times \bar{e}_t)\cdot(\nabla_t \times \bar{e}_t)^* - k_0^2\bar{e}_t\cdot\bar{\bar{\epsilon}}\cdot\bar{e}_t^* \right. \\ + \frac{k_z^2}{\mu_r}\left(\nabla_t e_z\cdot\nabla_t e_z^* + \bar{e}_t\cdot\nabla_t e_z^* + \nabla_t e_z\cdot\bar{e}_t^* + \bar{e}_t\cdot\bar{e}_t^*\right) \\ \left. + jk_0^2k_z(\bar{e}_t\cdot\bar{\epsilon}_{tz}e_z^* - e_z\bar{\epsilon}_{zt}\cdot\bar{e}_t^*) - k_0^2k_z^2e_z\epsilon_{zz}e_z\right] d\Omega. \quad (5.7)$$

As shown before (Figure 5.1), the geometry is divided into triangular mesh elements while the fields are discretized according to $\bar{e}_t^e = \sum_i \bar{N}_i^e e_{ti}^e$ and $e_z^e = \sum_i L_i^e e_{zi}^e$, where $\bar{N}_i^e$ and L_i^e are the local shape functions [14]. With the Rayleigh-Ritz procedure [13] we obtain an eigenvalue system from which the propagation constant k_z can be derived.

$$\begin{bmatrix} A_{tt} & 0 \\ 0 & 0 \end{bmatrix}\begin{bmatrix} e_t \\ e_z \end{bmatrix} = -k_z^2\begin{bmatrix} B_{tt} & B_{tz} \\ B_{zt} & B_{zz} \end{bmatrix}\begin{bmatrix} e_t \\ e_z \end{bmatrix} - k_z\begin{bmatrix} 0 & jC_{tz} \\ -jC_{zt} & 0 \end{bmatrix}\begin{bmatrix} e_t \\ e_z \end{bmatrix}, \quad (5.8)$$

where

$$[A_{tt}^e] = \int\int\left[\frac{1}{\mu_r}\{\nabla_t \times \bar{N}^e\}\cdot\{\nabla_t \times \bar{N}^e\}^T - k_0^2\{\bar{N}^e\}\cdot\bar{\bar{\epsilon}}_{tt}\cdot\{\bar{N}^e\}^T\right] d\Omega \quad (5.9)$$

$$[B_{tt}^e] = \int\int\left[\frac{1}{\mu_r}\{\bar{N}^e\}\cdot\{\bar{N}^e\}^T\right] d\Omega \quad (5.10)$$

$$[B_{tz}^e] = [B_{zt}^e]^T = \int\int\left[\frac{1}{\mu_r}\{\bar{N}^e\}\cdot\{\nabla_t L^e\}^T\right] d\Omega \quad (5.11)$$

$$[B_{zz}^e] = \int\int\left[\frac{1}{\mu_r}\{\nabla_t L^e\}\cdot\{\nabla_t L^e\}^T - k_0^2\epsilon_{zz}\{L^e\}\{L^e\}^T\right] d\Omega \quad (5.12)$$

$$[C_{tz}^e] = [C_{zt}^e]^T = k_0^2\int\int\left[\{\bar{N}^e\}\cdot\bar{\epsilon}_{tz}\{L^e\}^T\right] d\Omega. \quad (5.13)$$

Equation 5.8 is a quadratic eigenvalue problem [15] that can be solved numerically. Reference [12] contains more details and calculation examples for the mode solver.

	V$_L$	V$_H$
E$_x$	$\epsilon_\perp$	$\epsilon_\perp$
E$_y$	$\epsilon_\perp$	$\epsilon_{||}$
E$_z$	$\epsilon_{||}$	$\epsilon_\perp$

Table 5.1: Dielectric constants seen by the E-field components at low and high voltage levels in a top-bottom electrode configuration.

5.3 General tuning mechanisms

The intuitive understanding of the tuning mechanism has been briefly discussed in chapter 4 when the experimental results were described. We repeat it here in a bit more detail as it will help to increase the readability of the rest of the chapter where we will go through the various simulations that we performed.

5.3.1 Top-bottom tuning

There is a direct relation between the change in effective index and the change in resonance wavelength. This change in effective index is dependent on the electric fields of the light mode and the dielectric constants of the core and the cladding layers. Table 5.1 shows an overview of the dielectric constants seen by the different components of the electric field (E$_x$, E$_y$, E$_z$ in agreement with Figure 2.3) for low and high voltage levels in a top-bottom electrode configuration. In section 2.3.2 it was explained that a quasi TE mode in photonic wires has an important E-field component in the propagation direction (E$_z$), located at the sidewalls of the waveguide. In the tuning scheme discussed in this section the dielectric constant along the propagation direction goes down with increasing voltages. It can be seen in Figure 5.2 that at low voltage levels the LC director is oriented along the propagation direction while it reorients perpendicular to it at higher voltages. In the transverse (E$_x$) direction the dielectric constant remains stable for all voltages. While the dielectric constant in the normal direction rises it has almost no influence on the effective index as the electric field (E$_y$) is very weak. From these considerations we expect the effective index to decrease with increasing voltages beyond the threshold voltage. From the change in effective index, the change in resonance wavelength of a ring resonator can be calculated as

$$\frac{\lambda_2 - \lambda_1}{\lambda_1} = \frac{n_{eff2} - n_{eff1}}{n_g}, \tag{5.14}$$

$$\lambda_2 = \lambda_1 \cdot \frac{n_{eff2} - n_{eff1}}{n_g} + \lambda_1, \tag{5.15}$$

	V_L	V_H
E_x	$\epsilon_\perp$	$\epsilon_{\|\|}$
E_y	$\epsilon_\perp$	$\epsilon_\perp$
E_z	$\epsilon_{\|\|}$	$\epsilon_\perp$

Table 5.2: Dielectric constants seen by the E-field components at low and high voltage levels in an in-plane switching electrode configuration.

with n_g the group index of the mode. The resonance wavelength changes proportionally to n_{eff}. For the quasi TM mode the most important contribution to n_{eff} is made by E_y. This component sees an increasing dielectric constant and n_{eff} will therefore increase. We expect a shift of the resonance wavelength towards longer wavelengths.

5.3.2 In-plane switching

In an in-plane switching electrode configuration, the director is forced to twist in the plane of the chip. The effect on the dielectric constants seen by the different electric field components can be seen in table 5.2 Two effects will counteract each other as the Z-component will cause a decrease in n_{eff} while the X-component will do the opposite. However, the X-component is the strongest of the two components and will weigh more heavily on the effective index. Moreover, the director at the sidewalls suffers from anchoring both from the sidewalls and the SiO_2 surface supporting the waveguide. From this we can expect to see a net increase of the effective index and the resonance wavelength of the ring resonators.

5.4 Anchoring strength

It is clear that the anchoring strength on the surface of the chip plays an important role in the ultimate behaviour of the cell. It determines how easily the director on the surface can be reoriented. In the presence of an electric field, the reorientation of the director starts in the bulk of the LC. Here, the influence of surface anchoring is minimal. For higher voltages, the reorientation spreads towards the surfaces in contact with the LC. As this region near the surface has the biggest influence on the effective index of the mode, the influence of the anchoring strength can not go unexamined. As explained in chapter 1, the anchoring strength is a measure for the influence of the surface on the orientation of the LC director. Hard anchoring does not allow deviations from the orientation determined by the surface conditions. The twist and tilt will remain the same

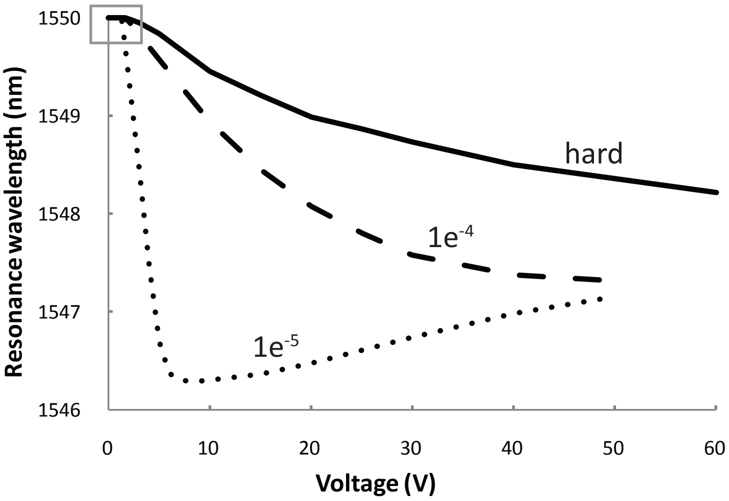

Figure 5.4: Simulated tuning curves for the TE mode for hard and weak anchoring. The waveguides are 500 nm wide and 220 nm high. A close-up of the grey box is given in Figure 5.5.

in any condition or under any external influence. Weak anchoring does allow some deviations [16], associated with a certain surface energy (see chapter 1). We make a distinction between anchoring energy for the tilt (a_t), when the director reorients out of the plane of the chip and anchoring energy for the twist (a_p), a rotational reorientation of the director in the plane. From our experience we know that the director on an untreated surface can show a planar degeneracy, meaning that while the molecules are to some extent anchored parallel to the surface, their orientation in the plane is not strictly fixed.

5.4.1 Top-bottom tuning

In Figure 5.4 we show the tuning curves for hard and weak anchoring of a ring guiding the TE mode. We have plotted the weak anchoring curves for surface energies $a_t = a_p = 1 \cdot 10^{-4}\,\mathrm{J/m^2}$ and $1 \cdot 10^{-5}\,\mathrm{J/m^2}$. The LC cladding layer is $2\,\mu$m thick and the waveguide measures 220 nm high and 500 nm wide. The three curves differ significantly from each other in tuning range and threshold voltage. The tuning range remains limited in the case of hard anchoring as no reorientation of the molecules *on* the surface is possible. The tuning itself occurs rather gradually as the anchoring allows reorientation *near* the surface only at higher voltages. For weaker anchoring, it is clear that the tuning curve is steeper at low voltages. Depending on the anchoring strength, a tuning range of around 1.5 to 2.5 nm is found. When the anchoring is very weak (e.g. surface energy is

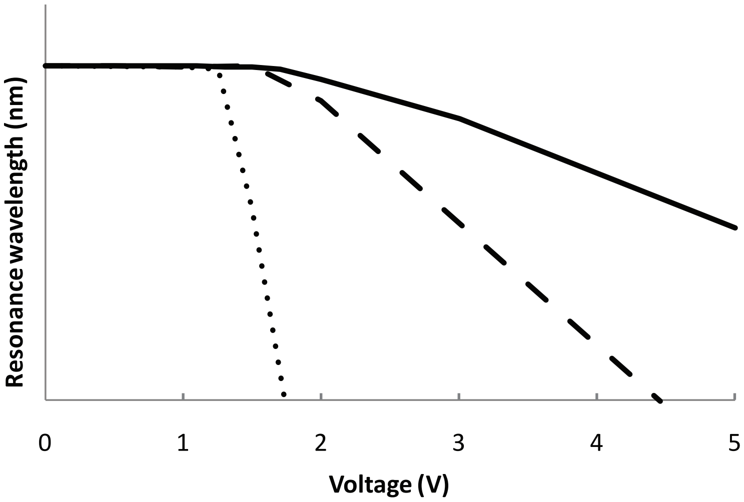

Figure 5.5: Gray box in Figure 5.4: close-up of the threshold voltages of the different tuning curves.

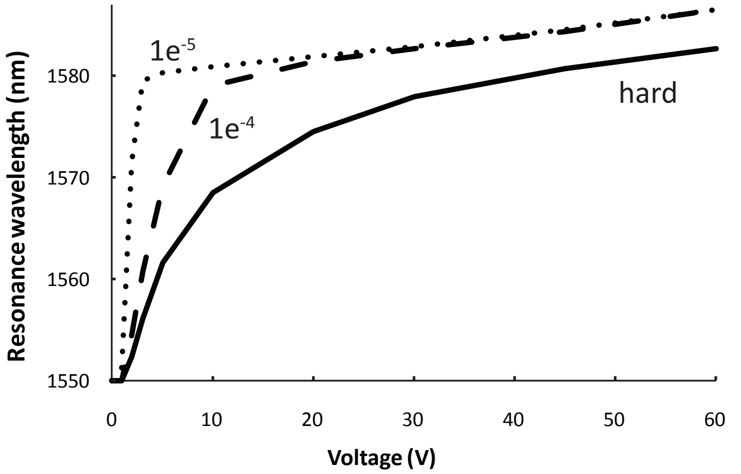

Figure 5.6: Simulated tuning curves for the TM mode for hard and weak anchoring. The waveguides are 500 nm wide and 220 nm high.

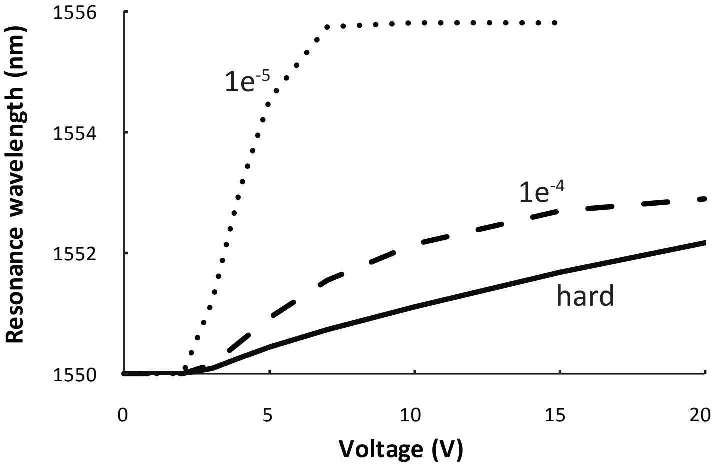

Figure 5.7: Simulated top-bottom tuning curves for the TE mode for hard and weak anchoring in an IPS configuration. The waveguides are 450 nm wide and 220 nm high.

$1 \cdot 10^{-5}\,\mathrm{J/m^2}$), a curious increase of the resonance wavelength is seen after the initial drop. The Si waveguide is a semiconductor and will therefore act as a floating electrode between the top and bottom electrodes. It will slightly bend the fieldlines and reorient the director a bit in the XY-plane. This will cause an increase of the dielectric constant along the X-axis. Due to the large transverse electric field component, this is translated in an increase of the effective index and the resonance wavelength. The threshold value shifts towards lower voltages for weaker anchoring strengths. The bulk of the LC starts to reorient at the voltage required for the Freedericksz transition. The reorientation is slowed down near the surfaces depending on the anchoring strength. For weaker anchoring the reorientation near the surface will start at lower voltages. When we calculate the TM mode instead of the TE mode we find a tuning range of 30 nm to 35 nm (Figure 5.6). As was predicted, the resonance wavelength shifts gradually towards longer wavelengths as the director aligns vertical to the waveguide. For weaker anchoring strengths the resonance shifts much faster compared to hard anchoring.

5.4.2 In-plane switching

In an IPS configuration, the anchoring strength plays an equally important role as in a top-bottom configuration. It will determine how easily the director on the surface can be twisted to align along the electric fieldlines. In Figure 5.7

we show the curves for hard and weak ($a_t = a_p = 1 \cdot 10^{-4}\,\mathrm{J/m^2}$ and $1 \cdot 10^{-5}\,\mathrm{J/m^2}$) anchoring. The waveguides are 450 nm wide and 220 nm high. The electrodes are spaced 3 μm apart. We can make more or less the same observations as before. The tuning range for lower anchoring strengths is higher as reorientation of the director at the surface is allowed to a larger degree. The threshold for tuning is lower as well. There is a noticeable difference however with the top-bottom simulation results as the voltage levels in general are much lower with IPS. This is easily explained when we consider that there will be no unwanted voltage drop in the IPS configuration as was the case in top-bottom tuning. The IPS cell is in fact as "thick" as the spacing between the electrode fingers, in this case 3 μm.

5.5 Cell thickness

A cell consisting of a chip, a liquid crystal cladding and an electrode on top acts essentially as a capacitor. With increasing thickness of the LC layer, the capacitance will decrease together with the strength of the electric field. We expect the reorientation to be weaker for thicker cells at the same voltage level.

5.5.1 Top-bottom tuning

We simulate the tuning curves for ring resonators with an increasingly thick cladding of LC (Figure 5.8). The waveguide itself measures 220 nm high and 450 nm wide. We implemented strong anchoring of the director on the surface. We see that the tuning occurs the fastest for a liquid crystal cladding of 1 μm thick. The simulations show that the tuning indeed gets weaker for thicknesses of 2 μm, 5 μm and 10 μm respectively at the same voltage levels. The same holds for the TM mode (Figure 5.9). As the cell gets thicker the electric field weakens and the tuning will occur at higher voltages. Although spacers should provide a well-defined thickness, it may be not so easy to achieve a manually assembled cell with a uniform thickness. These simulations show that careful control of the thickness is required for consistent results.

5.5.2 In-plane switching: gap between electrodes

In an in-plane switching configuration, the gap between the electrode fingers will have an influence on the magnitude of the tuning at a certain voltage. It is equivalent to the cell thickness examined above in a top-bottom electrode configuration. We simulate a cell with a 2 μm liquid crystal layer. The electrode fingers are spaced 3 μm and 5 μm respectively. Strong anchoring is implemented. Figure 5.10 shows the difference in behaviour. While the general shape of the

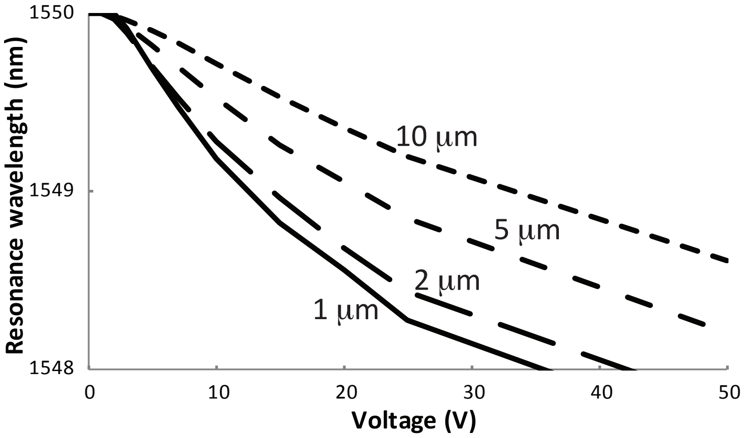

Figure 5.8: Tuning curves simulated for top-bottom tuned TE waveguides with LC cladding layers of 1 μm, 2 μm, 5 μm and 10 μm thick. The waveguides are 450 nm wide and 220 nm high.

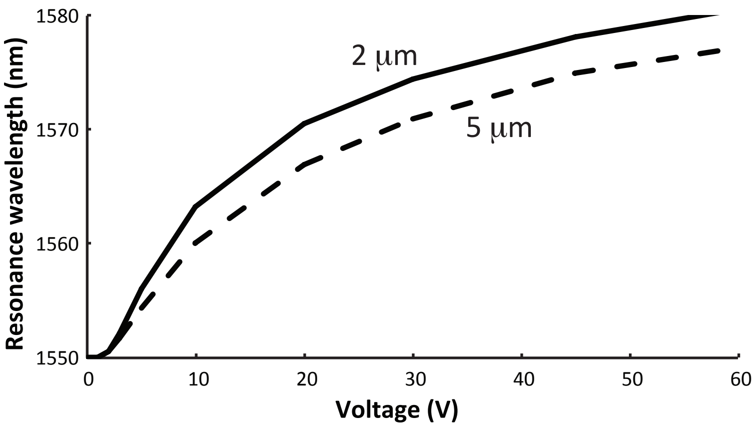

Figure 5.9: Tuning curves simulated for TM waveguides with LC cladding layers of 2 μm and 5 μm thick. The waveguides are 450 nm wide and 220 nm high.

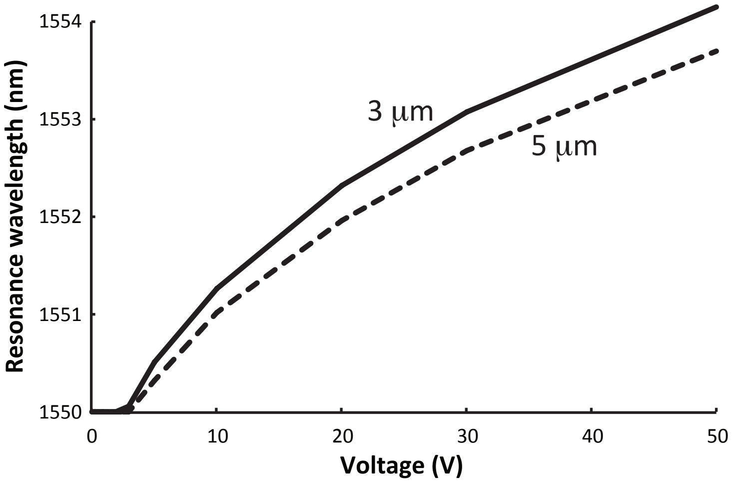

Figure 5.10: Tuning curves simulated for TE waveguides in an IPS cell. The electrode spacing is 3 μm and 5 μm. The waveguides are 500 nm wide and 220 nm high.

tuning curve is preserved, the tuning occurs at higher voltages when the spacing between the electrodes is enlarged.

5.6 Waveguide width

The height of the waveguides is determined by the SOI stack and is typically 220 nm. The Si top layer of a SOI wafer is extremely flat and any etching done to reduce the height of this layer will induce extra roughness and propagation losses. Therefore, it is very difficult to alter this parameter. The width of a waveguide, however, can be designed as small as the fabrication techniques allow. In a narrow waveguide, the light will be pushed out more in the cladding. The interaction with active cladding layers is therefore greater. This holds especially for the TE mode as it is located at the sidewalls of the waveguide. Here, we simulate waveguides with a height of 220 nm and a width of 350 nm, 400 nm, 450 nm and 500 nm respectively (Figure 5.11). The LC layer is 2 μm thick and the anchoring is strong. We can see that the tuning range increases for decreasing waveguide width. For standard photonic wires where the width is 450 nm or 500 nm, the tuning range remains limited to 1 to 2 nm. For significantly less wide waveguides (350 nm), this increases to about 4 nm. We calculate the fraction of the intensity in the core, the oxide and the LC cladding layer. From table 5.3 it follows indeed that more and more light gets pushed out into the cladding when

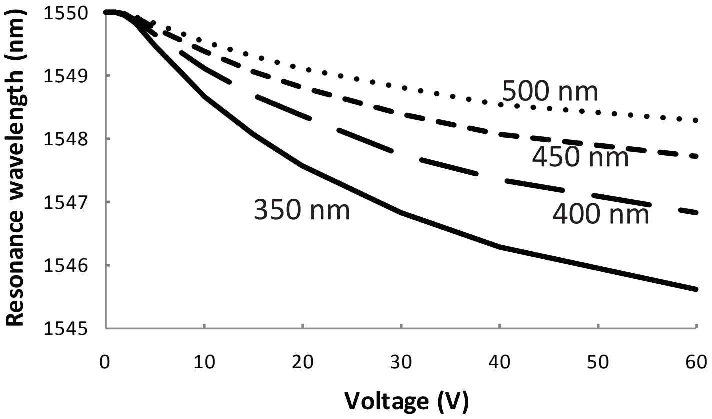

Figure 5.11: Top-bottom tuning curves simulated for TE resonators with waveguide widths of 350 nm, 400 nm, 450 nm and 500 nm.

	core	LC	oxide
500 nm	0.708	0.169	0.123
450 nm	0.696	0.171	0.133
400 nm	0.649	0.21	0.141
350 nm	0.560	0.285	0.155

Table 5.3: Relative intensity of the mode in the different regions of the waveguide cross section (the Si waveguide core, the LC cladding and the insulating oxide). There is no electric field applied.

the waveguide width decreases.

The evanescent tails of the TM mode are mostly located at the top of the waveguide. Therefore, the influence of the waveguide width on the resonance wavelength will be small (Figure 5.12). The tuning range of the 500 nm wide waveguide guiding the TE mode is about 25% smaller than the tuning range of the 450 nm wide waveguide. When the TM mode travels in these waveguides the difference is only about 12%. While this is still a substantial change, the effect of a changing waveguide width is only half as big as for TE waveguides.

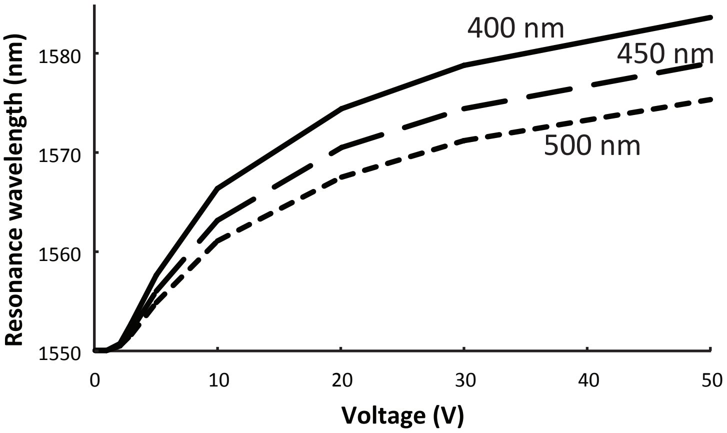

Figure 5.12: Top-bottom tuning curves simulated for TM resonators with waveguide widths of 400 nm, 450 nm and 500 nm.

5.7 Match between simulations and experiments

It is clear that there are quite some parameters that influence the outcome of the simulations. There is the thickness of the cell, the width and height of the waveguides but also the anchoring on the surface. In this chapter we have studied the effect of varying one parameter while keeping the others fixed. We have gained insight in the tuning mechanism doing this but we have yet to verify how close the simulations can match the experiments discussed in chapter 4.

5.7.1 Top-bottom tuning

The rings we used in the experiments are formed by waveguides with a width of 450 nm and a height of 220 nm. The thickness of the LC layer is controlled by spacers with a diameter of 6 μm. We consider these parameters known and fixed. Therefore, what remains unknown is the anchoring strength of the chip surface. We have performed a large number of simulations with different anchoring strengths in order to get as close as possible to the experimental results. The best agreement is achieved with a very low value for a_p and a moderate value for a_t. This means that the director is allowed to rotate freely in the plane of the surface. While the tilt of the director remains anchored, some vertical reorientation on the surface is also allowed. The best fit values are $a_p = 5.10^{-6}$ and $a_t = 5.10^{-4}$. There is a particulary good agreement between simulation and experiment in the TM tuning curve. The simulated tuning range, saturation and threshold value all correspond quite well to the experimentally found values (Figure 5.13). The simulated TE tuning curve differs somewhat from the experiments (Figure 5.14).

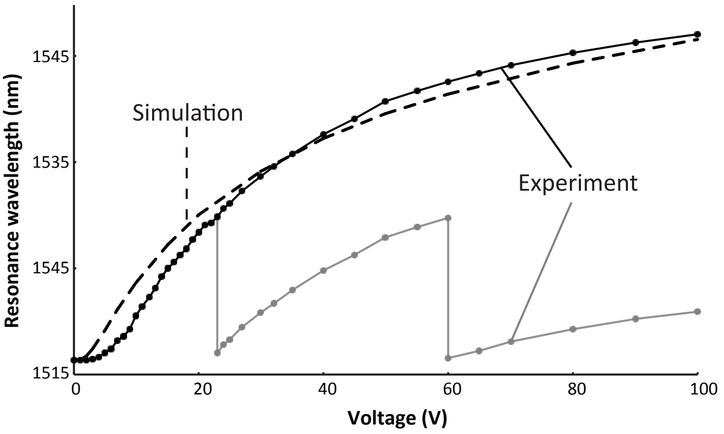

Figure 5.13: A comparison between the experimental and simulated tuning curve for ring resonators guiding TM light.

The tuning range is a bit smaller (3.5 nm compared to the experimental range of 4.5 nm). We have found it impossible to improve on the simulated range by lowering the anchoring strength even further. Therefore, we suspect that it is a slightly deviant waveguide profile (width, slanted sidewalls) that causes the difference.

5.7.2 In-plane switching

There are a few things we should take into account before starting to compare the simulation results of the in-plane switching cells with the experiments.

- **Electrode position.** As we said in chapters 3 and 4, all the cells are assembled manually. This poses serious problems regarding the alignment of the electrodes to the rings. To benefit from an optimal director reorientation, the ring has to sit right between two electrode fingers. This is nearly impossible to do manually and we can expect that all rings suffer from a less than perfect alignment. This will reduce the theoretical tuning range.

- **Non-uniform behaviour.** The circular geometry of the ring resonators leads to a non-uniform director orientation distribution along the ring waveguide. The parts of the ring that are more or less parallel to the electrode fingers and the initial rubbing direction, will see a reorientation when the director aligns to the field lines of the external field. The parts of the ring that are perpendicular to the electrodes, will see no reorientation at all as the director was already twisted there to begin with. This adds up to

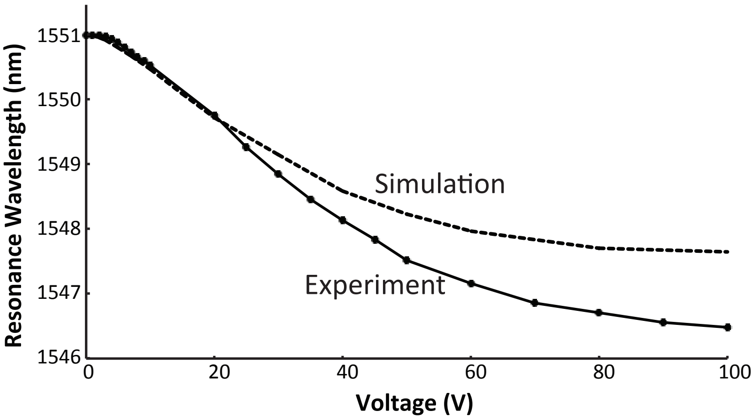

Figure 5.14: A comparison between the experimental and simulated tuning curve for ring resonators guiding TE light. The electrodes are in a top-bottom configuration.

a continuously changing cladding as seen by the waveguide mode. This again reduces the theoretical tuning range as parts of the ring simply won't tune at all.

- **Disclinations.** The rings used in the experiments are small in order to fit more or less between two electrode fingers. The remark made in paragraph 4.3.2.2 about the disclinations is especially important here. The disclinations will influence the behaviour of the cladding in an unpredictable way. With smaller rings this effect becomes more prominent.

The rings used in the IPS experiments have a width of 500 nm and a height of 220 nm. The spacing between the electrodes is 10 μm. Although the general shape of the curve resembles that of the experimentally found tuning curve, the agreement is not nearly as good as in the top-bottom tuning experiments. Considering the comments above helps us to understand the large difference in tuning behaviour between the simulations and the experiments (Figure 5.15).

5.8 Conclusions

In this chapter, we have introduced the modelling tools we have used to simulate the behaviour of SOI waveguides with a liquid crystal cladding. There are 3 parameters that have a major influence on the outcome: the anchoring strength on the chip's surface, the width of the waveguide and the thickness of the LC cell. We have shown that very weak anchoring, combined with very narrow

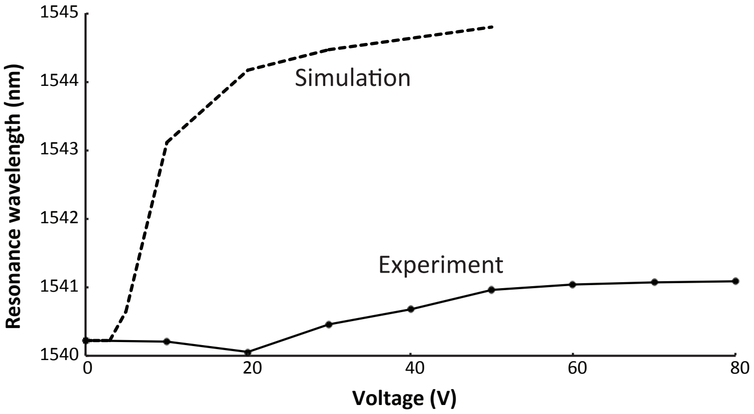

Figure 5.15: A comparison between the experimental and simulated tuning curve for ring resonators guiding TE light. The electrodes are in an in-plane switching configuration.

waveguides in a thin cell will yield the best results for TE and TM light, both in a top-bottom electrode configuration and an in-plane switching cell. Of course we can not always choose these parameters freely. The anchoring strength is a property of the surface and every layer we would add to lower the anchoring will be detrimental to the tuning range. The waveguide width is a parameter we can control and here lies a possibility for further improvement. However, a more narrow waveguide will be more lossy and will eventually yield lower q-factors of the ring resonators. A thin LC cell is challenging to make manually, but it can be done. However, a cell that is too thin (below 2 μm) can lead to absorption of the light in the ITO layer on the glass. Ultimately, once all simulation parameters are chosen well, we have found a good agreement with the experiments discussed in the previous chapter.

References

[1] A. Fratalocchi, R. Asquini, and G. Assanto. *Integrated electro-optic switch in liquid crystals.* Optics Express, 13:32–36, 2005.

[2] R. Asquini and A. d'Alessandro. *Bpm analysis of an integrated optical switch using polymeric optical waveguides and ssflc at 1.55 μm.* Molecular Crystals and Liquid Crystals, 375:243–247, 2002.

[3] G. N. Ntogari, D. Tsipouridou, and E. Kriezis. *A numerical study of optical switches and modulators based on ferroelectric liquid-crystals.* Journal of Optics A: Pure and Applied Optics, 7:82–87, 2005.

[4] Y. Lu and F. A. Fernandez. *An efficient finite element solution of inhomogeneous anisotropic and lossy dielectric waveguides.* IEEE Transactions on Microwave Theory and Techniques, 41:1215–1223, 1993.

[5] F. Bertazzi, O. Peverini, M. Goano, G. Ghione, R. Orta, and R. Tascone. *A fast reduced-order model for the full-wave fem analysis of lossy inhomogeneous anisotropic waveguides.* IEEE Transactions on Microwave Theory and Techniques, 50:2108–2114, 2002.

[6] P. Savi, I. Gheorma, and R. Graglia. *Full-wave high-order FEM model for lossy anisotropic waveguides.* IEEE Transactions on Microwave Theory and Techniques, 50:495–500, 2002.

[7] V. Schulz. *Adjoint high-order vectorial finite elements for nonsymmetric transversally anisotropic waveguides.* IEEE Transactions on Microwave Theory and Techniques, 51:1086–1095, 2003.

[8] A. Fallahkhair, S. Li, and T. Murphy. *Vector finite difference modesolver for anisotropic dielectric waveguides.* Journal of Lightwave Technology, 26:1423–1431, 2008.

[9] P. G. de Gennes and J. Prost. *The Physics of Liquid Crystals.* Oxford University Press, 1995.

[10] R. James, E. Willman, F. A. Fernández, and S. E. Day. *Finite-element modeling of liquid-crystal hydrodynamics with a variable degree of order.* IEEE Transactions on Electron Devices, 53:1575–1582, 2006.

[11] CIMNE International Center for Numerical Methods in Engineering. *GiD, The Personal Pre and Post Processor.* `http://gid.cimne.upc.es/`.

[12] J. Beeckman, R. James, F. A. Fernandez, W. De Cort, P. J. M. Vanbrabant, and K. Neyts. *Calculation of Fully Anisotropic Liquid Crystal Waveguide Modes.* Journal of Lightwave Technology, 27:3812–3819, 2009.

[13] J. Jin. *The Finite Element Method in Electromagnetics (Second ed.).* Wiley, 2002.

[14] M. Koshiba and Y. Tsuji. *Curvilinear hybrid edge/nodal elements with triangular shape for guided-wave problems.* Journal of Lightwave Technology, 18:737–743, 2000.

[15] F. Tisseur and K. Meerbergen. *The quadratic eigenvalue problem.* SIAM Review, 43:235–286, 2001.

[16] Chandrasekhar. *Liquid crystals, 2nd edition.* Cambridge University press, 1992.

6

Trimming ring resonators with polymerizable LC

In the previous chapters we have discussed the ins and outs of the tuning of ring resonators with a cladding layer of LC. In this chapter we will describe an alternative experiment, where we fix the position of the resonance of the ring after the tuning process. To achieve this, we use polymerizable LC in the form of a mixture of LC and a polymerizable component. After we have introduced polymerizable LC, we will describe the properties of the mixtures and the actual experiments. The majority of this work was carried out in the framework of the master thesis of Ir. Sophie Lambert. Her dissertation (in Dutch) should be consulted for more details [1].

6.1 Introduction

6.1.1 Trimming of SOI ring resonators

One of the strongest arguments for using SOI for photonics is the possibility for mass fabrication offered in the CMOS fabs [2, 3]. Deep UV lithography using 248 nm or 193 nm sources has become a mature technology and can produce high volumes at relatively low cost. It has to be noted, however, that the precision requirements for CMOS and photonics are not the same. A variation of 10% in the critical dimensions is acceptable for most CMOS processes but not at all for photonics. A variation of only 1 nm in the width of the waveguide of a ring resonator causes a resonance shift of about 1 nm [2]. In general, the resonance of fabricated ring resonators can differ more than 1 nm from the designed value. This is of course unacceptable for many applications. To overcome the fabrication imperfections, the ring resonators have to be trimmed or tuned to the exact resonance wavelength. Active thermal tuning is the most applied tuning technique. It involves the fabrication of metallic heaters close to the ring resonators [4–6]. This heating process becomes very demanding in terms of power and design effort for complicated structures with many resonators. Carrier injection or depletion [7] is also an option but requires doping of the silicon. The LC overlay methods discussed in the previous chapters can also be used to compensate for the fabrication inaccuracies. Although these methods offer flexibility and reversibility, they require continuous supply of voltage and are therefore not very attractive for use on a large scale. Trimming techniques can be used to make small non-reversible modifications to photonic ring resonators and their resonances. In his PhD. dissertation, Jonathan Schrauwen describes in detail the use of focussed ion beam etching or electron beam induced compaction as trimming methods [8]. In particular the use of electron beam induced compaction was successful. Here we propose an alternative method using polymerizable liquid crystal as an overlay. After tuning the resonance to the desired wavelength with one of the methods discussed in previous chapters, the orientation of the polymerizable LC can be fixed by illumination with UV light.

6.1.2 Polymerizable LC

In this part, we will first discuss photo-initiated polymerization after which we give an overview of the different kinds of LC polymers and give some application examples.

6.1.2.1 Photo-initiated polymerization

Since decades, light has been used as an initiator for polymerization. Especially in printing and coating industries this technique is widely applied [9]. We distinguish between two types of reactions:

- **Photopolymerization** is a condensation reaction where a chain molecule grows in steps. Each step requires the absorption of a photon to add a low molecular mass molecule to the chain [10].
- **Photo-initiation**, the method used in this work, is a process where the initiator absorbs photons and as a consequence decomposes into free radicals or reactive ions. These initiate the chain-growth [11]. As we use

this method in our work, we will focus on this reaction in the rest of the chapter.

A photopolymerizable material should be a mixture of different components. It must contain a polymerizable component, being a monomer, oligomer or polymer and an initiator. Acrylates are also often used as polymerizable components as they tend to grow fast into a polymer and are stable in a no-light condition. As we said before, the initiator is a molecule that absorbs energy in the form of photons (of the right wavelength) and decomposes into free radicals (homolytic dissociation).

$$I \xrightarrow{k_d} 2R\bullet, \tag{6.1}$$

where I stands for the initiator, R for the free radicals and k_d for the speed of the dissociation. The bullet denotes whether or not the molecule in question is reactive. A free radical can bond with a monomer M to form an initiated monomer. This process is called the *initiation*:

$$R\bullet + M \xrightarrow{k_i} M_1\bullet, \tag{6.2}$$

where M stands for monomer and k_i denotes the speed of the initiation. Chain-growth from this reactive monomer happens when other monomers attach to it. This is called *propagation*:

$$M_1\bullet + M \xrightarrow{k_p} M_2\bullet, \tag{6.3}$$

$$M_n\bullet + M \xrightarrow{k_p} M_{n+1}\bullet. \tag{6.4}$$

The chainreaction stops when two reactive chains bond. This process is called *termination*:

$$M_n\bullet + M_m\bullet \xrightarrow{k_{tc}} M_{n+m}, \tag{6.5}$$

$$M_n\bullet + M_m\bullet \xrightarrow{k_{td}} M_n + M_m, \tag{6.6}$$

with k_{tc} and k_{td} the speed of termination through combination and disproportion. How fast a certain material is polymerized depends on several factors: concentration of the monomer, intensity of the UV light, thickness of the layer that is illuminated and temperature of the mixture. The temperature dependency is a problem for our experiments as we don't want any polymerization before the material is illuminated. An inhibitor can be added to prevent polymerization in the absence of UV light [12].

6.1.2.2 LC polymers

LC polymers are polymers made up from LC monomers. The polymers consist of LC molecules that are linked with each other during polymerization and the

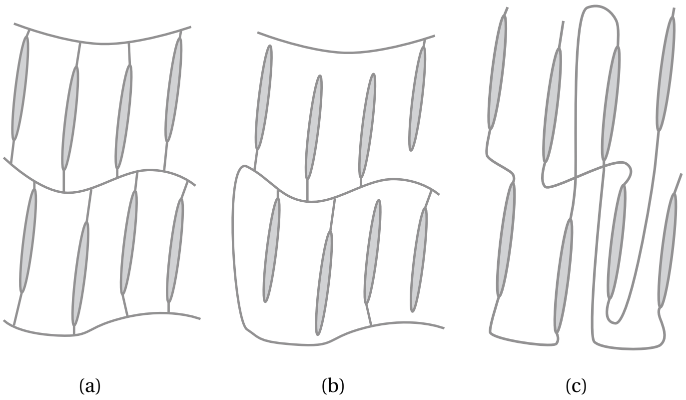
(a) (b) (c)

Figure 6.1: LC polymers organized in a network (a), a side-chain polymer (b), and a main-chain polymer (c)

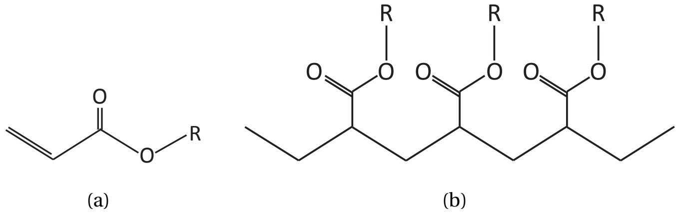

Figure 6.2: (a) Acrylate monomer, (b) acrylate polymer

resulting material will be anisotropic. The individual molecules can retain a certain degree of freedom after polymerization so that there can still be phase transition, but most often this is not the case [13]. They can be linked into an LC network, an LC side-chain polymer or an LC main-chain polymer (Figure 6.1). In an LC network, the molecules have little freedom as they are linked from both sides to the network. The two other types allow for more movement. In this work, we want to fix the material completely and we will use a complete LC network. LC acrylates will be used here. Figure 6.2 shows their structure, and that of the polymer they form when illuminated.

6.1.2.3 Applications

Polymerizable liquid crystals have been used in a large number of applications. As light can be used as an initiator, it is possible to use lithography techniques. This allows for very precise control of the polymerization. Below, we discuss some examples of polymerizable LC applications.

Polarizing beam splitters.
A layer of polymerizable LC is caught between two prisms. Light is split up by the first prism into two orthogonally polarized beams. The polarization of one of those beams is then rotated 90^o by the LC layer. The second prism puts the beams back together. Polarizing beam splitters are often used in projection [14].

Cholesteric polymer films with a large bandwidth.
Cholesteric LCs are arranged in layers where the molecules are twisted slightly with respect to the next layer. The result is a helix structure that reflects light that is circularly polarized with the same handedness. The reflected wavelength depends on the pitch of the helix. The pitch can be enlarged by mixing the cholesteric LC with a regular nematic LC [15]. Introducing a gradient in the helix greatly augments the reflection band of the cholesteric LC. A mixture of a mono-reactive nematic mesogen, a di-reactive chiral mesogen, a UV-absorbing colorant and an initiator sensitive to the wavelength absorbed by the colorant. During illumination, the colorant introduces a gradient of the UV intensity throughout the material. The di-reactive mesogen responds faster and at the top of the layer, a film with large concentration of chiral material forms. The nematic mesogen diffuses to the bottom of the layer where the resulting helix will have a larger pitch [15].

Mechanics.
When there are azo-groups present in the liquid crystalline material, rapid deformation of the molecules occurs under illumination. When a polymer film is created from this material, the whole film can deform when illuminated. This makes transition from light energy to mechanical movement possible [16].

6.2 Mixture properties

In this section, we introduce the materials we used and the mixtures we prepared. To evaluate the mixtures, we study it with a polarizing microscope and a spectrometer.

6.2.1 Materials

We prepare mixtures of polymerizable LCs, a regular nematic LC, an initiator and an inhibitor as discussed above. The exact materials are:

- RM23, a LC monomer, monoacrylate, available from Merck

component	mass percentage
RM23	13.2%
RM82	22.1%
RM257	53.0%
5CB	8.8%
irgacure	0.3%
TBHQ	2.6%

Table 6.1: Mass percentages of the different constituents of the mixture.

- RM82, a LC monomer, diacrylate, available from Merck
- RM257, a LC monomer, diacrylate, available from Merck
- 5CB, a nematic LC
- irgacure 819, the initiator
- tert-butylhydroquinone, the inhibitor

RM23, RM82 and RM257 are polymerizable LCs. They have a chemical structure resembling that of a regular nematic but with an acrylate-group attached that allows bonding with other molecules during polymerization. 5CB is the same nematic LC used in major parts of this PhD. Irgacure is a photoinitiator decomposing into free radicals upon UV illumination, thus initiating the chain-growth. Tert-butylhydroquinone (TBHQ) is the inhibitor that makes sure the reaction only starts with UV illumination. It is an antioxidant used as a preservative in food industry. The solvent used during the preparation is dichloromethane, which is evaporated afterwards. The mixture contains three LC components. The purpose is to increase the temperature range at which the mixture is in the nematic phase. In Figure 6.3 the principle is shown for a mixture of two components. T_{C1} and T_{C2} are the clearing temperatures and T_{m1} and T_{m2} the melting points. The clearing temperature of the mixture varies linearly as a function of the concentration of one of the constituents (LC_2 in the figure). The melting point however does not and for a well-chosen concentration, the nematic temperature range can be greatly increased (eutectic mixture). Eutectic mixtures often contain up to 15 components [17]. The exact composition of our mixture is shown in table 6.1.

6.2.2 Visual inspection

With a polarizing microscope, we evaluate the cells visually. They consist of two glass plates coated with ITO, glued together with UV-curable glue and spacers.

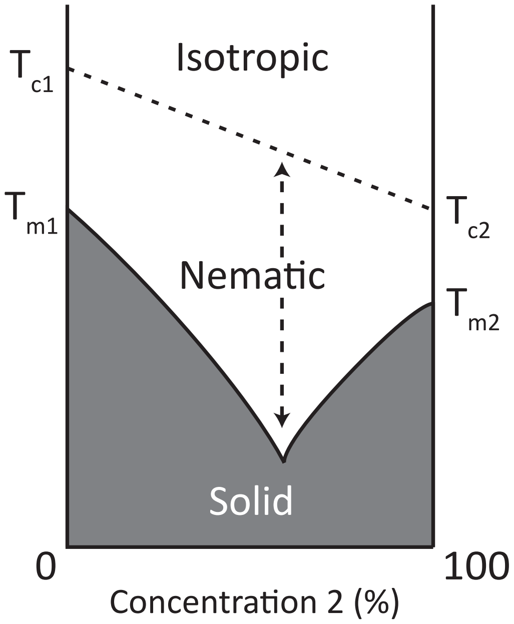

Figure 6.3: Phase diagram of a binary mixture.

The glass plates are coated with an alignment layer and rubbed to provide a uniform orientation of the director throughout the cell. When a voltage is applied (Figure 6.4) the cell changes colour. The electric field is too weak to reorient the molecules vertically, but the director now makes an angle with respect to the glass plates. This causes a change in the retardation (see chapter 1) of the layer and the colour also changes. Defects are seen in the material, caused by irregularities at the glass plates or by unsolved particles in the material. It is clear however that the cell responds well to the voltage. After polymerization (5 sec. with a strong UV source), the director seems to maintain its orientation even when the voltage source is disconnected (Figure 6.5). However, this evaluation method is based on visual appearance. A more precise method is given next.

6.2.3 Spectroscopy

6.2.3.1 Thickness of the cell

The general outline of a spectrometer as used in this chapter, is given in Figure 6.6. The polarizers in the figure are drawn perpendicular to each other but might as well be used in a parallel configuration. An empty cell in the spectrometer acts as a Fabry-Perot etalon. The transmission peaks when the roundtrip in the cavity

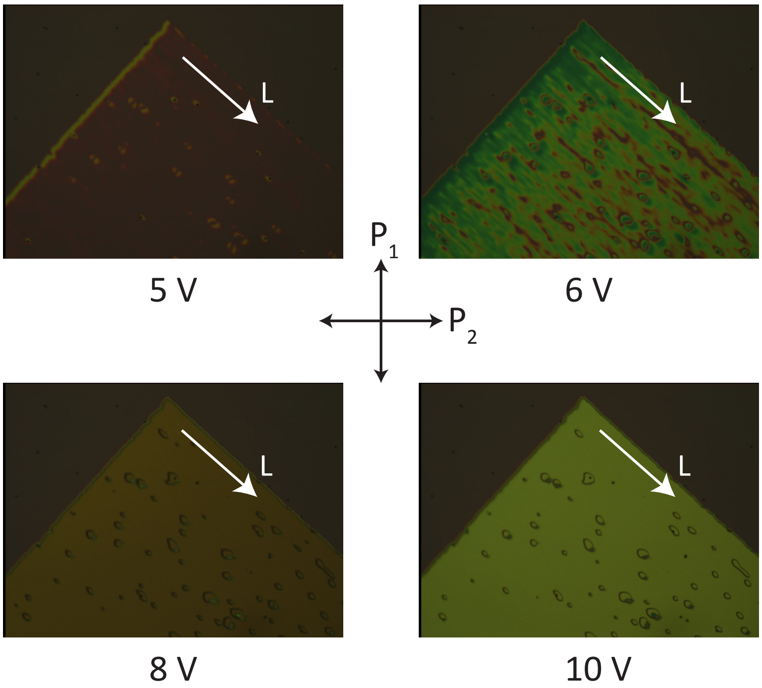

Figure 6.4: Polymerizable LC seen through a polarizing microscope with crossed polarizers. Different voltages are applied.

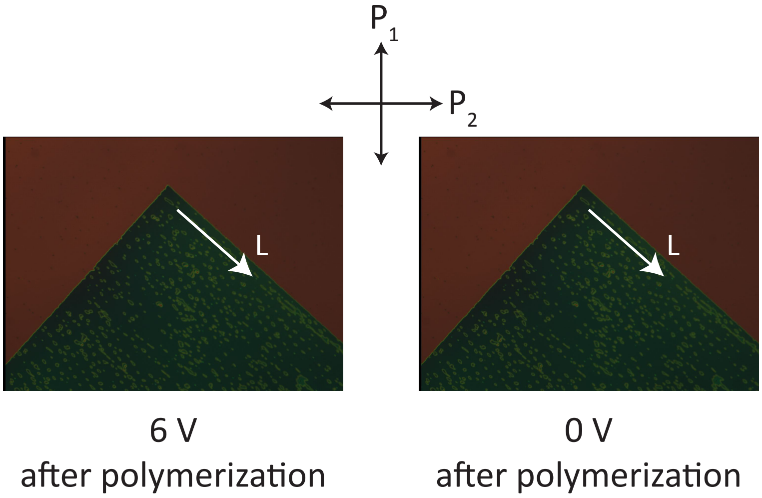

Figure 6.5: Polymerized LC seen through a polarizing microscope with crossed polarizers. Hardly any difference can be seen when the voltage source is disconnected.

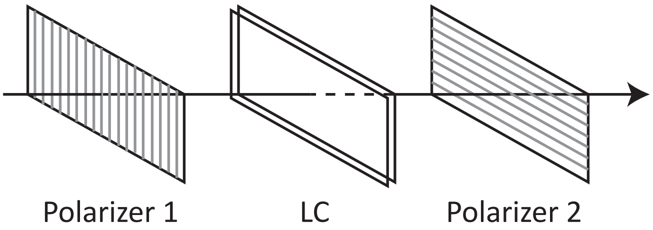

Figure 6.6: General schematic outline of a spectrometer as used in this chapter. The polarizers are drawn in a crossed configuration.

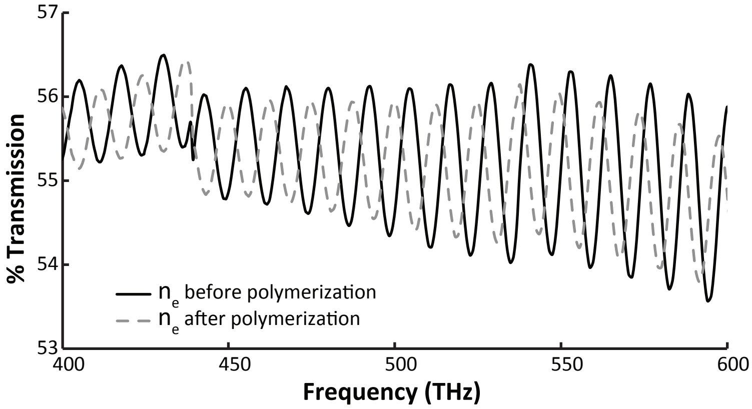

Figure 6.7: Transmission spectrum in order to determine n$_e$ before and after polymerization.

equals an integer times 2π:

$$f = q\frac{c}{2nd}, \tag{6.7}$$

with f the frequency, d the thickness of the cell, n the refractive index and q an integer. The distance between two peaks can be read out from a spectrum and the thickness of the cell is determined with equation 6.7

6.2.3.2 Refractive indices at one wavelength

Method

The refractive indices (n_e and n_o) of an anisotropic material can be determined with a setup as in Figure 6.6, but with polarizer and analyzer (polarizer 2) in a parallel configuration. The ordinary refractive index is determined with the director perpendicular to polarizer and analyser. The extraordinary refractive index requires the director to be parallel to polarizer and analyzer. The polarized light sees only one refractive index in this way. When we determine the thickness of the empty cell in advance, we can easily determine both refractive indices of the filled cell.

Results

The spectra of one cell with director parallel and perpendicular to polarizer and analyzer are shown in Figure 6.7 and Figure 6.8 before and after polymerization. We determine the distance between the peaks and calculate the effective indices. These are shown in Figure 6.9. Each value are averages of the 50 nm interval in which they lie. The error bars denote the deviation due to the resolution of the spectrometer. There is a trade-off between averaging over more peaks for a more

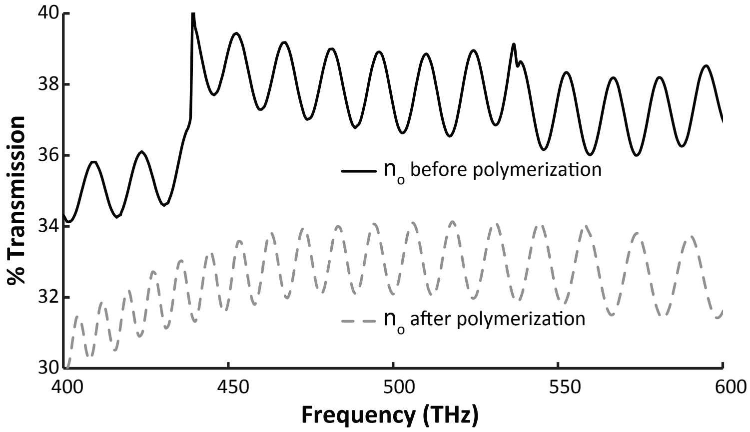

Figure 6.8: Transmission spectrum in order to determine n$_e$ before and after polymerization.

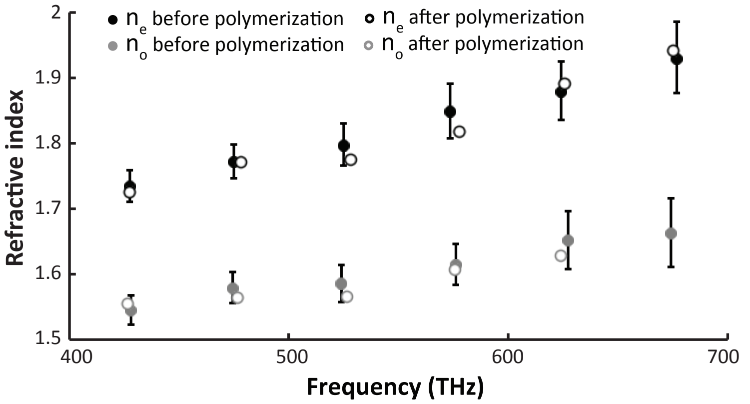

Figure 6.9: n$_o$ and n$_e$ at different wavelengths.

accurate Δf and taking into account the dispersion by averaging over a small range. It can be seen that

- n_o increases from about 1.55 to 1.65 in the wavelength interval 400 nm-700 nm
- n_e increases from about 1.75 to 1.95 in the wavelength interval 400 nm-700 nm

The polymerization causes a small fluctuation in n_o and n_e.

6.2.3.3 Birefringence

Method

With no voltage applied, the birefringence of a cell is $\Delta n = n_e - n_o$. When a voltage is applied, the director makes an angle θ with the propagation direction. From equation 1.14 it can be derived that the birefringence is now

$$\Delta n = n_{eff} - n_o = \frac{1}{\sqrt{\frac{cos^2(\theta)}{n_o^2} + \frac{sin^2(\theta)}{n_e^2}}} - n_o. \tag{6.8}$$

Note that n$_{eff}$ has not the same meaning as the effective index of the waveguide mode from the previous chapters. The reorientation is not uniform throughout the cell and a measurement of the transmitted light will yield an averaged result for n$_{eff}$. However, the birefringence as determined in this section, is a measure of the orientation of the molecules and we can quantify the effect of the polymerization.

The cell is inserted between crossed polarizers (Figure 6.6). The director is at an angle of 45^o with the polarizers. The Jones matrix formalism allows to calculate the transmission:

$$\begin{bmatrix} E_{x,o} \\ E_{y,o} \end{bmatrix} = \begin{bmatrix} 0 & 0 \\ 0 & 1 \end{bmatrix} \cdot \begin{bmatrix} cos(45^o) & -sin(45^o) \\ sin(45^o) & cos(45^o) \end{bmatrix} \cdot \begin{bmatrix} e^{-j\frac{2\pi n_{eff} d}{\lambda}} & 0 \\ 0 & e^{-j\frac{2\pi n_o d}{\lambda}} \end{bmatrix}$$

$$\cdot \begin{bmatrix} cos(45^o) & sin(45^o) \\ -sin(45^o) & cos(45^o) \end{bmatrix} \cdot \begin{bmatrix} 1 & 0 \\ 0 & 0 \end{bmatrix} \cdot \begin{bmatrix} E_{x,i} \\ E_{y,i} \end{bmatrix} \tag{6.9}$$

The x-axis is chosen along the direction of the first polarizer, the y-axis along the second, the analyzer. The intensity after the analyzer is proportional to

$$I_o \propto |E_{x,o}|^2 + |E_{y,o}|^2 = sin^2\left(\frac{\pi d(n_{eff} - n_o)}{\lambda}\right)|E_{x,i}|^2 \tag{6.10}$$

With the spectrometer, we can measure the relative intensity I_o/I_i as a function of wavelength. Δn can be determined by fitting the measured spectrum to the theoretical one. The birefringence is, due to dispersion, not constant for changing wavelengths, and we use the Cauchy equation

$$\Delta n(\lambda) = A + \frac{B}{\lambda^2} + \frac{C}{\lambda^4} \tag{6.11}$$

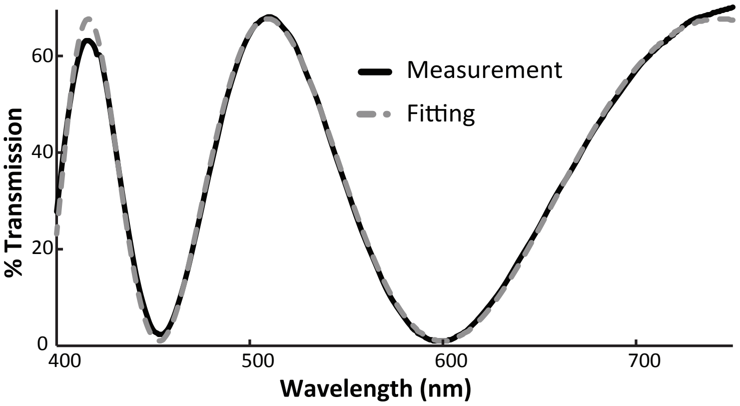

Figure 6.10: Measured and fitted intensity transmission of a LC cell as a function of wavelength. The director is at a 45^o angle with the polarizers.

as an approximation. We introduce a factor M to match the amplitude of the oscillations and an offset O. The fitting model then becomes

$$I = M\left(sin^2\left(\frac{\pi d\left(A+\frac{B}{\lambda^2}+\frac{C}{\lambda^4}\right)}{\lambda}\right)\right)+O \tag{6.12}$$

Results

In Figure 6.10 a measured spectrum and fitting is shown. They are in good agreement and we can easily derive the Δn from the A, B and C values. The resulting dispersion curve is displayed in Figure 6.11. The values for 0V lie around 0.25, in agreement with Figure 6.9. When a voltage is applied, we see that the spectrum shifts towards shorter wavelengths (Figure 6.12). Fitting the curves for each voltage, allows us to obtain the dispersion as a function of voltage (Figure 6.11). The birefringence decreases for increasing voltages. This is intuitively clear as the molecules make an increasing angle with the glass plates. n_{eff} will shift gradually from n_e to n_o. Finally, the material behaves like an isotropic material with $\Delta n = 0$. There is a threshold value of about 2 V for the Fr$\acute{e}$edericksz transition (Figure 6.13). After polymerization by UV illumination the birefringence remains the same with or without voltage applied. We have polymerized different cells at different voltages. It seems that the birefringence always drops a little during polymerization. We suspect that during polymerization bonds are formed that may break the alignment of the molecules. This in turn leads to a drop in the order parameter and anisotropy. It is difficult to predict how much the birefringence will change during polymerization, more

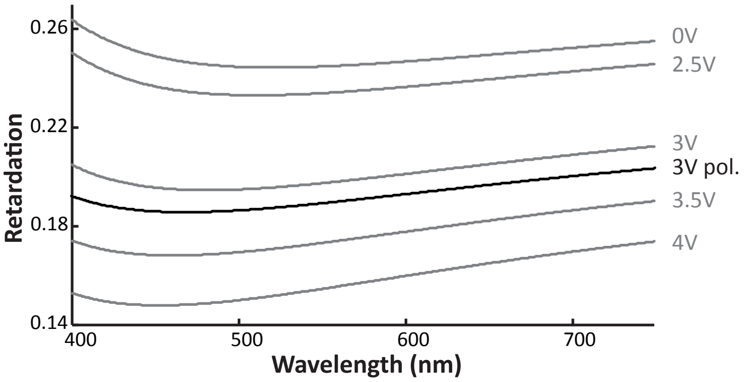

Figure 6.11: Birefringence as a function of wavelength. In black, the values after polymerization.

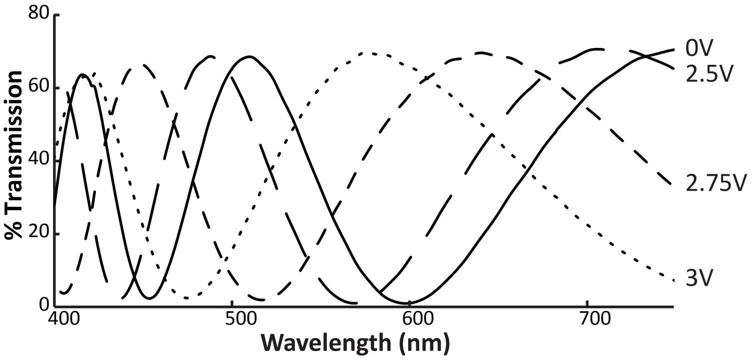

Figure 6.12: The transmission spectrum of the polymerizable LC cell shifts towards shorter wavelengths for an increasing voltage.

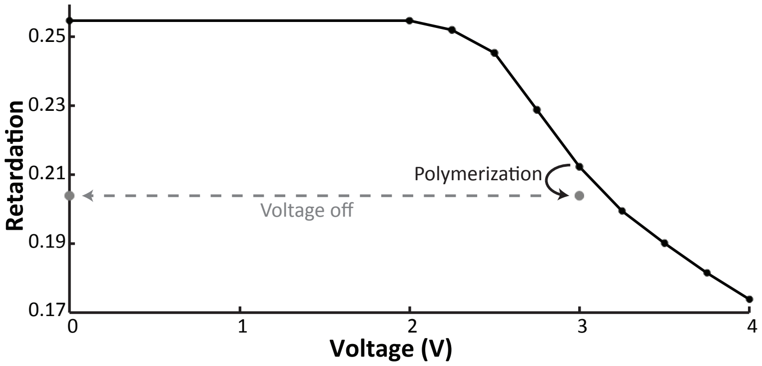

Figure 6.13: Birefringence of the polymerizable LC cell as a function of voltage. In gray, the value after polymerization.

measurements are needed.

6.3 Trimming ring resonators

In this section we discuss ring resonators with a cladding of polymerizable LC. The effects of applied voltage and polymerization are studied.

6.3.1 Cells and setup

The cells are prepared through the manual process as described in chapter 3. A glass plate is glued to a SOI chip with UV curable glue and spacers. On the glass plate are an unpatterned ITO layer for contacting and an alignment layer. Metallic wires are attached to the substrate and the ITO layer. Right before the measurments are done, the cell is filled with polymerizable LC. The cell is fixed on the vacuum chuck of the setup. Light is coupled into and out of the waveguides through grating couplers [18]. The light source is a tunable laser and the outcoupled power is detected with a power meter. The metallic wires are connected to a voltage source. AC voltage is needed to prevent ion drift in the LC [19]. To polymerize the cell, we illuminate it for 5 sec. with a strong UV source. The waveguides used for these experiments are 500 nm wide and 220 nm high. The rings have a bend radius of 6 μm.

6.3.2 Measurements

We measure the output spectrum of the ring resonators. The output power as a function of the wavelength shows the familiar dips at the wavelengths where the

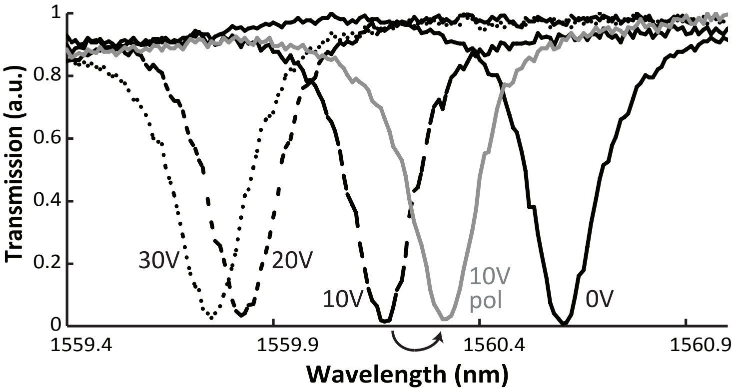

Figure 6.14: A ring resonator coated with polymerizable LC behaves like it were coated with regular LC. The resonance wavelength shifts towards shorter wavelengths for increasing voltages. Polymerization induces an extra redshift.

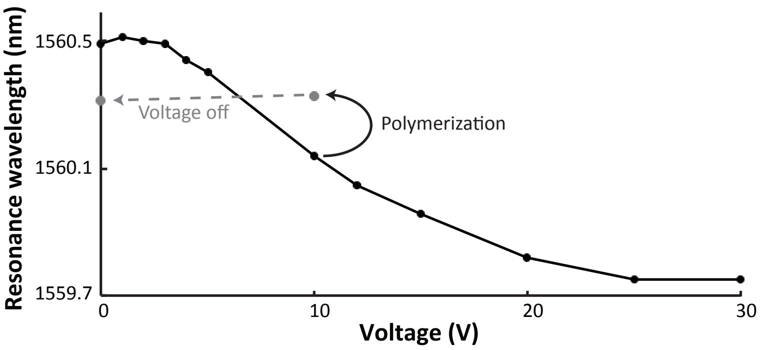

Figure 6.15: Trace of the resonance wavelength of a ring resonator coated with polymerizable LC.

light in the ring resonates. For increasing voltages the resonances shift towards shorter wavelengths (Figure 6.14). This is to be expected as the cell behaves exactly the same as the top-bottom tuning cells as discussed in chapter 4. Like with a regular nematic LC, the resonances become slightly less pronounced and less deep when a voltage is applied. A better uniformity would again require an extra alignment layer on the chip surface. However, the quality of the rings is certainly high enough for this trimming experiment. The tuning curve (Figure 6.15) shows familiar features like the threshold value (around 3 V) and saturation at higher voltage. We can conclude that the mixture is similar to a regular nematic LC in the cells we studied. The tuning range here is smaller due to larger dimensions

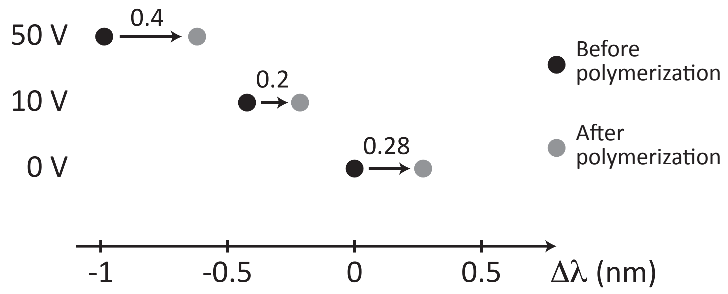

Figure 6.16: The effect of polymerization on the resonance wavelength in different cells.

of the waveguide than those used in chapter 4.

Upon polymerization, we see that the resonance wavelength of the rings undergoes another shift. This shift is larger than is to be expected from the experiments in section 6.2.3. We suspect that bonds between the molecules can introduce forces that reorient the molecules in the plane. This increases the effective index of the mode. Moreover, it is not trivial to predict the behaviour of a material that is polymerized while in contact with a nanostructured surface. If, for example, the polymerization process reduces the distance between molecules, the total volume may change a bit. This effect will of course be especially pronounced at the surfaces. The resonances shift towards the red side of the spectrum. In Figure 6.16 we have combined the measurements of three cells. One was polymerized at 0V, a second at 10V and a third at 50V. In all three cases the resonance shifts towards longer wavelengths. There seems to be no clear connection between the magnitude of the shift before and during polymerization. A prediction of exact position of the resonance after polymerization remains difficult. Furthermore, part of the tuning range is undone by the extra shift induced by the polymerization (a remaining shift of 0.56 nm is measured). When the voltage source is disconnected, the resonance peak remains fixed (a small deviation of 0.02 nm is seen). After a longer period of time (measurements were performed again after 19 days), the position remains unchanged. We can conclude that the rings are successfully trimmed.

In order for this process to become useful in real-life components, some aspects of the trimming still need to be cleared out. The initial tuning range can be increased using larger rings with smaller waveguide dimensions. This was discussed in section 4.3.2. More measurements should be performed to be able to predict the wavelength shift of the trimming process.

6.4 Conclusions

In this chapter we have introduced polymerizable LCs for the trimming of ring resonators. The material is a mixture of several polymerizable LC molecules, 5CB, an initiator and an inhibitor. The mixture behaves like a regular nematic LC when it comes to aligning to a surface and reorienting in the presence of an electric field. When illuminated with UV light, the molecules bond to each other and form a interconnected network. The material is now solidified. We have used the polymerizable mixture as a cladding layer on silicon-on-insulator ring resonators. When a voltage is applied, the resonance wavelength of the ring shifts towards shorter wavelengths, like in regular top-bottom tuning cells. Polymerization introduces an additional redshift undoing part of the tuning range. After polymerization, the resonance wavelength remains fixed. While we have demonstrated that the trimming principle works, further investigation remains necessary to fully quantify the process.

References

[1] S. Lambert. *Afstemmen van geïntegreerde optische componenten door middel van gepolymeriseerde vloeibare kristallen.* Master Thesis, 2011.

[2] S. K. Selvaraja, P. Jaenen, W. Bogaerts, D. Van Thourhout, P. Dumon, and R. Baets. *Fabrication of Photonic Wire and Crystal Circuits in Silicon-on-Insulator Using 193-nm Optical Lithography.* Journal of Lightwave Technology, 27:4076–4083, 2009.

[3] W. Bogaerts, D. Taillaert, B. Luyssaert, P. Dumon, J. Van Campenhout, P. Bienstman, D. Van Thourhout, R. Baets, V. Wiaux, and S. Beckx. *Basic structures for photonic integrated circuits in silicon-on-insulator.* Optics Express, 12:1583–1591, 2004.

[4] I. Kiyat, A. Aydinli, and N. Dagli. *Low-power thermooptical tuning of soi resonator switch.* Photonics Technology Letters, 18:364–366, 2006.

[5] E. J. Klein, D. H. Geuzebroek, H. Kelderman, G. Sengo, N. Baker, and A. Driessen. *Reconfigurable optical add-drop multiplexer using microring resonators.* Photonics Technology Letters, 17:2358–2360, 2005.

[6] P. Dong, W. Qian, H. Liang, R. Shafiiha, D. Feng, G. Li, J. Cunningham, A. Krishnamoorthy, and M. Asghari. *Thermally tunable silicon racetrack resonators with ultralow tuning power.* Optics Express, 18:20298–20304, 2010.

[7] A. Liu, L. Liao, D. Rubin, H. Nguyen, B. Ciftcioglu, Y. Chetrit, N. Izhaky, and M. Paniccia. *High-speed optical modulation based on carrier depletion in a silicon waveguide.* Optics Express, 15:660–668, 2007.

[8] J. Schrauwen. *Focused Ion Beam Processing of Nanophotonic Structures.* PhD. Thesis, 2009.

[9] G. Odian. *Principles of polymerization.* John Wiley & sons, 2007.

[10] F. C. De Schryver. *Photopolymerization.* Pure and Applied Chemistry, 34:213–224, 1973.

[11] A. Ledwith. *Photoinitiation of polymerization.* Pure and Applied Chemistry, 49:431–441, 1977.

[12] D. J. Broer. *In-situ photopolymerization of oriented liquid-crystalline acrylates.* PhD. Thesis, 1990.

[13] C. Van Oosten. *Resposive Liquid Crystal Networks.* PhD. Thesis, 2009.

[14] D. Coates, M. J. Goulding, S. Greenfield, J. M. W. Hanmer, E. Jollife, S. A. Marden, O. L. Parri, and M. Verrall. *New applications of liquid crystals and liquid crystal polymers.* Proceedings of Euro Display '96 (Society for Information Display), pages 91–94, 1996.

[15] D. J. Broer, J. Lub, and G. N. Mol. *Wide-band reflective polarizers from cholesteric polymer networks with a pitch gradient.* Nature, 378:467–469, 1995.

[16] M. Yamada, M. Kondo, R. Miyasato, Y. Naka, J. Mamiya, M. Kinoshita, A. Shishido, Y. L. Yu, C. J. Barrett, and T. Ikeda. *Photomobile polymer materials-various three-dimensional movements.* Journal of Materials Chemistry, 19:60–62, 2009.

[17] J. H. Lee, D. N. Liu, and S. T. Wu. *Introduction to flat panel displays.* John Wiley & sons, 2008.

[18] D. Taillaert, P. Bienstman, and R. Baets. *Compact efficient broadband grating coupler for silicon-on-insulator waveguides.* Optics Letters, 29:2749–2751, 2004.

[19] A. Di Falco and G. Assanto. *Tunable wavelength-selective add-drop in liquid crystals on a silicon microresonator.* Optics Communications, 279:210–213, 2007.

7

Conclusions and Outlook

7.1 2006 to 2011

The focus of this work has been the study of SOI ring resonators with an LC cladding for tuning purposes. The optical properties of LCs can be changed with an externally applied electric field. This gives us the possibility to alter the effective index of a waveguide or the resonance of a ring resonator electrically, provided that the waveguides are clad with LC. We have shown that this can be done. We have made a distinction between ring resonators guiding TE light and ring resonators guiding TM light. The first were tuned 4.6 nm towards shorter wavelengths in a top-bottom electrode configuration (one electrode below the ring resonator and one above the cladding) and were tuned 1 nm towards longer wavelengths in an in-plane switching cell (electrodes left and right of the ring). The TM ring resonators were tuned 31 nm towards longer wavelengths in a top-bottom configuration. The major achievements of this work can be summed up as follows:

- Understanding the behaviour of LCs on a structured SOI surface. Studying the LC cladding with a polarizing microscope has taught us that the LC director aligns with the waveguide structures on the surface of the chip. When the top of the cladding has a fixed orientation due to the presence of an alignment layer, the director twists throughout the cladding to align to the waveguides.

- Simulating the director in a waveguide geometry in the presence of an electric field. This gives insight in how the LC behaves on surfaces with nano-scale structures. We have studied the influence of several parameters such as anchoring strength of the surface, thickness of the cell and dimensions of the waveguides. A low anchoring strength, thin cells and narrow waveguides lead to better performance of the tunable devices.
- Simulating the modes in SOI waveguides with a liquid crystal cladding. We have used a fully anisotropic mode solver that uses the data from the director calculation as input.
- Fabricating and measuring test cells consisting of SOI chips covered with LC and sealed with a glass plate. On the glass plate, there are an alignment layer and an ITO electrode layer present. This has resulted in tuning ranges of 31 nm and 4.6 nm for TM and TE ring resonators respectively.
- Trimming ring resonators using polymerizable LC. We have shown that ring resonators can be trimmed but we have yet to prove the repeatability of this process.

At this point we have a well-understood method to tune ring resonators with a cladding layer of liquid crystals. In the next section we suggest different routes that can be taken from here.

7.2 2012 and onwards

7.2.1 Wavelength tuning of different components

In this work, we have devoted our attention to the tuning of ring resonators. Now that the mechanisms and fabrication are well understood, the technique can be applied to different photonic components.

- Next to ring resonators, a whole range of other **filters** exist. Resonant filters, like Fabry-Perot resonators, can in principle be tuned like ring resonators. Filters not based on resonance, like Mach-Zehnder interferometers, will have a tuning range dependent on the length difference between the tuned and the reference arm. A component that we find very interesting in this respect, is an AWG (Arrayed Waveguide Grating). This component divides a broad spectrum into narrow peaks and sends them to different waveguides. This component can be made completely tunable with the method described in this thesis.

- A widely tunable **laser** on silicon is a holy grail that has not seen an efficient implementation yet. Solutions like bonded lasers on silicon can potentially become tunable if a liquid crystal top layer is applied. However, this is not as straightforward as it sounds. To achieve a tunable laser with a tuning range of 31 nm, like the best result in this work, we need a resonator that has an FSR of at least 31 nm. This translates into TM guiding rings that have a bend radius of only 4 to 5 μm. Bend losses for the TM mode will be considerable, certainly too high for an efficient laser. A solution may be to use resonators without bends, like Fabry-Perot resonators or waveguides with DBR mirrors. The fabrication of these devices is far from easy due to the precision required in the mirror section. We believe, however, that this route of straight resonators is the most logical route towards a widely tunable laser in the near future.

7.2.2 Maximizing the tuning range

The tuning ranges reported in this work, are the widest to be found in literature. However, we believe that there is still quite some room for improvement in this area. The waveguides that we have used are of standard height and width. The height is 220 nm and the width varies from 450 nm to 500 nm. When we would make these dimensions even smaller, a larger portion of the waveguide modes will be located in the cladding of the waveguide. This increases the interaction of the light with the LC and the tuning range of the rings. Ideally, TE waveguides should be made narrower to enhance interaction at the sidewalls. Care has to be taken, however, that the losses due to sidewall roughness do not become too dramatic. Waveguides guiding the TM mode should be made lower to increase interaction at the top of the waveguide. Here, roughness is typically not a problem at all. In both cases, losses due to the liquid crystal will increase in comparison with the results of this work. Careful surface treatment may reduce these losses, but may also reduce the interaction and tuning range.

7.2.3 Quantifying the power consumption

In this work, the focus has been on understanding the tuning mechanisms and demonstrating that ring resonators can be tuned with liquid crystals. While we succeeded in this part, not much work has been done yet to quantify the power consumption for this type of devices. We suspect the power consumption to be relatively low as tuning our devices essentially boils down to charging a capacitor, assuming the leakage current is very low. Further research has to be done in order to confirm this.

7.2.4 Large-scale fabrication and testing

A third route we propose is to investigate the possibilities for a larger scale of fabrication. In this work, all devices were constructed manually. This is an intrinsically slow process with a high risk of fabrication errors. What is more, the fabrication itself can influence the behaviour of the devices. We have shown in chapter 5 that, among others, the device thickness influences the tuning. This parameter is hard to control precisely when assembling a device manually. Further testing of tunable integrated optical components would benefit from a well-controlled machine assembly of the devices. It may be useful to look to machinery and techniques used in display technology.

7.3 Final conclusion

It is now clear that widely tunable integrated components in silicon-on-insulator can be made by adding liquid crystals as a top cladding layer. The thesis:

Integrated optical filters in general and ring resonators in particular can be tuned over a wide wavelength range when they are clad with a layer of liquid crystals to which an external electric field is applied,

has been proven. The experiments and simulations performed in this work have shown this. To get these tunable components into real-life applications, a considerable testing period and research into the practical development of the devices are still required. We believe that the components discussed here are indeed very promising. However, their future in real applications depends on the follow-up to this work and further research efforts.

List of Figures

1 Heroriëntering van een vloeibaar kristal toplaag op een SOI golfgeleider. xix
2 De resonantie van een TE ring kan afgestemd worden over 4.6 nm naar kortere golflengtes. xx
3 De resonantie van een TM ring kan afgestemd worden over 31 nm naar langere golflengtes. xxi

1 Reorientation of the LC cladding. xxiv
2 Resonance wavelength of a ring resonator guiding TE light as a function of voltage. xxvi
3 Resonance wavelength of a ring resonator guiding TM light as a function of voltage. xxvi

1.1 The nematic LC phase. 4
1.2 The smectic A and C LC phases. 5
1.3 Disk and banana-shaped LCs. 6
1.4 (a) Schematic view of a typical nematic LC. (b) Schematic view of a 5CB molecule. 6
1.5 Tilt (θ) and twist (ϕ) in the xyz coordinate system. 8
1.6 The three basic elastic deformations of the director are splay, twist and bend. 11
1.7 Schematic top and side view of a polymer rubbing layer. 12
1.8 LC molecules realign in an external electric field. 13
1.9 Cross section of the SOI stack. 14
1.10 In a high index contrast waveguide, bends can be sharper as more propagation angles are allowed. 15
1.11 Schematic top view of a notch or all-pass ring resonator. 17
1.12 Schematic top view of a add-drop ring resonator. 18
1.13 Typical pass transmission of a ring resonator. 18

2.1 Schematic view of a slab waveguide clad with a layer of LC. 26

2.2 X, y and z components of the electric field of the TE mode (left) and the TM mode (right). 28
2.3 Effective index and resonance wavelength of LC-clad TE ring resonators, for different director orientations. 29
2.4 Effective index and resonance wavelength of LC-clad TM ring resonators, for different director orientations. 30

3.1 Schematic top and side view of an LC-clad device. 38
3.2 Photograph of a completed cell. 40
3.3 General outline of a polarizing microscope in reflection. 41
3.4 Principle of observing a cell with a polarizing microscope. 42
3.5 Transmission of a twisted cell. 43
3.6 Transmission of a uniform cell. 44
3.7 Polarizing microscope image of a waveguide and grating covered with LC. The inset shows the structure outline. 45

4.1 Photograph of the measurement setup. 48
4.2 Top view of a TE and TM grating coupler. 49
4.3 Schematic cross section of a symmetric and asymmetric waveguide. 50
4.4 Effective refractive index (n_{eff}) as a function of waveguide width in symmetric and asymmetric waveguides. 51
4.5 Polarization microscope image of a ring resonator with a cladding of LC. 54
4.6 Polarization microscope images of the LC-clad ring resonator for increasing voltages. 55
4.7 Polarization microscope images of the LC-clad ring resonator for increasing voltages. The rubbing is at an angle with the polarizer. 56
4.8 Transmission of a ring notch filter with LC cladding for increasing voltages. 57
4.9 Resonance wavelength of the ring resonator as a function of voltage. 58
4.10 Q-factor of the TE ring resonator as a function of voltage. 58
4.11 (a) Schematic view of a ring resonator as used in the IPS experiments. (b) Schematic view of the finger electrodes. 60
4.12 Polarization microscope image of ring resonators in an IPS electrode configuration. 61
4.13 Transmission of a notch filter with LC cladding for different voltages in an in-plane switching cell. 62
4.14 Trace of the resonance wavelength as a function of applied voltage. 63
4.15 Q-factor of the ring resonator as a function of applied voltage. . . 64
4.16 Resonance wavelength of a ring with and without LC cladding as a function of temperature. 66

4.17 Temperature-dependent refractive indices of UCF-2 (a nematic liquid crystal mixture) and 5CB at λ=589 nm. Figure reproduced from [10] . . . 67
4.18 Transmission of a ring notch filter with LC cladding for increasing voltages. The rings guide the TM mode. . . . 69
4.19 Resonance wavelength of a ring resonator guiding TM light, as a function of voltage. . . . 70
4.20 Evolution of the Q-factor of TM ring resonators with LC cladding for increasing voltage levels. . . . 70
4.21 (Dynamic measurements) Transmission of the LC-clad ring resonator as a function of wavelength with and without voltage applied. 72
4.22 (Dynamic measurements) Transmission of the ring as a function of time. . . . 73

5.1 Mesh generated with the GiD program. The assigned materials are indicated. . . . 77
5.2 Simulated director orientation in a waveguide cladding layer for 0V and 20V. The electrodes are in a top-bottom configuration. . . . 77
5.3 Simulated director orientation in a waveguide cladding layer for 7V. The electrodes are in an in-plane switching configuration. . . . 78
5.4 Simulated tuning curves for the TE mode for hard and weak anchoring. . . . 82
5.5 Close-up of the threshold voltages of the different tuning curves. . 83
5.6 Simulated tuning curves for the TM mode for hard and weak anchoring. . . . 83
5.7 Simulated top-bottom tuning curves for the TE mode for hard and weak anchoring in an IPS configuration. . . . 84
5.8 Tuning curves simulated for top-bottom tuned TE waveguides with LC cladding layers of different thicknesses. . . . 86
5.9 Tuning curves simulated for top-bottom tuned TM waveguides with LC cladding layers of different thicknesses. . . . 86
5.10 Tuning curves simulated for TE waveguides in an IPS cell with different electrode spacings. . . . 87
5.11 Top-bottom tuning curves simulated for TE resonators with different waveguide widths. . . . 88
5.12 Top-bottom tuning curves simulated for TM resonators with different waveguide widths. . . . 89
5.13 A comparison between the experimental and simulated tuning curve for ring resonators guiding TM light. . . . 90

5.14 A comparison between the experimental and simulated tuning curve for ring resonators guiding TE light. The electrodes are in a top-bottom configuration. 91
5.15 A comparison between the experimental and simulated tuning curve for ring resonators guiding TE light. The electrodes are in an in-plane switching configuration. 92

6.1 LC polymers organized in a network (a), a side-chain polymer (b), and a main-chain polymer (c) 98
6.2 (a) Acrylate monomer, (b) acrylate polymer 98
6.3 Phase diagram of a binary mixture. 101
6.4 Polymerizable LC seen through a polarizing microscope with crossed polarizers. Different voltages are applied. 102
6.5 Polymerized LC seen through a polarizing microscope with crossed polarizers. Hardly any difference can be seen when the voltage source is disconnected. 103
6.6 General schematic outline of a spectrometer as used in this chapter. The polarizers are drawn in a crossed configuration. 103
6.7 Transmission spectrum in order to determine n$_e$ before and after polymerization. 104
6.8 Transmission spectrum in order to determine n$_e$ before and after polymerization. 105
6.9 n$_o$ and n$_e$ at different wavelengths. 105
6.10 Measured and fitted intensity transmission of a LC cell as a function of wavelength. The director is at a 45^o angle with the polarizers. . 107
6.11 Birefringence as a function of wavelength. In black, the values after polymerization. 108
6.12 The transmission spectrum of the polymerizable LC cell shifts towards shorter wavelengths for an increasing voltage. 108
6.13 Birefringence of the polymerizable LC cell as a function of voltage. In gray, the value after polymerization. 109
6.14 Transmission spectra of a ring resonator clad with polymerizable LC.110
6.15 Trace of the resonance wavelength of a ring resonator coated with polymerizable LC. 110
6.16 The effect of polymerization on the resonance wavelength in different cells. 111